N-Glycosylation signatures of epithelial ovarian cancer

Inaugural-Dissertation

to obtain the academic degree

Doctor rerum naturalium (Dr. rer. nat.)

submitted to the Department of Biology, Chemistry, Pharmacy

of Freie Universität Berlin

by

Marta Grzeski

from Jaworzno

(Poland)

2021

This work was conducted between Apr-2015 and Jul-2021 under the supervision of Prof. Dr. Véronique Blanchard at the Institute of Laboratory Medicine, Clinical Chemistry and Pathobiochemistry, Charité - Universitätsmedizin Berlin.

I declare that the doctoral thesis entitled "*N*-glycosylation signatures of epithelial ovarian cancer" and the work presented in it are my own. I certify that I have prepared and written this thesis independently using only the aids and tools specified. I confirm that the thesis contains no material that has been submitted previously, in whole or in part, for the award of any other academic degree or diploma.

First Reviewer: Prof. Dr. Véronique Blanchard
Second Reviewer: Prof. Dr. Kevin Pagel
Date of defence: 18.11.2021

To all women fighting ovarian cancer

Zusammenfassung

Trotz intensiver Forschung auf dem Gebiet der Diagnostik und Therapie ist das epitheliale Ovarialkarzinom (EOC) nach wie vor die tödlichste gynäkologische Krebsentität bei Frauen. Das Fehlen von sensitiven und spezifischen Biomarkern für die Diagnose von EOC in einem frühen, noch heilbaren Stadium, hat die Aufmerksamkeit auf die Untersuchung der veränderten Proteinglykosylierung gelenkt, welche als ergänzende Screening Marker eingesetzt werden könnten. Während das Serum-*N*-Glykom bei EOC-Patientinnen umfassend untersucht wurde, gibt es nur wenige Daten zu Glykosylierungsveränderungen, der einzelnen in Serum oder im Gewebe vorkommenden Glykoproteine. Um diese Wissenslücke zu schließen, wurden in dieser Arbeit EOC-spezifische Glykosylierungsveränderungen des häufigsten Serumglykoproteins Immunglobulin G (IgG) ausführlich analysiert. Ergänzend dazu, wurde das gesamte Gewebe-*N*-Glykom diverser morphologischer Subtypen des EOCs mittels hochmoderner Technologie, der MALDI-Massenspektrometrie-Bildgebung (MALDI-MSI) untersucht.

Das humane IgG wird in vier Subklassen unterteilt: IgG_1, IgG_2, IgG_3 und IgG_4. Diese Subklassen unterscheiden sich hinsichtlich deren biologischen Eigenschaften und Effektorfunktionen, wobei deren Aminosäuresequenzen hohe Homologien aufweisen. Glykosylierungsveränderungen von IgG wurden bereits bei EOC Patientinnen auf der Ebene enzymatisch freigesetzter *N*-Glykane intensiv untersucht. Die derzeit verfügbaren Daten dieser Untersuchungen können jedoch nur grundlegende Informationen geben und sind weder subklassen- noch ortsspezifisch (Fc/Fab). Um einen tieferen Einblick in die Veränderungen des Glykoms im Krankheitsverlauf des EOCs zu bekommen, wurde daher der Fokus dieser Arbeit auf die Untersuchung subklassenspezifischer Veränderungen der Glykosylierung gelegt. Hierfür wurde eine umfassende Analyse auf Glykopeptidebene durchgeführt. Das IgG wurde aus dem Blutserum von 87 EOC Patientinnen (FIGO-Stadium I-IV) und 74 alterskorrelierenden gesunden Kontrollen isoliert. Zur Separation von IgG_2 und IgG_3, die über eine in den meisten Fällen identische Peptidsequenz mit der Asn297-Glykosylierungsstelle verfügen, wurde eine zweistufige Aufreinigung mittels Affinitätschromatographie unter Verwendung von Protein A (IgG_1, IgG_2, IgG_4) und Protein G Sepharose (IgG_3) durchgeführt. Isolierte IgG-Fraktionen wurden mit Trypsin verdaut und die resultierenden Glykopeptide mit HILIC-Säulen angereichert. Die Vermessung der Glykopeptide wurde mittels MALDI-TOF-MS im negativen Ionisierungsmodus durchgeführt. Durch Summation der relativen Intensitäten der jeweiligen Glykopeptidstrukturen wurden folgende sechs (bzw. fünf im Falle von IgG_2) Glykosylierungsmuster ermittelt: A-, Mono-, Digalaktosylierung, Sialylierung, bisecting GlcNAc Strukturen und Fukosylierung für die Unterklassen IgG_{1-3} berechnet. Die Analyse von IgG_4 wurde aufgrund einer geringen Serumkonzentration und überlappender Glykopeptidsignale nicht durchgeführt. In allen untersuchten IgG Subklassen wurde eine Abnahme der Mono- und Digalaktosylierung unabhängig

vom Stadium der Krankheit festgestellt. Bemerkenswert ist zudem, dass sich die Glykosylierungsprofile aller untersuchten Subklassen mit zunehmendem Alter verändern, wobei die EOC bedingten Veränderungen bei jüngeren Patientinnen stärker ausgeprägt sind. Zusätzlich deuten die subklassenspezifischen Glykosylierungsmuster darauf hin, dass jede IgG-Subklasse leicht unterschiedlich auf die Entwicklung der Krankheit anspricht. Vor allem IgG_1 zeigte die auffälligsten EOC spezifischen Glykosylierungsveränderungen, wobei die Agalaktosylierung die stärkste Assoziation zu dem diagnostischen Marker CA 125 aufwies. Des Weiteren ergab die Kombination der IgG_1-Glykosylierung und dem CA 125 Marker im Vergleich zu IgG_2 und IgG_3 die beste diagnostische Prognose bei der Differenzierung gesunder Kontrollen von den EOC-Patientinnen unabhängig vom Alter und Stadium der Krankheit. Darüber hinaus konnte in dieser Arbeit gezeigt werden, dass eine simultane Analyse von IgG_2 und IgG_3 aufgrund ihrer deutlich unterschiedlichen Glykosylierungsphänotypen vermieden werden sollte.

Ziel des zweiten Teils dieser Arbeit war es, Glykosylierungsveränderungen von Glykoproteinen zu bestimmen, die in Eierstockkrebszellen und deren direkten Umgebung exprimiert werden. Die Analyse wurde mittels MALDI-MSI durchgeführt, die eine Visualisierung der räumlichen Verteilung zahlreicher Analyten in einem einzigen Bildgebungsexperiment ermöglicht. Das untersuchte Material bestand aus Formalin-fixierten und in Paraffin eingebetteten Gewebeproben. Neben den Gewebeproben von dem häufigsten und aggressivsten EOC Subtypen, dem *high-grade* serösen Ovarialkarzinom, wurden auch weniger aggressive *low-grade* seröse, klarzellige sowie endometrioide Ovarialkarzinoma und überwiegend gutartigen *borderline*-Ovarialtumore untersucht. Alle Gewebeproben wurden de-paraffiniert, rehydriert und einer thermischen Epitopdemaskierung unterzogen. Negativ geladene Sialinsäuren wurden chemisch und damit einhergehend bindungsspezifisch derivatisiert, woraufhin alle im Gewebe enthaltenen *N*-Glykane mit dem Enzym PNGase F *in situ* freigesetzt wurden. Die freigesetzten *N*-Glykane wurden anschließend mit einem rapifleX MALDI Tissuetyper gemessen. Das verwendete Protokoll erlaubte die Detektion von über 60 *m/z* Spezies, wobei sowohl die neutralen als auch die negativ geladenen sialylierten *N*-Glykane dem Oligomannose-, Hybrid- und Komplex-Typ entsprachen. Auffällig war, dass die detektierten *N*-Glykantypen in den von Pathologen definierten Geweberegionen, distinkt verteilt waren. *N*-Glykane mit hohem Oligoannose Gehalt wurden vor allem in Tumorregionen nachgewiesen, während die neutralen komplexen *N*-Glykane häufiger in Gewebebereichen ohne Tumorzellen nachgewiesen werden konnten. Aufgrund der chemischen Derivatisierungsreaktion und damit einhergehender Massenverschiebung konnten die α2,3- und die α2,6-sialylierten *N*-Glykanstrukturen bindungsspezifisch detektiert werden. Somit handelt es sich um die erste Studie, in der eine *in situ* Sialylierung der *N*-Glykane in seiner stabilen und bindungsspezifischen Form im EOC Gewebeproben dargestellt werden konnte. Beachtenswert ist dabei, dass die unterschiedlich sialylierten *N*-Glykanstrukturen sich im Gewebe spezifisch verteilten. Während die α2,6-sialylierten *N*-Glykane im Tumor und in tumornahen nekrotischen Regionen

vorkamen, wurden die α2,3-sialylierten *N*-Glykane vorwiegend in den von tumorfreien Regionen detektiert. Mit Hilfe von statistischer Analyse konnte eine Reihe von gewebetypspezifischen *N*-Glykanen ermittelt werden, die eine Diskriminierung von kanzerogenem und nicht-kanzerogenem Ovarialgewebe erleichtert und ferner potenziell als Biomarker zur Diagnose des epithelialen Ovarialkarzinoms eingesetzt werden könnte.

Abstract

Despite intense research efforts, epithelial ovarian cancer (EOC) invariably remains the most lethal gynecological malignancy in women. In the absence of biomarkers capable of detecting EOC at an early, still curable stage, altered glycosylation of proteins attracted attention as a potential source of complementary screening markers. While changes of total serum *N*-glycome in EOC patients have been broadly examined, there is so far only limited data available on glycosylation alterations occurring in individual serum-derived glycoproteins and ovarian cancer tissue. Therefore, to fill this gap of knowledge, EOC-related glycosylation changes were investigated in this thesis at the level of immunoglobulin G (IgG), the most abundant serum glycoprotein, and at the level of EOC tissue, implementing cutting-edge technology, MALDI mass spectrometry imaging (MALDI-MSI).

In humans, IgG occurs as four subclasses, IgG_1, IgG_2, IgG_3, and IgG_4, which differ sharply in respect to their biological characteristics and effector functions despite high homology at the amino acid level. Although IgG glycosylation in EOC patients has already been investigated previously, EOC-related glycosylation alterations were determined at the level of enzymatically released *N*-glycans. In consequence, currently available data give only global information and is neither subclass- nor site (Fc/Fab)-specific. Therefore, in order to provide a deeper insight into glycomic changes accompanying the development and progression of EOC, in this work, glycosylation alterations were investigated in a subclass-specific manner, performing the analysis at the glycopeptide level. To this end, IgG was isolated from blood sera of 87 EOC patients (FIGO stage I-IV) and 74 age- and sex-matched healthy controls. In order to separate IgG_2 and IgG_3, whose peptide backbones encompassing the Asn297-glycosylation are frequently identical, a two-step affinity purification employing Protein A and Protein G Sepharose was performed. Isolated IgG fractions containing IgG_1, IgG_2, IgG_4, and IgG_3, respectively, were digested with trypsin, and the resulting glycopeptides were enriched using cotton-HILIC columns. Finally, measurements were performed by MALDI-TOF-MS in negative ionization mode. By summing up relative intensities of respective glycopeptide structures, six (or five in the case of IgG_2) glycosylation traits, namely a-, mono-, digalactosylation, sialylation, bisection, and fucosylation, were calculated separately for IgG_{1-3} subclasses (analysis of IgG_4 was omitted due to its very low serum concentration and overlapping glycopeptide signals). In all investigated IgG subclasses, mono- and digalactosylation were found to decrease in patients suffering from early- and late-stage EOC. Notably, as glycosylation profiles of all investigated subclasses were observed to alter with increasing age, the EOC-related alterations were more pronounced in younger patients. Additionally, the detected subclass-specific glycosylation features indicate that each IgG subclass responds slightly differently to the outbreak of the disease. Above all, IgG_1 showed the most pronounced EOC-related glycosylation alterations, and its agalactosylation showed the strongest association with CA 125 routine diagnostic marker. Additionally, as compared

to IgG_2 and IgG_3, the combination of IgG_1 glycosylation with the CA 125 marker showed the best performance in distinguishing healthy controls from EOC patients, irrespective of patients' age and EOC stage. Furthermore, the results of this work imply that a common analytical practice of simultaneous analysis of IgG_2 and IgG_3 subclasses should be avoided due to their noticeably different glycosylation phenotypes.

The aim of the second part of this work was to determine glycosylation alterations occurring directly on glycoproteins expressed in ovarian cancer cells and their surroundings. Analyses were performed using MALDI-MSI technique that enables the visualization of the spatial distribution of numerous analytes in a single imaging experiment. The investigated material consisted of formalin-fixed paraffin-embedded tissue specimens of the most common and aggressive EOC type, high-grade serous ovarian cancer, less aggressive low-grade serous, clear cell, and endometrioid ovarian cancer as well as non-malignant borderline ovarian tumor. All tissue specimens were deparaffinized, rehydrated, and subjected to heat-induced antigen retrieval. Negatively charged sialic acids were chemically derivatized in a linkage-specific manner, after which all tissue-contained *N*-glycans were released *in situ* with PNGase F. Ultimately, released *N*-glycans were measured using a rapifleX MALDI Tissuetyper. The applied protocol allowed the detection of over 60 *m/z* species corresponding to high-mannose-, hybrid-, and complex-type neutral and sialylated *N*-glycans. Importantly, observed *N*-glycans were diversely distributed within distinct tissue regions, defined by a pathologist prior to the analysis. High-mannose *N*-glycans were predominantly detected in tumor regions, while neutral complex-type *N*-glycans were more abundant in non-tumor tissue areas. Due to the mass shift introduced via a chemical derivatization reaction, the sialylated structures carrying α2,3- and α2,6-linked sialic acids could be distinguished. Notably, this is the first study, in which *in situ* sialylation of EOC tissue was investigated in its stabilized form and a linkage-specific manner. Importantly, the distribution of differently sialylated *N*-glycan structures within the tissue was observed to vary. While α2,6-sialylated *N*-glycans were enriched in tumor and tumor-related necrotic regions, α2,3-sialylated *N*-glycans were predominantly present in non-tumor tissue. Ultimately, statistical analyses revealed tissue type-specific *N*-glycan structures, which support EOC diagnosis and pave the way to serve as biomarkers to discriminate between cancerous and non-cancerous ovarian tissue.

Publication list

Publications included in this thesis:

Wieczorek M, Braicu EI, Oliveira-Ferrer L, Sehouli J, Blanchard V (2020)
Immunoglobulin G subclass-specific glycosylation changes in primary epithelial ovarian cancer.
Front. Immunol. 11:654.
https://doi.org/10.3389/fimmu.2020.00654

Wieczorek M, Taube E, Braicu EI, Sehouli J, Blanchard V*, Klein O*
* *equal contribution*
In situ N-glycosylation signatures of epithelial ovarian cancer tissue.
Manuscript in preparation

Publications not included in this thesis:

Weiz S, Wieczorek M, Schwedler C, Kaup M, Braicu EI, Sehouli J, Tauber R, Blanchard V (2016)
Acute-phase glycoprotein N-glycome of ovarian cancer patients analyzed by CE-LIF.
Electrophoresis. 37(11):1461-1467.
https://doi.org/10.1002/elps.201500518

Abbreviations

3'-SialLacNAc	3'-sialyl-*N*-acetyllactosamine
6'-SialLacNAc	6'-sialyl-*N*-acetyllactosamine
A	α2,3-linked sialic acid - amidated
aa	amino acid
ABC	ammonium bicarbonate
ACA	anti-carbohydrate antibody
ACN	acetonitrile
ADCC	antibody-dependent cell-mediated cytotoxicity
AFP	α-fetoprotein
AFP-L3	α1,6-fucosylated AFP fraction
Agal	agalactosylation
Asn	asparagine
AUC	area under the curve
Bisec	bisection
BOT	borderline ovarian tumor
C1q	complement component 1q
CA 125	cancer antigen 125
CA 19-9	carbohydrate antigen 19-9
CBB	Coomassie Brilliant Blue
CCA	cholangiocarcinoma
CDC	complement-dependent cytotoxicity
CDP	cytidine diphosphate
CDR	complementarity determining region
CE	capillary electrophoresis
CFG	Consortium for Functional Glycomics
C_H	constant domain of heavy (IgG) chain
CHCA	α-cyano-4-hydroxycinnamic acid
C_L	constant domain of light (IgG) chain
ClCCA	4-chloro-α-cyanocinnamic acid
CMP	cytidine monophosphate
ConA	concanavalin A
CRC	colorectal cancer
CTP	cytidine triphosphate
CV	coefficient of variation
D	α2,6-linked sialic acid - dimethylamidated
DC-SIGN	dendritic cell-specific intercellular adhesion molecule-3-grabbing non-integrin
DH	dextran hydrolysate
DHB	2,5-dihydroxybenzoic acid
Digal	digalactosylation
DMA	dimethylamine
DMSO	dimethyl sulfoxide
Dol-P	dolichol phosphate
Dol-P-P	dolichol diphosphate
DP	diphosphate
EC	endometrioid carcinoma
EDC	1-ethyl-3-(3-(dimethylamino)propyl)-carbodiimide
EOC	epithelial ovarian cancer
ER	endoplasmic reticulum
ESI	electrospray ionization
EtOH	ethanol

F, Fuc	fucose, fucosylation
FA	formic acid
Fab	fragment antigen binding
Fc	fragment crystallizable
FcγR	Fc gamma receptor
FcRn	neonatal Fc receptor
FDA	Food and Drug Administration
FFPE	formalin-fixed paraffin-embedded
FIGO	International Federation of Gynecology and Obstetrics
FUT	fucosyltransferase
G, Gal	galactose
GalNAc	*N*-acetylgalactosamine
Gal-ratio	a ratio of agalactosylated to mono- and digalactosylated IgG structures
GBP	glycan-binding proteins
GDP	guanidine diphosphate
Glc	glucose
GlcNAc	*N*-acetylglucosamine
GlcNAc-T	*N*-acetylglucosaminyltransferase
H	in *Chapter III*: heavy (IgG) chain in *Chapter IV*: hexose
H&E	hematoxylin and eosin
HCC	hepatocellular carcinoma
HGSOC	high-grade serous ovarian carcinoma
HIAR	heat-induced antigen retrieval
HIV	human immunodeficiency virus
HILIC	hydrophilic interaction liquid chromatography
HOBt	1-hydroxybenzotriazole
Ig	immunoglobulin
IgG	immunoglobulin G
IL	interleukin
ITAM	immunoreceptor tyrosine-based activating motif
ITH	intra-tumoral heterogeneity
ITIM	immunoreceptor tyrosine-based inhibitory motif
ITO	indium tin oxide
IVIG	intravenous immunoglobulin
K	potassium
K_d	dissociation constant
L	light (IgG) chain
LC	liquid chromatography
LGSOC	low-grade serous ovarian carcinoma
MAL-I	*Maackia amurensis I* lectin
MALDI	matrix-assisted laser desorption/ionization
Man	mannose
MBL	mannan-binding lectin
MC	mucinous carcinoma
Monogal	monogalactosylation
MUC16	mucin 16
MS	mass spectrometry
MSI	mass spectrometry imaging
m/z	mass-to-charge ratio
N	in *Chapter III*: bisecting *N*-acetylglucosamine in *Chapter IV*: *N*-acetylhexosamine
Na	sodium
NaOH	sodium hydroxide
Neu5Ac	*N*-acetylneuraminic acid

Neu5Gc	*N*-glycolylneuraminic acid
NK	natural killer cell
OC	ovarian cancer
OCC	ovarian clear cell carcinoma
OST	oligosaccharyltransferase
PAGE	polyacrylamide gel electrophoresis
PBS	phosphate-buffered saline
PGC	porous graphitic carbon
PLCO	Prostate, Lung, Colorectal, and Ovarian Cancer Screening Trial
PSA	prostate-specific antigen
PNGase F	peptide-*N*-glycosidase F
PTM	post-translational modification
RA	rheumatoid arthritis
ROC	receiver operating characteristic
ROI	region of interest
rpm	revolutions per minute
S, Sia	sialic acid
SD	standard deviation
SDS	sodium dodecyl sulfate
Ser	serine
Sial	sialylation
sLe^X	sialyl-Lewis X antigen
SNA	*Sambucus nigra* lectin
SOC	serous ovarian carcinoma
SPE	solid-phase extraction
ST3Gal	α2,3-sialyltransferase
ST6Gal	α2,6-sialyltransferase
TIC	total ion count
TFA	trifluoroacetic acid
Thr	threonine
TMA	tissue microarray
TOF	time-of-flight
TVUS	transvaginal ultrasound
UDP	uridine diphosphate
UPLC	ultra-performance liquid chromatography
V_H	variable domain of heavy (IgG) chain
V_L	variable domain of light (IgG) chain

Table of Contents

Chapter I General introduction

1. Ovarian cancer

1.1. Incidence, staging, and mortality rates

According to the latest statistics, each year approximately 300.000 women worldwide are diagnosed with ovarian cancer (OC) and 180.000 succumb to this disease. Thus, even though OC is rather rare as compared to other malignancies, it is the fifth most common cause of female cancer death and the leading cause of cancer death among gynecological malignancies in women [1, 2]. This particularly high mortality is primarily due to inadequate early detection that results from vague, late-occurring disease symptoms and a lack of accurate early diagnostic markers.

The key predictor of OC mortality is the stage of the disease at diagnosis. According to the 2014 International Federation of Gynecology and Obstetrics (FIGO) classification system [3] that is based on findings from surgical explorations, OC is categorized into four main stages:

- *Stage I* – the cancer is confined to one or both ovaries;
- *Stage II* – the cancer has spread within the pelvic region, e.g., to fallopian tubes, uterus;
- *Stage III* – the cancer has spread beyond the pelvic region, e.g., to abdomen lining, nearby lymph nodes;
- *Stage IV* – the cancer has metastasized to distant sites and organs, e.g., spleen, lungs, liver.

Importantly, when detected and treated in stage I, OC is highly curable and consequently is associated with five-year survival rates exceeding 90%. Nevertheless, over 70% of OC patients present with an advanced-stage III or IV disease, in which five-year survival rates are 39% and 17%, respectively, and the risk of disease recurrence increases to 70-95% [4]. Notably, the poor prognosis for OC has hardly changed in the last decades, despite a better understanding of its etiology and clinical behavior, advances in treatment, and great efforts to improve screening strategy.

1.2. Histological heterogeneity and classification

It is now well recognized that, instead being a single disease entity, OC comprises a histologically and molecularly heterogeneous group of diseases. In 2014, World Health Organization categorized OC into four major subtypes, i.e., epithelial, germ cell, sex-cord stromal, and mixed-cell type (*Figure 1*), based on the etiology of cancer-initiating cell [5]. Germ cell and sex-cord stromal carcinomas that arise from primitive germ (egg) cells and sex-cord or stromal cells, respectively, are fairly rare and comprise less than 15% of all OCs combined. In the majority of cases, these tumor types affect young women and present in the early stage, which translates to their overall good prognosis and high survival rates [6]. On the contrary, epithelial ovarian cancer (EOC), which arises from malignant transformation of the ovarian surface, peritoneum, or fallopian tube epithelium, is the most common and lethal OC histotype [7]. It accounts for 85-90% of all ovarian carcinomas and exhibits high heterogeneity in terms of histology, genetics, and clinical and biological behavior.

As indicated in *Figure 1*, EOC has been further subcategorized into five histotypes, i.e., serous ovarian carcinoma (SOC), endometrioid carcinoma (EC), ovarian clear cell carcinoma (OCC), mucinous carcinoma (MC), and malignant Brenner tumors [7]. The latter classification is primarily based on the morphological appearance of the metaplastic epithelium. Consequently, serous carcinoma resembles the serous epithelium of fallopian tubes, endometrioid carcinoma has epithelium similar to tubular endometrial glands, epithelium of clear cell carcinoma contains cells with large clear cytoplasm filled with glycogen, mucinous carcinoma has mucin-containing cells, whereas in Brenner tumors the epithelium is of transitional (stratified) type [8].

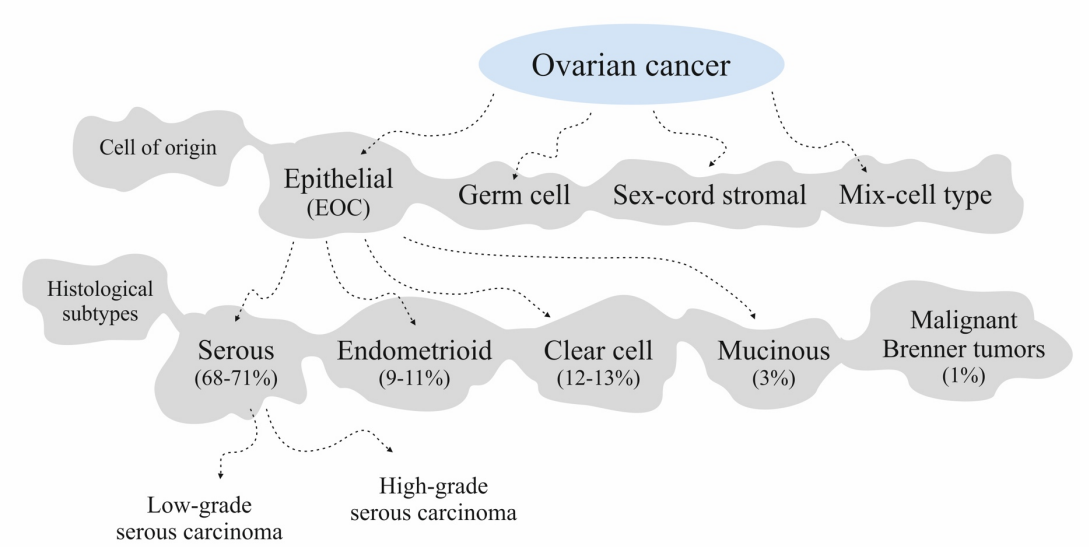

Figure 1. Classification of ovarian carcinoma based on tumor etiology and histology (modified from [7]).

It is important to note that the prevailing histotype – serous EOC – is further categorized into low- (LGSOC) and high-grade serous carcinoma (HGSOC), based on differences in their malignant potential. Interestingly, in the past, highly aggressive HGSOC was considered to arise from a well-differentiated low-grade form [9, 10]. However, accumulated findings from clinicopathological and molecular characterizations of ovarian masses revealed that LGSOC is unlikely to be a precursor lesion of HGSOC [11]. Currently, these two conditions are regarded to be separate diseases, marked by differing patterns of genomic alterations and distinct behavior [11].

In 2004, Shih and Kurman [12] proposed a dualistic model of OC pathogenesis, in which EOCs were categorized into two distinct types, type I and type II EOC. Type I EOCs that include LGSOC, OCC, most of ECs and MC are thought to arise from well-defined non-cancerous precursor lesions, among others, borderline tumors and endometriotic cysts. Type I tumors are typically characterized by indolent behavior, are unilateral and confined to the ovary at the time of diagnosis. In a majority of cases, they are diagnosed at a younger age and hence are associated with a favorable outcome. Type I tumors are relatively genetically stable and frequently harbor mutations in *KRAS*, *BRAF,* and *ERBB2* genes [7, 13].

In contrast, HGSOC that due to the lack of clearly defined precursor lesion is believed to develop *de novo* from the fallopian tube epithelium is categorized as type II EOC. HGSOC accounts for 75% of all EOCs and, in a majority of cases, is diagnosed at an advanced stage and has an aggressive clinical course. Unlike type I EOCs, HGSOC is marked by considerable genomic/chromosomal instability and ubiquitous pathogenic mutations in *TP53*, *BRCA1,* and *BRCA2* genes [7, 13].

Notably, although HGSOC was long considered the deadliest form of OC, recent data indicate that some type I EOCs, in particular distant-stage mucinous and clear cell carcinomas, might exhibit even higher mortality. Clinical evidence suggests that, due to their distinctive nature, these type I EOC histotypes are less responsive to the conventional OC treatment approach that combines cytoreductive surgery with platinum- or taxane-based chemotherapy [14]. This emphasizes the fact that proper classification of OC histotypes is crucial for the choice of an adequate treatment that maximizes patient's survival chances. Nevertheless, in some cases, the distinction between EOC histotypes can be impeded by high intra-tumoral morphological heterogeneity. As clinical routine relies on histological assessment, misdiagnosis of EOC histotype could lead to the selection of an inappropriate treatment strategy.

1.3. Ovarian cancer screening

At present, screening for OC typically consists of a combination of cancer antigen 125 (CA 125) blood test and transvaginal ultrasound (TVUS) examination.

CA 125 is a peptide epitope of MUC16, a highly glycosylated mucin-type protein, naturally expressed on the surface of cells derived from the embryonic coelomic epithelium, e.g., Müllerian ducts, the lining of the abdominal cavity, heart, and lung [15-17]. MUC16 is initially expressed as a membrane-bound protein whose extracellular part is released in a soluble form to body fluids following the proteolytic cleavage. While in healthy adults serum CA 125 concentration is usually low, the reference value of 35 U/mL is exceeded in 80% of advanced ovarian cancer patients and 50% of early-stage patients [18, 19]. The quantification of soluble CA 125/ MUC16 in peripheral blood is performed with ELISA assay, using two monoclonal anti-CA 125 antibodies, namely OC125 and M11 [20, 21]. Importantly, besides ovarian cancer, elevated levels of circulating CA 125 were also reported in other malignancies, including breast and gastric cancer [22, 23], mesothelioma [24], and non-Hodgkin lymphoma [25], as well as in various physiological and benign gynecological conditions, among others, menstruation [26], pregnancy [27], and endometriosis [28]. Hence, due to its limited specificity and low sensitivity, particularly in the early-stage disease, CA 125 is not recommended for OC screening in asymptomatic women [29].

Besides the serum CA 125 test, screening for OC typically employs transvaginal ultrasound (TVUS), which was proven highly accurate in detecting changes in ovarian morphology and volume. As compared to transabdominal ultrasonography, TVUS enables a more precise and detailed lesion

assessment [30]. Nevertheless, TVUS is only moderately reliable in discriminating benign and malignant ovarian tumors, which makes it prone to false-positive assessments that increase the risk of unnecessary surgery and psychological distress [30]. Furthermore, as a highly operator-dependent technique, TVUS is susceptible to interpretive errors.

At present, annual screening for OC is performed only in high-risk women and is not recommended in the general population. In previous screening programs, including the 19-year follow-up US Prostate, Lung, Colorectal, and Ovarian (PLCO) Cancer Screening Trial with more than 78000 participants, annual screening with CA 125 marker and TVUS showed no decrease in OC mortality as compared to standard care.

Hence, massive efforts are being undertaken to discover a novel and more effective screening mechanism for early-stage OC that would allow detecting the disease prior to the onset of clinical symptoms. In terms of serum-based screening tools, the common approach to improve the diagnosis efficiency is to use a combination of few serum proteins. For instance, one of the newest Food and Drug Administration (FDA)-approved serum-based screening tests for ovarian cancer, OVA1, combines five well-established markers, i.e., CA 125, transthyretin, apolipoprotein A1, beta-2 microglobulin, and transferrin [31]. Nevertheless, as far as OVA1 was shown to outperform CA 125 in presurgical assessment, its score can be interfered with by high levels of serum triglycerides and rheumatoid factors. Additionally, its clinical use might be hindered by relatively high costs that amount to roughly $650 per patient [32].

Significantly, OC was shown to be accompanied by glycosylation alterations occurring both at the level of serum-contained soluble proteins as well as membrane-bound proteins decorating the surface of cancer cells. In absence of reliable and clinically accepted tests for early OC detection, these alterations attracted great attention as a source of novel complementary screening markers.

2. Glycosylation

Glycosylation, which is an attachment of a carbohydrate moiety to the target macromolecule, is one of the most common co- and post-translational modifications (PTMs) occurring in proteins and lipids. Glycans are more than energy suppliers, indeed, they play a broad range of important roles within organisms. All eukaryotic cells are covered with a dense glycan-rich coating, called “glycocalyx”, which allows maintaining proper structure, integrity, and porosity of the tissue. Apart from providing a protective shield, glycans are known to mediate and modulate various essential events that involve cell-molecule, cell-cell, and cell-matrix interactions [33]. For instance, during embryonic neurodevelopment, negatively charged carbohydrate components inhibit adhesion of cells, which is necessary for retaining neuronal plasticity and migration [34]. On the other hand, the endothelial glycocalyx that coats the lumenal surface of blood vessels is known to modulate the recruitment of leukocytes during the inflammatory response [35]. Structural, protective, and

modulatory effects of attached glycans are also visible at the protein level, as they were shown to influence protein activity, stability, solubility, and folding [36]. Additionally, by causing steric hindrance and/or introducing a negative charge, dense glycosylation protects proteins against protease cleavage. This effect is particularly apparent in highly glycosylated mucins that line the gastrointestinal tract [37, 38]. Glycosylation is regarded as the most diverse form of PTMs, and its classification is based on the identity of the structure (e.g. atom) to which the oligosaccharide chain is attached to as well as on the type of glycoconjugate that it forms. In humans, protein glycosylation typically occurs as *N*-glycans, *O*-glycans, and proteoglycans that give rise to a broad spectrum of membrane-bound and secretory glycoproteins. In *N*-glycans, oligosaccharide structures are linked to proteins via a nitrogen atom of certain asparagines, whereas, in *O*-glycans, they are linked via an oxygen atom of serine's and threonine's side chains. In proteoglycans, glycans actually form long and linear glycosaminoglycan chains composed of repeating disaccharide units that are covalently linked to a protein core. Although like *O*-glycans, glycosaminoglycan chains are linked via an oxygen atom to protein's serine and threonine residues, they are regarded as a separate group due to their distinct biosynthetic pathway and structure.

2.1. *N*-Glycans

Among different types of glycosylation, *N*-glycosylation is the most commonly observed and studied one. *N*-Glycans are attached to a protein backbone at asparagine (Asn) residues that constitute a part of the consensus sequence Asn-X-Ser/Thr, where X can be any amino acid except proline. The name "*N*-glycan" refers to the fact that the glycosidic bond linking the glycan to the protein is formed via the nitrogen atom of an Asn side chain. Despite the large variety of their final structures, human *N*-glycans are made of only seven monosaccharides, of which six are neutral and one is acidic. Neutral human monosaccharides consist of glucose (Glc), galactose (Gal), mannose (Man), fucose (Fuc), *N*-acetylglucosamine (GlcNAc), and *N*-acetylgalactosamine (GalNAc), whereas the lone negatively charged acidic monosaccharide is *N*-acetylneuraminic acid (Neu5Ac) [39]. Chemical structures of all monosaccharides composing human *N*-glycans, together with their notations proposed by Consortium for Functional Glycomics (CFG), are depicted in *Figure 2*.

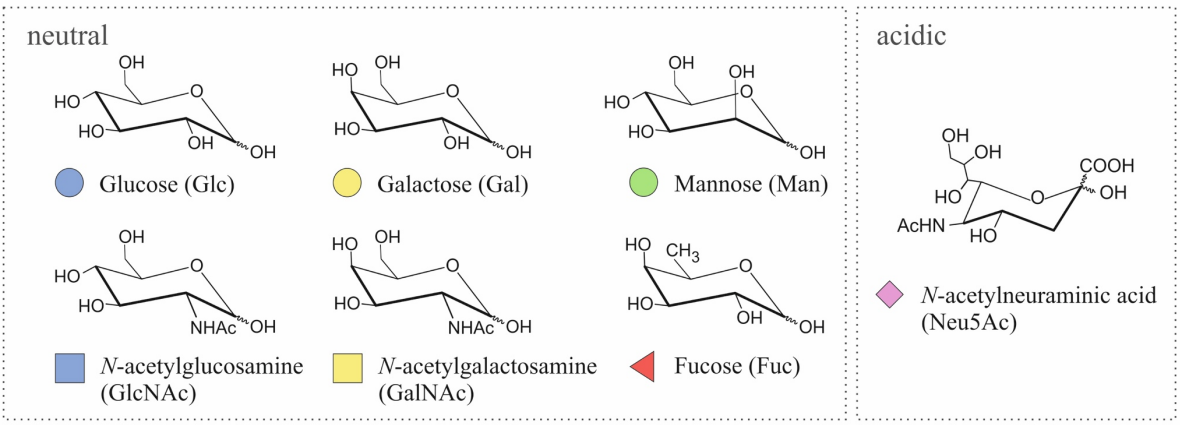

Figure 2. Chemical structures and symbolic representations of N-glycan monosaccharides in humans.

Interestingly, a majority of non-human mammals, e.g., mice and cows, synthetize as well another acidic monosaccharide that is closely related to Neu5Ac, namely *N*-glycolylneuraminic acid (Neu5Gc). Even though the gene inactivation that occurred around 2-3 million years ago irreversibly deprived humans of the ability to synthetize Neu5Gc, its trace amounts can still be found in human tissues [40]. It has been reported that the majority of the Neu5Gc detected in humans is being incorporated from dietary sources such as red meat and dairy products [41]. Due to the fact that Neu5Gc is present in humans in only negligible amounts making Neu5Ac a lone representant of sialic acids, in the following chapters, terms Neu5Ac and sialic acid will be used interchangeably.

As shown in *Figure 3*, all *N*-glycans share an identical pentasaccharide core composed of three mannoses and two *N*-acetylglucosamines, abbreviated as $Man_3GlcNAc_2$. Based on the further elongation of this core structure, *N*-glycans are divided into three subtypes:

- *Oligo- /High-mannose-type* – only mannoses are attached to the core;
- *Complex-type* – one or more antenna(e) initiated with GlcNAc residue are attached to the core;
- *Hybrid-type* – the α(1-6) arm of the core is decorated exclusively with mannose residues, whereas the α(1-3) arm is terminated with complex-type antenna(e).

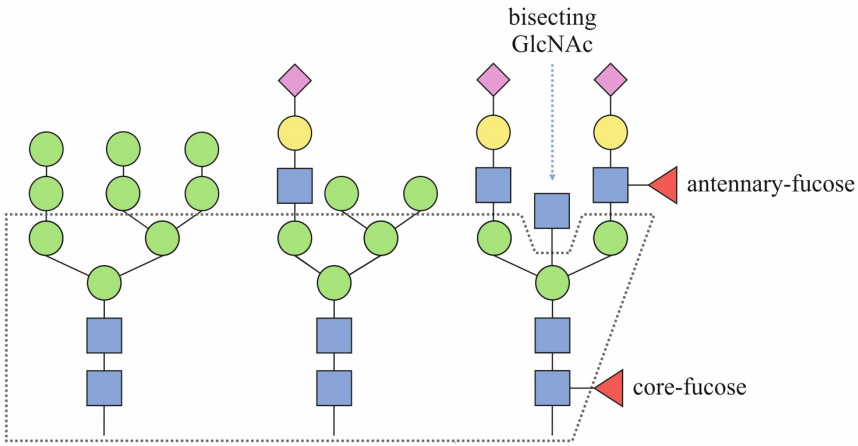

Figure 3. Three types of N-glycans: oligomannose (left), hybrid (middle), and complex (right). All N-glycans share an identical pentasaccharide core $Man_3GlcNAc_2$ indicated by a black dashed line.

Complex- and hybrid-type *N*-glycans can be further extended by the addition of fucose residue, which can be attached either via an α1,6-linkage to the innermost core-GlcNAc ("core-fucose") or via an α1,3-linkage to the antennary GlcNAc ("antennary-fucose"). Moreover, complex-type *N*-glycans might contain an additional GlcNAc residue attached via a β1,4-linkage to the innermost core-mannose, which is referred to as a "bisecting GlcNAc". Unlike GlcNAc that initiates a complex antenna, bisecting GlcNAc is never further extended [39].

2.2. *N*-Glycan biosynthesis

Unlike DNA transcription and protein translation, the biosynthesis of glycans is a non-templated process. It relies on the activity of membrane-bound enzymes such as glycosyltransferases and glycosidases, distributed within the endoplasmic reticulum (ER) and the Golgi apparatus, as well as the accessibility of specific monosaccharide precursors. Despite its complexity, the process of *N*-glycan biosynthesis is currently quite well understood, primarily due to extensive studies performed on genetic mutants of yeast *Saccharomyces cerevisiae* [42].

The process of glycosidic bond formation that accompanies the attachment of monosaccharide residues is energetically demanding. To power this reaction, monosaccharide units are firstly converted into nucleotide-activated sugar donors and dolichol-phosphate-linked sugars, whose subsequent hydrolysis by respective glycosyltransferases provides the required energy. The majority of nucleotide activated-sugars are synthetized in the cytoplasm and contain two phosphate groups (diphosphate, DP). Among them, mannose and fucose are known to form guanidine-diphosphate sugar nucleotides (GDP-Man, GDP-Fuc), whereas *N*-acetylglucosamine, *N*-acetylgalactosamine, glucose, and galactose form uridine-diphosphate sugar nucleotides (UDP-GlcNAc, UDP-GalNAc, UDP-Glc, UDP-Gal). The activated sugar donor of sialic acid is synthetized in the nucleus and contains only one phosphate group (cytidine-monophosphate-Neu5Ac, CMP-Neu5Ac). Dolichol-phosphate-linked monosaccharides such as Dol-P-Man and Dol-P-Glc are used during glycan elongation steps that take place on the lumenal surface of the ER membrane. Both, Dol-P-Man and Dol-P-Glc are formed at the cytoplasmic surface of the ER membrane by translocating Man and Gal from, respectively, GDP-Man and UDP-Glc to Dol-P. Then, they are flipped as complexes across the ER membrane to its lumenal side [43].

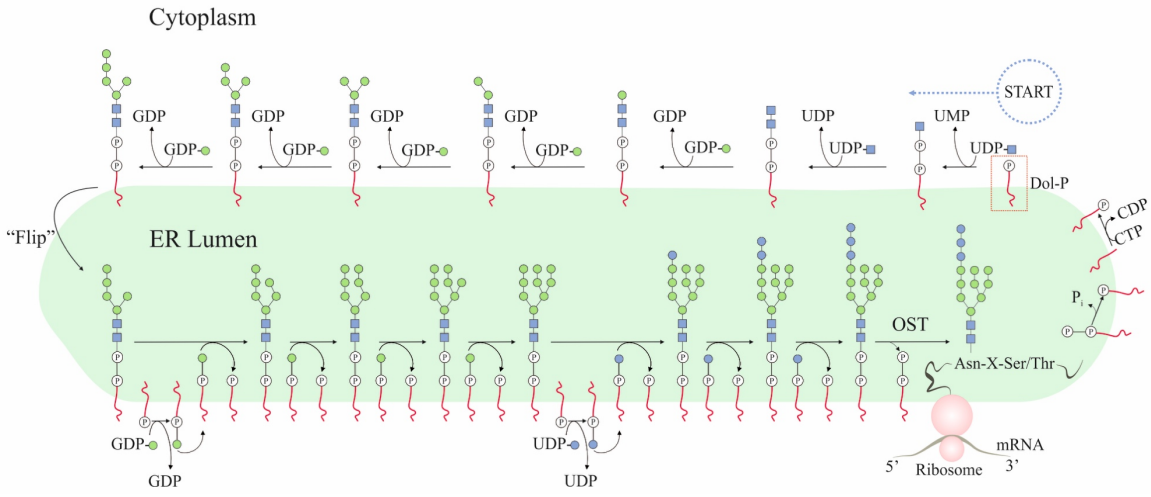

Figure 4. Initial steps of N-glycan biosynthesis and the following transfer of the N-glycan precursor to the nascent protein. Dol-P – dolichol phosphate, OST – oligosaccharyltransferase, P_i – phosphate group (modified from [43]).

As shown in *Figure 4*, in eukaryotes, the biosynthesis of *N*-glycans initiates on the cytoplasmic surface of the ER membrane, where GlcNAc-1-phosphate (GlcNAc-1-P) is transferred from UDP-GlcNAc to the lipid carrier dolichol-phosphate (Dol-P). This step is catalyzed by GlcNAc-1-phosphotransferase and results in the formation of dolichol-diphosphate *N*-acetylglucosamine (GlcNAc-P-P-Dol). Generated GlcNAc-P-P-Dol is extended by the stepwise addition of six residues, namely one GlcNAc and five mannoses, transferred by specific glycosyltransferases from UDP-GlcNAc and GDP-Man, respectively. The resulting $Man_5GlcNAc_2$-P-P-Dol translocates across the ER membrane with the help of an enzyme called "flippase". Once in the ER lumen, the glycan is further extended by the addition of four mannoses and three glucose residues, transferred from Dol-P-Man and Dol-P-Glc, respectively. This generates the fourteen-monosaccharide long glycan ($Glc_3Man_9GlcNAc_2$), shown in *Figure 5*, which is *en bloc* transferred from Dol-P-P to Asn residue in Asn-X-Ser/Thr sequence within a nascent polypeptide translocating into the ER. This central step of *N*-glycan biosynthesis is catalyzed by a large enzymatic complex, oligosaccharyltransferase (OST), which cleaves the GlcNAc-P bond.

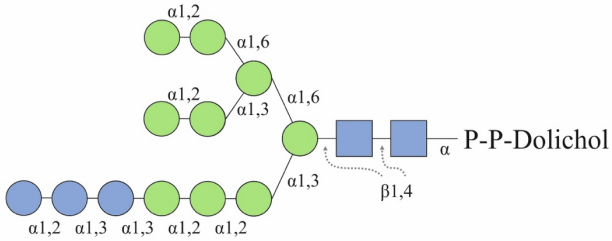

Figure 5. The structure of the fourteen-monosaccharide long N-glycan precursor attached to P-P-Dol. Once transferred onto the protein, the innermost GlcNAc is attached via a β1-glycosidic linkage to a nitrogen atom of the Asn, at the Asn-X-Ser/Thr consensus glycosylation motif.

Released Dol-P-P is de-phosphorylated and the remaining Dol-P is recycled to the cytoplasmic face of the ER in order to be reused [43]. As shown in *Figure 6*, the *N*-glycan attached to the polypeptide chain is trimmed by sequential removal of three glucose residues, which steps are catalyzed by the exoglycosidases α-glucosidase I and II. At this point, the trimmed *N*-glycan interacts with ER-resident chaperones, calnexin and calreticulin, which control the proper folding of the nascent glycoprotein. Misfolded glycoproteins are re-glucosylated, which prolongs their retention in the ER and allows repeating the folding cycle. Once the correct folding is accomplished, the re-attached glucose residue, together with the mannose terminating the central arm of $Man_9GlcNAc_2$, are trimmed by α-glucosidase II and α-mannosidase I, respectively. The resulting glycoprotein, decorated with $Man_8GlcNAc_2$, is transferred to the cis-Golgi, where a series of α-mannosidases remove three mannose residues, forming $Man_5GlcNAc_2$. A small portion of glycoproteins escapes the above-mentioned remodeling pathway in the cis-Golgi and mature with *N*-glycans of high-mannose-type ($Man_{5-9}GlcNAc_2$). In most cases, however, nascent glycoproteins translocate further to the medial-Golgi, where high-mannose glycans serve as substrates for the synthesis of hybrid- and complex-type *N*-glycans.

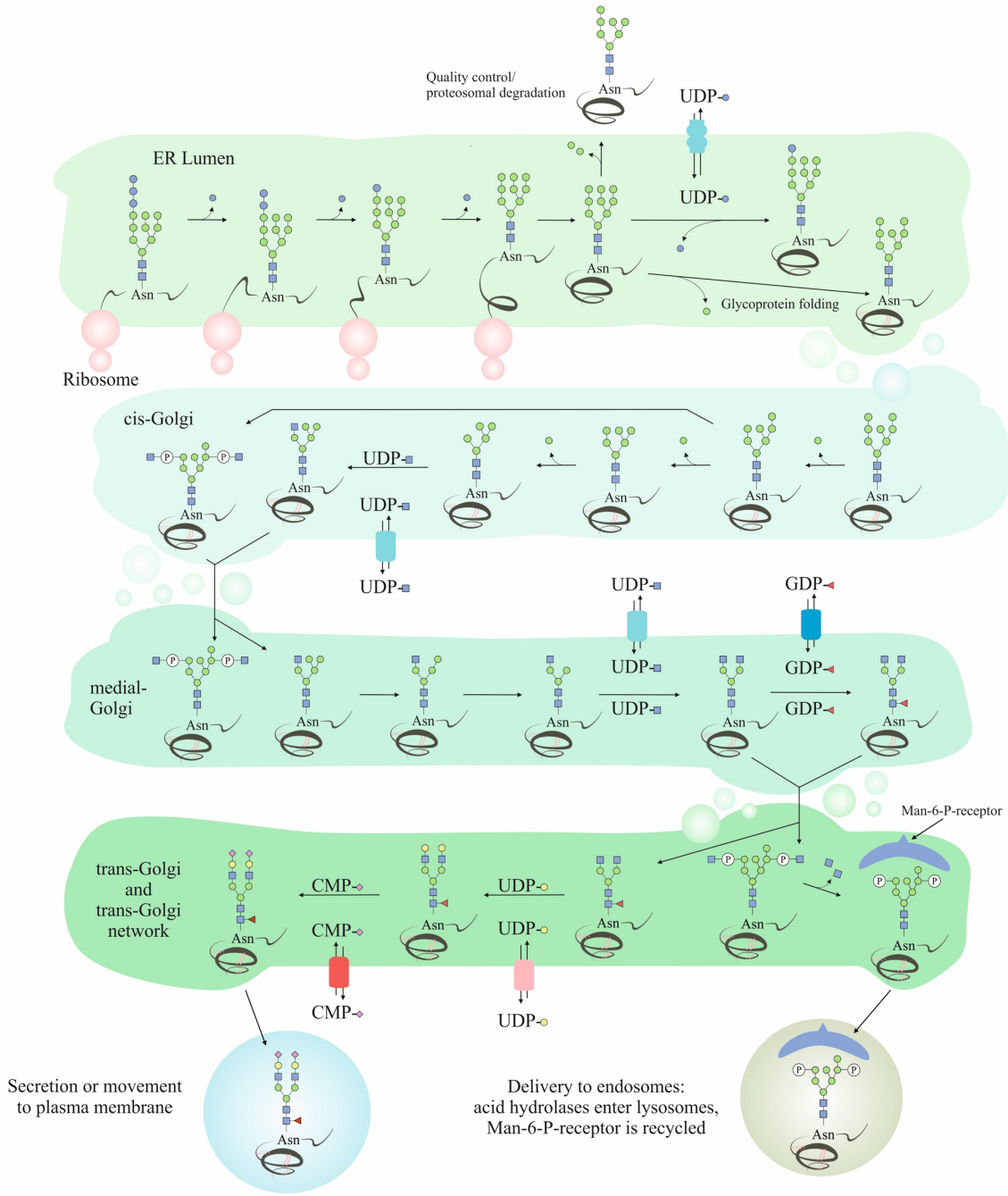

Figure 6. Further processing of an Asn-attached N-glycan in the ER and the Golgi apparatus (modified from [43]).

In the following steps, $Man_5GlcNAc_2$ oligosaccharides are extended by the addition of a GlcNAc residue to the α1,3-linked core-mannose, catalyzed by *N*-acetylglucosaminyltransferase (GlcNAc-T)-I. Subsequently, α1,3-Man and α1,6-Man terminating the second arm are cleaved by α-mannosidase II, leading to the formation of $GlcNAcMan_3GlcNAc_2$. Incomplete processing of the latter step leads to the generation of glycoproteins carrying hybrid-type *N*-glycans, with the GlcNAc attached to the α1,3-core-mannose initiating the antenna and one or more mannose residues attached to the α1,6-linked mannose. In most cases, however, the $GlcNAcMan_3GlcNAc_2$ structure is processed to complex-type *N*-glycans, which begins with the addition of a second GlcNAc to the

α1,6-linked core-mannose, catalyzed by GlcNAc-T-II. The resulting simplest complex-type *N*-glycan, $GlcNAc_2Man_3GlcNAc_2$, is usually further modified by the addition of other branches, elongation of antenna(e), or the addition of fucose. Further branching is achieved by activities of different GlcNAc-Ts (IV-VI) that catalyze the addition of GlcNAc residues to either α1,3- or α1,6-linked core-mannoses, leading to the formation of tri- and tetraantennary *N*-glycans. In turn, GlcNAc-T-III catalyzes the addition of a GlcNAc residue to the β-linked mannose, generating bisecting *N*-glycans. In vertebrates, *N*-glycans are frequently decorated with fucose residues that are either α1,6-linked to the innermost GlcNAc residue, forming "core-fucose", and/or α1,3-linked to antennary GlcNAc residues. Finally, nascent glycoprotein *N*-glycans move to the trans-Golgi, whereby antennary GlcNAcs usually become capped with β1,4-linked galactoses and α2,3- or α2,6-linked sialic acids. These elongation steps are catalyzed by specific galactosyltransferases, α2,3-sialyltransferases (ST3Gal-I to ST3Gal-VI), and α2,6-sialyltransferases (ST6Gal-I and ST6Gal-II), respectively [43].

As shown above, the structural diversity of generated *N*-glycans results from a concerted action of glycosyltransferases and glycosylhydrolases that build and remodel their structure as well as the accessibility of sugar donors. While initial steps of *N*-glycan biosynthesis are quite conserved among various proteins, the following processing in the Golgi apparatus exhibits a broader diversity. Among other factors, the nature of attached *N*-glycans was shown to vary depending on the destination of the carrier glycoprotein within the cell. For instance, in the case of acid hydrolases that are destined for lysosomes, the $Man_7GlcNAc_2$ located in the cis-Golgi escapes a typical *N*-glycan processing pathway (*Figure 6)* and acquires GlcNAc-1-P extensions on its distant mannose residuals. This modification is crucial for the guidance of the protein to a prelysosomal compartment [43].

2.3. *N*-linked glycosylation in cancer

Since glycosylation plays a variety of important roles within an organism, it is not surprising that changes in glycan structures and compositions have been observed to accompany a number of pathological conditions including cancer. Although in many cases it is still unclear whether disease-related glycosylation alterations are a cause or a result of the disease, their investigation can help understanding disease mechanisms and ultimately aid disease diagnosis and treatment.

Altered glycosylation of proteins was shown to play an important role in various steps of malignant transformation and tumor progression and is frequently referred to as the next hallmark of cancer [44, 45]. Notably, cancer-associated glycosylation changes have been detected in cancer cells and tissues as well as in serum/plasma proteins of cancer patients. As such, glycosylation alterations have the potential to serve as a source of cancer biomarkers and targets for drug therapy.

2.3.1. Serum-related glycosylation in cancer

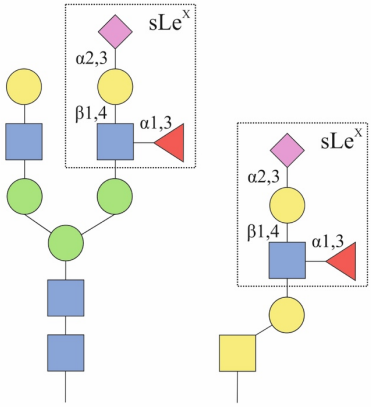

Figure 7. Sialyl-Lewis X antigen on (left) the N- and (right) the O-glycan.

Cancer-associated changes in total serum *N*-glycome have been investigated in various malignancies, e.g., breast, ovarian, lung, bladder, and prostate cancer, revealing a common profile of altered core- and/or antennary-fucosylation, increased antennarity (β1,6-branching) and sialylation [46-50]. In particular, the total serum *N*-glycome of cancer patients was reported to contain increased levels of certain Lewis blood group-related antigens, among others, sialyl-Lewis X (sLe^X), which is schematically represented in *Figure 7* [51, 52]. Notably, these serum *N*-glycome alterations were shown to primarily derive from acute-phase proteins produced in the liver, such as α1-acid glycoprotein, α1-antichymotrypsin, and haptoglobin, whose concentration increases in the presence of cancer [53, 54]. However, to a smaller extent, they might also reflect changes that occur directly within the tumor, as cancer cells were shown to express α1-acid glycoprotein and sLe^X antigens and to shed/secrete surface proteins into the blood [55, 56].

Importantly, in the case of certain low abundant serum glycoproteins, aberrant glycosylation was observed to correlate with tumor development and progression, making them promising biomarker candidates. For instance, increased fucosylation of α-fetoprotein (AFP) was found to be strongly related to hepatocellular carcinoma (HCC) progression. In fact, the ratio of α1,6-fucosylated AFP fraction (AFP-L3) to total AFP was superior to AFP alone at discriminating between HCC patients and healthy controls [57, 58]. Due to its improved performance, in 2006, FDA approved the AFP-L3/AFP ratio as an improved biomarker for HCC. Similarly, determination of α2,3-sialylation of prostate-specific antigen (PSA) rather than the measurement of total PSA concentration in blood, was shown to improve early detection of prostate cancer and to refine discrimination between its aggressive and non-aggressive form [59, 60].

Cancer-associated glycosylation changes were also detected in immunoglobulin G (IgG), which is a representative protein of the immune system and, at the same time, the most abundant glycoprotein in human serum. As described in detail in *Chapter III*, IgG glycosylation is an important modulator of IgG structure and function, and its changes were reported to accompany various physiological and pathological conditions. Total serum IgG glycosylation profile has been investigated in a number of malignancies, including gastric, ovarian, colorectal, lung, and prostate cancer, revealing significant differences between cancer patients and healthy controls [61-65]. Notably, IgG-specific cancer-related glycosylation alterations were distinctly different from those observed in liver-originated serum proteins. In fact, malignant diseases were uniformly accompanied by a decreased level of IgG galactosylation, an abnormality that was first described in rheumatoid arthritis patients [66]. As reported by Ren et al. [67], the distribution of IgG galactosylation, determined as a ratio of

agalactosylated to mono- and digalactosylated IgG structures (Gal-ratio), was shown to increase in all twelve investigated cancer types. As far as this indicates that decreased IgG galactosylation is neither disease nor cancer type-specific, the Gal-ratio showed the potential to aid cancer diagnostics and to serve as a pan-cancer marker since it outperformed routinely used biomarkers in discriminating cancer and non-cancer patients [67]. Besides galactosylation, cancer development and progression were also shown to be associated with changes in other IgG glycosylation traits. For instance, in gastric cancer, an increase in IgG core-fucosylation and a decrease in bisecting GlcNAc correlated with disease progression [68], whereas in large-scale colorectal cancer (CRC) study, a decrease in IgG galactosylation was accompanied by decreased sialylation of fucosylated structures and an increase in bisecting GlcNAc, all of which were strongly associated with CRC mortality [63]. As described in *Chapter III*, a decrease in galactosylation and sialylation as well as an increase in bisecting GlcNAc converts IgG molecule into pro-inflammatory phenotype by facilitating complement activation via binding to mannose-binding lectin (MBL). It has been suggested that increased expression of pro-inflammatory IgG molecules provides the host's defense response to the presence of malignancy [69].

2.3.2. Cellular glycosylation in cancer

In cancer cells, increased activity of fucosyltransferases (FUTs) was shown to correspond to increased metastatic and invasive phenotypes [70-72]. In line with this data, *in vitro* and *in vivo* experiments demonstrated that inhibition of fucosylation results in a reduction of tumor growth and metastasis [73, 74]. This effect can be explained by the fact that enhanced expression of certain FUTs (FUT 3, 5, 6, and 7) is directly associated with increased expression of sLe^X antigens (*Figure 7*), which are ligands of cell adhesion molecules, E-selectins. By elevating the number of sLe^X antigens, increased fucosylation facilitates E-selectin-dependent binding of cancer cells to the activated endothelium, which eventually leads to their extravasation and spreading within the body [75].

Besides increased fucosylation, cancer cells are frequently characterized by increased β1,6-branching that was shown to result from overexpression of GlcNAc-T-V, an enzyme attaching GlcNAc residues on the α1,6-mannose. In murine tumor models, enhanced β1,6-branching was observed to positively correlate with invasiveness and metastatic potential of cancer cells [76]. Additionally, *N*-glycan branching was shown to be essential for sustaining cancer cell proliferation. Precisely, tri- and tetra-antennary *N*-glycans decorating growth-promoting receptors (e.g., epidermal-, insulin-like-, and fibroblast growth factor receptor) localized on the surface of cancer cells are able to interact with galectin-3. This leads to the formation of molecular lattices that prevent receptors' internalization and endocytosis [77, 78]. In consequence, growth-promoting receptors retained at the cell surface continuously supply cancer cells with proliferative signals, leading to disease progression.

Aberrant sialylation has been observed in numerous malignancies, and its cancer-related increase was shown to arise from enhanced expression/activity of sialyltransferases, increased production of sialylated glycoproteins, and reduced activity of sialidases [79]. Accumulation of sialylated glycans on the surface of cancer cells increases the local negative charge and, in consequence, disrupts cell-cell adhesion. In this manner, increased sialylation promotes detachment of cancer cells from the tumor mass, facilitating their spread in the body [80]. Additionally, an increase in α2,3-sialylation typically translates to increased abundance of sLe^X antigens (*Figure 7*), which, as described above, mediate cancer cell adhesion to the vascular endothelium and promote their invasive character [81, 82]. Accordingly, Cui et al. [83] reported that the level of α2,3-sialylation corresponds to metastatic potential and migration ability of three human breast cancer cell lines. Besides α2,3-sialylation, a tumor-associated increase in sialylation is also manifested by increased α2,6-sialylation [84]. Its cognate glycosyltransferase – ST6Gal-I – was shown to be overexpressed in acute myeloid leukemia, cervical carcinoma, gastric, ovarian, colon, and some brain tumors [85-90]. In breast cancer, high expression of ST6Gal-I was observed to correlate with poor prognosis [91], whereas in ovarian cancer it was associated with resistance to cisplatin-based chemotherapy [88]. Interestingly, Dall'Olio et al. [92], who studied the hepatic expression of ST6Gal-I in HCC patients, showed that ST6Gal-I expression and activity can vary greatly between individuals suffering from the same cancer type. While in most HCC tissue homogenates ST6Gal-I was clearly overexpressed, in some probes ST6Gal-I expression was strongly reduced when compared to healthy controls. Moreover, Dall'Olio et al. [92] demonstrated that even within the same tumor sample, ST6Gal-I can be up- or downregulated within different groups of cells. This heterogeneity was suggested to reflect activation of different oncogenic pathways and varied cancer cell's differentiation stage, as lower ST6Gal-I expression was detected in less differentiated HCC specimens [92].

Besides alterations in fucosylation, branching, and sialylation, cancer development and progression were shown to be associated with an increase in high-mannose *N*-glycans, which suggests premature and/or failure termination of the *N*-glycosylation pathway. Among others, increased abundance of high-mannose *N*-glycans was reported in bladder, head and neck, breast, and colon cancer [93-96].

3. Protein *N*-glycosylation analysis

Due to their enormous structural diversity, elaborate biosynthesis, and numerous technical limitations, the analysis of glycans has lagged far behind those of proteins and nucleic acids. Fortunately, recent advances in understanding pivotal roles of glycosylation have placed a renewed emphasis on detailed glycan analysis, leading to the development of technologies that helped to expand our knowledge of the glycome, the entire collection of carbohydrates within the body.

3.1. Analytical approaches

Depending on the research question, protein *N*-glycosylation can be investigated at three different levels, namely at the level of intact glycoprotein, glycopeptide, and/or released *N*-glycan [97]. Analysis of intact protein glycosylation, the so-called top-down approach, is fast and straightforward, as it does not require prior enzymatic digestion. It is usually performed on glycoproteins that have been enriched or purified, for example, by means of lectin or antibody affinity binding, protein precipitation, or molecular weight cut-off ultrafiltration. Alternatively, they are separated via liquid chromatography (LC) techniques [98]. The final measurement is typically performed using mass spectrometric instruments equipped with an electrospray ionization (ESI) source that enables the mass determination of large biomolecules. However, while intact glycoprotein analysis might provide general information about the protein's molecular weight and the presence or absence of major modifications such as glycosylation, it does not allow for more detailed structural characterization via mass spectrometric techniques due to resolution limitations. Also, as direct analysis of intact (glyco)proteins frequently generates mass spectra that are complex and difficult to interpret, this strategy has been limited to small glycoproteins [99].

Contrarily, glycosylation analysis at the glycopeptide level requires proteolytic digestion of the protein backbone. This step is usually accomplished with the help of trypsin, a serine protease of high specificity that cleaves the amino acid chain at the carboxyl side of lysine and arginine residues. After tryptic digestion, glycopeptides are usually enriched via hydrophilic interaction chromatography (HILIC) or size-exclusion chromatography in order to improve their detection over non-glycosylated peptides. Then, they are analyzed by chromatographic and/or mass spectrometric techniques. The biggest advantage of this approach is the fact that the generated information is site-specific and hence allows determining both *N*-glycan structures and their exact positions within the protein. This is of particular importance when analyzing glycosylation of proteins that carry more than one glycosylation site, like in the case of immunoglobulin G (Fc- and Fab-glycosylation).

Monosaccharide composition, glycosidic linkages, and the relative abundance of *N*-glycans within a mixture can be accurately determined by performing the analysis at the level of released glycans. *N*-Glycan release can be achieved by either chemical or enzymatic methods. Chemical methods are cost-effective but usually lack specificity and hence lead to the simultaneous release of different types of glycans. One of the most known chemical release methods is hydrazinolysis [100], typically performed in anhydrous hydrazine at 90 °C for 4 h. Hydrazinolysis releases glycans in their non-reduced form, making them suitable for further labeling/derivatization. Nevertheless, anhydrous hydrazine is highly toxic and unspecific, as it may release both *N*- and *O*-linked glycans. Additionally, hydrazinolysis causes partial de-*N*-acetylation of GlcNAc and therefore must be followed by a re-*N*-acetylation step [100]. Enzymatic release of *N*-glycans is performed using substrate-specific glycosidase enzymes, including peptide-*N*-glycosidase F (PNGase F),

endoglycosidase F, and endoglycosidase H [101]. Among them, PNGase F is the most commonly used, which is owed to its broad specificity (it releases all types of *N*-glycans, except those carrying α1,3-linked core-fucose) and high activity. Also, as PNGase F cleaves the glycosidic bond between the innermost GlcNAc and an asparagine residue on the protein, it allows releasing and profiling the intact *N*-glycan. Enzymatic release of *N*-glycans is frequently preceded by glycoprotein denaturation that facilitates access to buried *N*-glycosylation sites. Released *N*-glycans are subsequently purified on the basis of their hydrophilic character and measured by means of LC, mass spectrometry (MS), or capillary electrophoresis (CE). Nevertheless, it should be noted that while the analysis of enzymatically released *N*-glycans is the most commonly used approach, it usually provides no information about the originating glycosylation site. In the case of PNGase F, however, the removal of *N*-glycan is accompanied by a deamination of asparagine to aspartic acid, which results in a specific mass-to-charge ratio (*m/z)* shift. When combined with protein sequencing, this conversion can be utilized to determine the location of the *N*-glycosylation site [101].

3.2. Analytical techniques

The most frequently used analytical techniques for glycomic analysis are MS, CE, ultra-performance liquid chromatography (UPLC), lectin arrays, and 2D gel electrophoresis [99]. As a non-targeted and sensitive analytical method, MS is a well-suited and preferred tool for glycan profiling [102]. It allows an analysis of complex mixtures of unknown compounds, whose structure is determined based on their *m/z* and, when needed, their fragmentation spectra acquired in tandem MS mode. Nevertheless, the distinction of structural isomers (i.e., structures of identical mass but different atom arrangement), requires the use of further techniques, e.g. CE, which separates *N*-glycans based not only on their mass but also on their topology [103].

3.2.1. MALDI-TOF-MS

For the purpose of glycosylation analysis, one of the most widely used ionization techniques is matrix-assisted laser desorption/ionization (MALDI), in which analyte ionization is accomplished with the help of a laser and a matrix. The matrix is a low molecular weight substance that absorbs at the wavelength of the laser and passes the excess of energy to the analyte. There are several MALDI matrixes available, with super DHB (s-DHB, a 9:1 mixture of 2,5-dihydroxybenzoic acid and 2-hydroxy-5-methoxybenzoic acid) and α-cyano-4-hydroxycinnamic acid (CHCA) being the most commonly used for the analysis of N-glycans, and CHCA and 4-chloro-α-cyanocinnamic acid (ClCCA) for the analysis of glycopeptides [104].

For a regular MALDI-MS measurement, the analyte is at first co-crystallized with the respective matrix on the stainless-steel MALDI target plate. Subsequently, as indicated in *Figure 8*, dried analyte-matrix spots are fired with laser, whose energy, after being absorbed by the matrix, evokes

the release of molecules in a form of a hot plume. Although the exact mechanism of MALDI is still debated, the latter step is believed to generate ions of the analyte and the matrix, both of which are subsequently accelerated in an electric field [103]. In most cases, MALDI-MS is assembled with a time-of-flight (TOF) mass analyzer (MALDI-TOF-MS), which determines the *m/z* of the generated analyte ions based on the time they need to reach the detector. Since all ions are originally given the same kinetic energy and as MALDI typically produces singly charged ions (e.g., $[M+Na]^+$, $[M+H]^+$, $[M+K]^+$, $[M-H]^-$), the velocity of ions is directly proportional to their molecular mass [105]. As such, molecules with lower mass fly at higher velocities and reach the detector faster than larger and slower molecules.

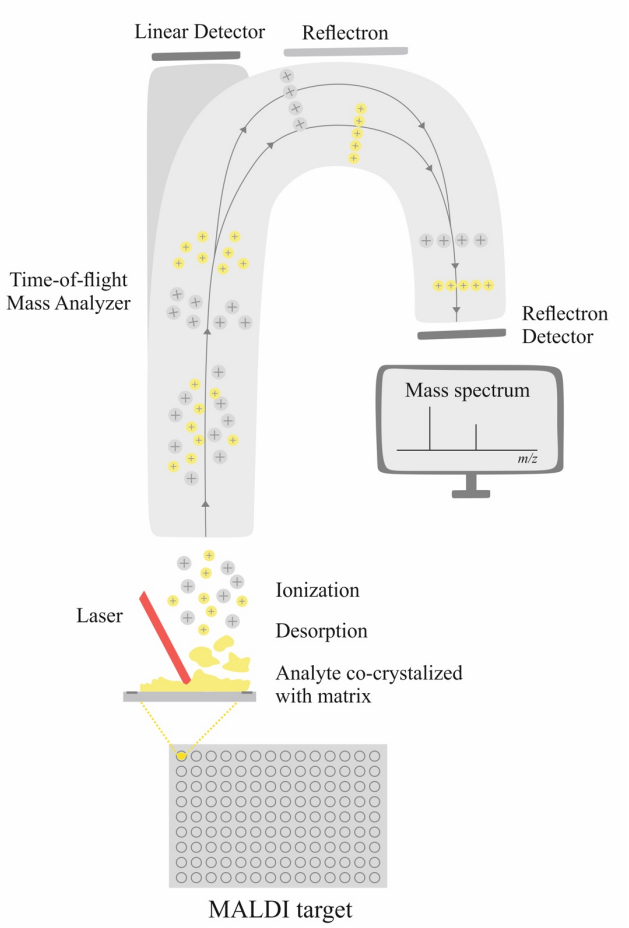

Figure 8. Schematic representation of the MALDI-TOF-MS measurement procedure.

Depending on the character of investigated molecules, MALDI-TOF-MS measurement can be performed in positive and negative ionization mode, with the latter being necessary for the analysis of underivatized sialylated *N*-glycans that carry a negative charge. MALDI is regarded as a "soft" ionization method, as it produces ions without fragmenting or decomposing the analyte molecules. Nevertheless, the labile nature of α-glycosidic bonds that link sialic acids to galactoses might lead to a partial loss of sialic acid residues during the MS measurement [106]. Additionally, in positive ionization mode, negatively charged sialylated glycans are prone to form multiple alkali metal adducts (Na, K), which hinders the relative quantification [106]. To minimize those disturbing effects, numerous chemical derivatization reactions for neutralization and stabilization of sialic acid residues have been proposed. These include permethylation that converts all carboxyl, hydroxyl, and amine groups within the glycan into methyl esters [107], as well as methylation [106] and methylamidation [108], which derivatize exclusively carboxyl groups. Particularly useful are linkage-specific derivatization methods, such as esterification [109, 110], amidation [111], and dimethylamidation [112], which allow discriminating between α2,6- and α2,3-linked sialic acid.

Due to differences in their orientation and reactivity, carboxyl groups of α2,6-linked sialic acids become esterified, amidated, or dimethylamidated (depending on the used protocol), whereas carboxyl groups of α2,3-linked linked sialic acids form lactones with C2 hydroxyl groups of adjacent galactoses. This selective reactivity leads to the *m/z* difference between these two sialic acid isomers, allowing discrimination of their linkage. Recently, a modified version of dimethylamidation reaction has been reported by Holst et al. [113], in which relatively unstable lactones of α2,3-linked sialic acids are stabilized via their pH-driven hydrolysis and amidation that occurs in the presence of ammonium hydroxide.

3.2.2. MALDI-MS Imaging

The sensitivity and specificity of MALDI-MS have been exploited in a new technology, MALDI-MS Imaging (MALDI-MSI), which allows mapping the distribution of analytes directly within the tissue. Although initially it was targeted for the analysis of peptides and proteins, MALDI-MSI is more and more commonly used in other types of "omics" including glycomics. Importantly, as this technique can be adapted for various biological materials, including formalin-fixed paraffin-embedded (FFPE) tissues, it allows retrieving molecular data from large cohorts of archived samples.

In principle, *in situ N*-glycosylation analysis by MALDI-MSI resembles the regular in-solution procedure, as it likewise involves incubation of the investigated sample with the *N*-glycan-releasing PNGase F enzyme and the subsequent co-crystallization of the analyte with the MALDI matrix. However, in the case of MALDI-MSI, the investigated material consists of very thin (~ 5 μm) tissue sections mounted on conductive indium tin oxide (ITO)-coated glass slides. To prevent delocalization of released *N*-glycans and hence to retain site-specificity, both the enzyme and the matrix solutions are deposited in a very controlled and homogeneous manner, using specialized robotic spraying devices. Among the most commonly used ones are HTX TM-Sprayer (HTX Technologies LLC) and SunCollect System (Bruker Daltonics) that allow controlling various parameters, including velocity and temperature of the sprayed solution. Notably, when using FFPE-preserved material, enzymatic digestion and the following matrix application are preceded by deparaffinization, rehydration, and (in some cases) antigen retrieval steps. Similarly, all chemical derivatizations, which in standard procedure typically occur after *N*-glycan release, must be conducted prior to PNGase F digestion. Otherwise, these treatments could cause *N*-glycan delocalization and loss of site-specific information. Finally, after MALDI matrix deposition, the processed tissues are measured. For this purpose, indicated tissue regions (or the entire tissue area) are irradiated by a laser at a spatial resolution ranging between 20-100 μm, generating mass spectra for each XY coordinate. This results in a two-dimensional visualization of the spatial distribution of released *N*-glycans within the tissue.

Chapter II Scientific goal

Over the last decades, cancer-related glycosylation alterations have gained increased attention as they were shown to have the potential to serve as complementary markers aiding diagnosis, monitoring, and treatment of disease. Among others, glycosylation alterations have been reported in ovarian cancer, which, despite intense research efforts, invariably remains the most lethal gynecological malignancy in women. While changes of total serum *N*-glycome in ovarian cancer patients have already been broadly examined, data available on glycosylation alterations in individual serum-derived glycoproteins and ovarian cancer tissue is still limited. Therefore, the aim of this work was to investigate epithelial ovarian cancer (EOC)-related glycosylation alterations at the level of immunoglobulin G (IgG), the most abundant serum glycoprotein, and at the level of EOC tissue. As such, this work aimed at determining EOC-related glycosylation alterations from two different perspectives; while IgG-specific glycosylation alterations reflected the biological response of the host to the tumor, the *in situ* analysis allowed revealing alterations occurring directly on glycoproteins expressed in cancer cells and their surroundings.

As opposed to previous studies, in which analysis of IgG glycosylation alterations relied on enzymatically released *N*-glycans, in this work, EOC-related IgG glycosylation alterations were examined at the level of tryptic glycopeptides, in order to provide more detailed protein- and site-specific information. This analytical approach was crucial for two main reasons. Firstly, in humans, IgG occurs as four subclasses that, despite high amino acid sequence homology, differ in respect to structural and functional characteristics, e.g., antigen-binding, immune complex formation, and triggering of effector functions. Secondly, besides conserved Fc-*N*-glycosylation sites, some IgG molecules possess additional *N*-glycosylation sites within variable domains of their Fab-regions. Due to distinct localization and accessibility, Fc- and Fab-*N*-glycans influence different IgG functions and properties and were shown to differ structurally. Nevertheless, since a majority of available data originates from studies of total IgG protein, information regarding IgG subclass- and site-specific glycosylation in EOC is very limited. Therefore, in this work, the analytical workflow was adapted to allow the profiling of IgG_1-, IgG_2-, and IgG_3-specific Fc-*N*-glycosylation changes in EOC patients. The analysis of IgG_4 was omitted primarily due to its very low concentration in serum. Additionally, it was tested whether EOC-related IgG subclass-specific glycosylation alterations are dependent on patients' age and disease stage, and, ultimately, whether observed differences have the potential to aid EOC diagnosis.

The aim of the second part of this work was to investigate *in situ N*-glycosylation in EOC tissue, implementing cutting-edge technology, MALDI mass spectrometry imaging (MALDI-MSI), which enables the visualization of the spatial distribution of numerous analytes in a single imaging experiment. More precisely, it was intended to examine the spatial distribution of *in situ* released *N*-glycans in formalin-fixed paraffin-embedded EOC tissue specimens and furthermore to determine whether the distribution of particular types of *N*-glycans reflects tissue morphology. Since EOC

is a highly heterogeneous disease, besides the most common and aggressive high-grade serous ovarian cancer, the analysis included less aggressive EOC histotypes, such as low-grade serous, clear cell, and endometrioid carcinoma as well as non-malignant borderline ovarian tumor. In particular, it was aimed to examine EOC tissue-specific sialylation, as this glycosylation feature that is known to play an important role in tumor progression, angiogenesis, and metastasis has not been studied *in situ* in its stabilized form in EOC tissue so far. To allow discrimination between α2,6- and α2,3-sialylated *N*-glycans, the analytical workflow has been adapted, introducing a linkage-specific sialic acid derivatization reaction. Finally, it was aimed to determine whether tissue-contained *N*-glycans have the potential to serve as discriminants of cancerous and non-cancerous regions of ovarian tissue.

Chapter III Subclass-specific IgG glycosylation in epithelial ovarian cancer

The content of this chapter has been adapted from the following research article:

Wieczorek M, Braicu EI, Oliveira-Ferrer L, Sehouli J, Blanchard V (2020)
Immunoglobulin G Subclass-Specific Glycosylation Changes in Primary Epithelial Ovarian Cancer. *Front. Immunol.* 11:654.

The original version can be found under: https://doi.org/10.3389/fimmu.2020.00654

1. Introduction

1.1. Immunoglobulin G

Immunoglobulin G (IgG), present at a concentration of 7-18 mg/ml, is the most abundant glycoprotein and, at the same time, the most abundant antibody class in human serum. As all antibodies, IgG is a soluble form of B-cell surface receptors that are formed and released by mature plasma cells in response to encountered antigens and upon activation by helper T cells. IgG plays an important role in multiple humoral immune processes, among others, antigen neutralization, target opsonization, antibody-dependent cell-mediated cytotoxicity (ADCC), activation of the complement system and complement-dependent cytotoxicity (CDC), providing comprehensive systemic immune protection. In humans, IgG is divided into four subclasses – IgG_1, IgG_2, IgG_3, and IgG_4 – named according to their decreasing abundance in blood [114].

Table 1. Comparison of IgG subclasses (modified from Vidarsson et al.[115]).

		IgG_1	IgG_2	IgG_3	IgG_4
General information:	Relative abundance in serum (%)	60-65	20-25	5-10	3-6
	Molecular mass (kDa)	146	146	170	146
	Amino acids in hinge region (n)	15	12	62*	12
	Inter-heavy chain disulfide bonds (n)	2	4	11*	2
	Half-life (days)	21	21	7/~21*	21
	Placental transfer	++++	++	++/++++*	+++
Response to:	Proteins	++	+/-	++	++
	Polysaccharides	+	+++	+/-	+/-
	Allergens	+	-	-	++
Binding to Fc receptors:	FcγRI	+++	-	++++	++
	FcγRIIa	+++	+/++	++++	++
	FcγRIIb/c	+	-	++	+
	FcγRIIIa	++/+++	+/-	++++	++/-
	FcγRIIIb	+++	-	++++	-
	FcγRn	+++	+++	++/+++	+++
Complement activation:	C1q binding	++	+	+++	-

* varies between different IgG_3 allotypes

Despite the fact that amino acid sequences of all IgG subclasses are 90% identical, each subclass differs with respect to structure, antigen-binding, immune complex formation, triggering of effector functions, placental transport, and half-life [115]. For instance, IgG_1, IgG_3, and (to a lesser extent) IgG_4 are primarily formed against protein antigens, whereas IgG_2 against repetitive polysaccharide structures that are found on encapsulated bacteria [116]. IgG_3 is the strongest inducer of effector functions, which is owed to its superior affinity toward activating Fc gamma receptors (FcγRs)

and C1q complement factor, and is produced first in the course of various infections including herpes and HIV [117, 118]. Contrarily, IgG_2 and IgG_4 are weak inducers of both FcγRs- and complement-mediated effector functions [119]. Comparison of all four IgG subclasses is shown in *Table 1*.

1.1.1. IgG structure

IgG is a relatively big (~150 kDa) glycoprotein composed of two identical γ-heavy chains and two identical κ- or λ-light chains, which are linked together via inter-chain disulfide bonds forming a characteristic Y-shaped structure. As depicted in *Figure 9*, each γ-heavy chain (H) consists of three constant domains (C_H1, C_H2, C_H3) and one variable domain (V_H) at its N-terminal end. In turn, each light chain (L) is composed of one constant (C_L) and one variable domain (V_L). Functionally, each IgG molecule can be divided into three distinctive regions, i.e. fragment antigen binding (Fab), fragment crystallizable (Fc), and a hinge region.

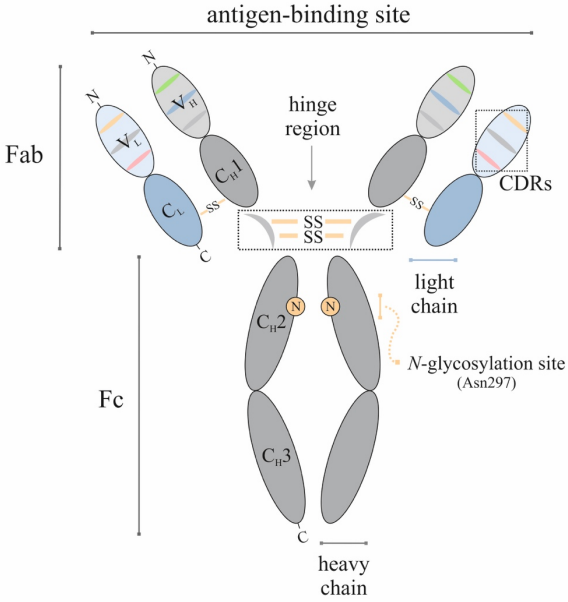

Figure 9. IgG structure. Structural elements are designated as: V_L and V_H, variable domains of light (blue) and heavy (grey) chains; C_L and C_H, constant domains of light and heavy chains; SS, disulfide bridge; CDRs, complementarity determining regions.

The complete IgG molecule contains two Fab regions that constitute both arms of its Y-shaped structure. Both Fab arms are composed of one variable (V_H, V_L) and one constant domain (C_H1, C_L) of each of the light and the heavy chain and are responsible for recognizing and binding to antigens. Each Fab variable domain contains three hypervariable regions, referred to as complementarity determining regions (CDRs) that are evenly interspersed with four framework regions of low variability. While the latter regions are mainly responsible for providing structural stability, CDRs are directly engaged in binding antigen and as such determine IgG antigen specificity. It should be noted, that due to their high hypervariability, CDRs enable antibodies to recognize virtually unlimited number of antigens.

The central part of the IgG molecule, located between C_H1 and C_H2 domains, is referred to as a hinge region. Due to its localization, hinge region provides a linker between both Fab arms and the Fc domain and determines segmental flexibility of the molecule. Additionally, depending on the IgG subclass, it contains from 2 to 11 disulfide bonds that link both heavy chains together (*Table 1*). The length and flexibility of the hinge region vary greatly between different IgG subclasses, being of middle length and high flexibility in IgG_1, short and rigid in IgG_2, very long and highly flexible in IgG_3, and short but of intermediate flexibility in IgG_4. Both the length and the flexibility of the hinge

region determine the relative orientation and movements of Fab and Fc domains, which in turn influences IgG capacity to bind antigens and form immune complexes.

Located below the hinge region, C_H2 and C_H3 domains of both heavy chains form the IgG Fc region, which is responsible for antibody effector functions and pharmacokinetic properties. It contains binding sites for C1q protein that is involved in the complement system, activating and inhibitory FcγRs expressed on the surface of cells of the innate immune system, and the neonatal Fc receptor (FcRn), which is important for antibody half-life and placental transport. Despite being composed of only constant domains, the IgG Fc tail exhibits a substantial degree of heterogeneity. The latter arises from differences within primary amino acid sequences among all IgG subclasses and allotypes and from the varying composition of Fc-attached *N*-glycans.

1.1.2. IgG glycosylation

The Fc region of all four IgG subclasses contains a highly conserved *N*-glycosylation site at asparagine 297 (Asn279), localized within the C_H2 domain of each heavy chain. The attached *N*-glycans protrude toward the inner hydrophobic cleft between the two opposing C_H2 domains. Due to their localization, *N*-glycans maintain the Fc-tail in a specific horseshoe-shaped conformation, in which C_H3 domains are closely associated and C_H2 domains are spatially separated (*Figure 10*). As described in the following sections, the latter conformation is essential for IgG Fc-mediated effector functions, elicited via interactions with FcγRs and complement.

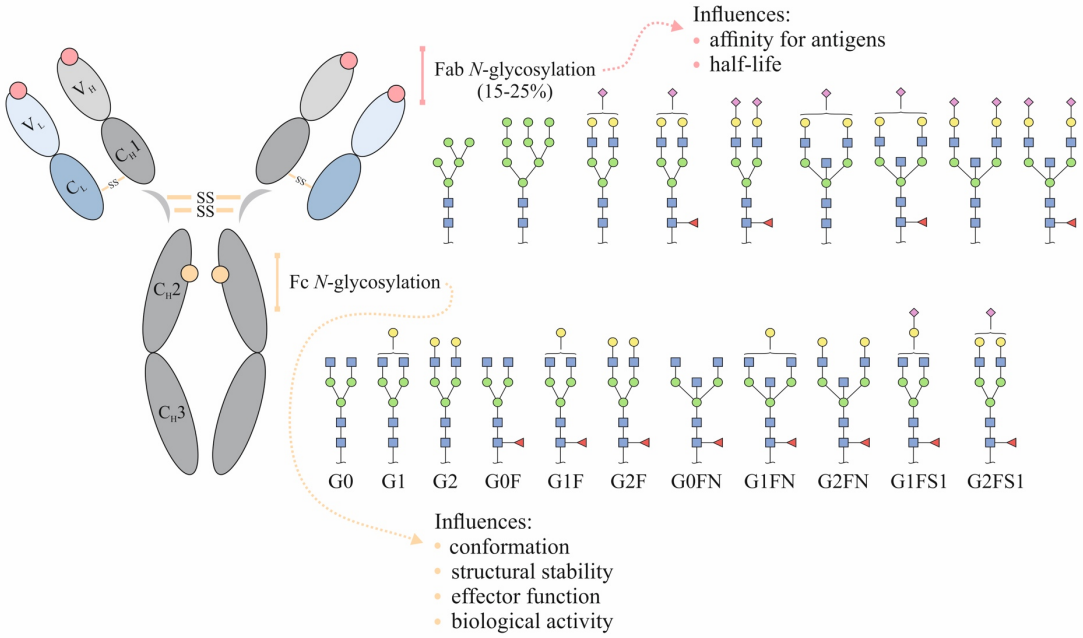

Figure 10. IgG Fc- and Fab-associated N-glycans. Carbohydrate structures are given in terms of: G, galactose; F, fucose; N, bisecting GlcNAc; S, sialic acid.

In humans, Fc-linked *N*-glycans are predominantly of biantennary complex-type and usually carry a fucose residue attached to the core (*Figure 10*). They vary strongly in respect to the number of attached galactoses, giving rise to a combination of structures decorated with zero, one, or two

galactoses. They are abbreviated G0, G1, and G2 when carrying both antennary GlcNAc but no fucose and G0F, G1F, and G2F when decorated with both antennary GlcNAc and an α1,6-linked core-fucose. A small portion of IgG Fc *N*-glycans is terminated with one or two sialic acids (S) attached mainly via α2,6-linkage to the underlying galactose and/ or carry a bisecting GlcNAc (N). Both high mannose- and hybrid-type *N*-glycans are rarely observed at Asn297. Even when present, they represent only a trace amount of all IgG Fc-attached *N*-glycans.

Notably, 15 to 25% of all circulating IgG molecules contain additional *N*-glycosylation sites within their variable domains. In contrast to the highly conserved Fc *N*-glycosylation site, these Fab-resident *N*-glycosylation sites are more variable as they emerge from gene segment rearrangements and somatic mutations during the immunoglobulin synthesis. They may occur within both heavy and light chains, in CDRs as well as in framework regions. IgG Fab *N*-glycans are mostly of complex biantennary type and, unlike Fc-attached *N*-glycans, contain low levels of core-fucose and high levels of bisecting GlcNAc, galactose, and sialic acid. High occurrence of these fully processed biantennary *N*-glycan structures was suggested to result from higher exposure of Fab-attached *N*-glycans to the surrounding solvent, which makes them more accessible for respective glycosyltransferases. Representatives of IgG Fc- and Fab-associated *N*-glycans are depicted in *Figure 10*.

1.1.3. IgG Fc-mediated effector functions

The biological activity of IgG is exerted via interactions of the IgG Fc domain with specialized Fc-effector molecules that include FcγRs, expressed on the surface of innate immune cells, and soluble initiators of the complement cascade.

1.1.3.1. Fc-gamma receptors

A wide range of IgG-mediated responses is elicited via interactions with their cognate FcγRs ubiquitously expressed on innate immune cells. In humans, there are three types of FcγRs, namely high-affinity FcγRI and low-affinity FcγRII and FcγRIII. The latter two are further divided into three (FcγRIIa, FcγRIIb, FcγRIIc) and two (FcγRIIIa, FcγRIIIb) variants, respectively. All FcγRs belong to the family of non-catalytic tyrosine-phosphorylated receptors and share a conserved signalling pathway that involves phosphorylation of the cytoplasmic domains by extrinsic tyrosine kinases [120]. FcγRI, FcγRIIa, FcγRIIc, FcγRIIIa, and FcγRIIIb utilize an immunoreceptor tyrosine-based activating motif (ITAM) and hence are qualified as activating FcγRs. Their cross-linking by IgG-opsonized targets evokes an effector cell type-specific response such as degranulation, phagocytosis, ADCC, transcription of cytokine genes, and/or release of inflammatory mediators, all of which aim to destroy the invading pathogen [121, 122]. Contrarily, FcγRIIb transmits its signal via an immunoreceptor tyrosine-based inhibitory motif (ITIM) and represents the sole inhibitory Fcγ receptor [121]. Its primary job is to antagonize the signalling activity of ITAM-containing FcγRs and to regulate inflammatory responses under homeostatic conditions. Consistently, a deficiency of

FcγRIIb is associated with autoimmunity [123]. Curiously, binding affinity of FcγRs was shown to be influenced by the nature of IgG Fc-linked *N*-glycans [124], which will be addressed in the following sections of this work. Additionally, it has long been recognized that FcγRs display some degree of selectivity toward different IgG subclasses. As shown in *Table 1*, a majority of FcγRs bind primarily IgG_1 and IgG_3, which corresponds to their overall strong effector function profiles. On the other hand, IgG_2 exhibits the weakest affinity for most FcγRs and does not bind to FcγRI, FcγRIIb, and FcγRIIIb receptors [125].

A key FcγR-mediated IgG effector function is ADCC, whereby an antibody-coated target cell is killed by host effector cells. Precisely, after binding to the target cell-specific antigen, the IgG Fc part is recognized and bound by FcγRs on effector immune cells that include natural killer (NK) cells, monocytes, macrophages, eosinophils, neutrophils, and dendritic cells. For ADCC to occur, the above antibody-receptor interaction must involve an activating FcγR and be potent enough to cause its cross-linking. Activation of specific signalling pathways in effector immune cells leads to the release of cytolytic proteins, such as pore-forming perforins and serine proteases granzymes [126]. These apoptosis-inducing proteins evoke cellular membrane disruption and DNA fragmentation, eventually leading to target cell death [127].

1.1.3.2. Complement system

Besides FcγRs, IgG immune complexes can activate the complement system, a powerful tool of the innate immune system that flags and eradicates pathogens, tumor, apoptotic cells, and cell debris. Complement consists of many distinct plasma proteins circulating in blood in a form of inactive precursors that become activated at sites of infection. Typically, the complement system activation results in the lysis of the target cell, which is commonly referred to as complement-dependent cytotoxicity (CDC). In principle, triggering of complement cascade leads to the formation of C3b peptide, the main effector molecule of the complement system. C3b molecules act as opsonins; they are deposited on the pathogen surface targeting it for destruction by phagocytes. As the complement cascade progresses, the proteolytic activation of the following complement components results in the formation of membrane attack complexes that pierce the pathogen's membrane bilayer leading to its destruction. Importantly, IgG can activate the complement via all three pathways, namely the classical, the lectin, and the alternative pathway [128].

In the classical pathway, the Fc-C_H2 domain of an antigen-complexed IgG is recognized and bound by a complement component 1q (C1q), a big protein of a bouquet-like shape, composed of six globular heads linked together via collagen-like tails [129, 130]. Interestingly, IgG subclasses differ in their potencies to activate the complement system via C1q binding [131]. As C1q is a spacious protein, this variance is believed to partly result from different flexibility of their hinge regions. Indeed, IgG_1 and IgG_3, whose hinge regions are highly flexible, are the strongest activators of the classical complement pathway. The IgG_2 of moderately flexible hinge-region is a weaker C1q

activator, whereas the least flexible IgG_4 shows no or minor reactivity toward C1q [131]. Notably, binding to C1q is strongly dependent on the nature of Asn297-attached *N*-glycans, which is described in the following section.

In the lectin pathway, C1q is replaced by a mannan-binding lectin (MBL), which binds to terminal mannoses and other glycan residues, i.e., fucose, glucose, and GlcNAc, exposed on pathogens or pathogen-bound antibodies. The alternative pathway plays an important role in the amplification of the pathogen-bound C3b compound that was generated by the classical and the lectin pathway. It has been shown that activation of the alternative pathway might be induced by IgG-immune complexes and that IgG Fc *N*-glycans play an important role in this process [132].

1.1.4. Impact of Fc glycosylation on IgG effector functions and biological activity

Covalently-linked *N*-glycans constitute an integral part of the IgG molecule and influence its important features, including conformation, stability, half-life, and effector functions [133]. The X-ray crystallographic analysis revealed that Asn297-attached glycans participate in approximately 70 non-covalent interactions with the Fc backbone, which are necessary for stabilizing the IgG quaternary structure [134]. In fact, progressive shortening of Fc-attached *N*-glycans was shown to result in an approaching of the two opposing C_H2 domains [135], whereas their complete removal via enzymatic or chemical methods deprived IgG of its pro- and anti-inflammatory activity [136].

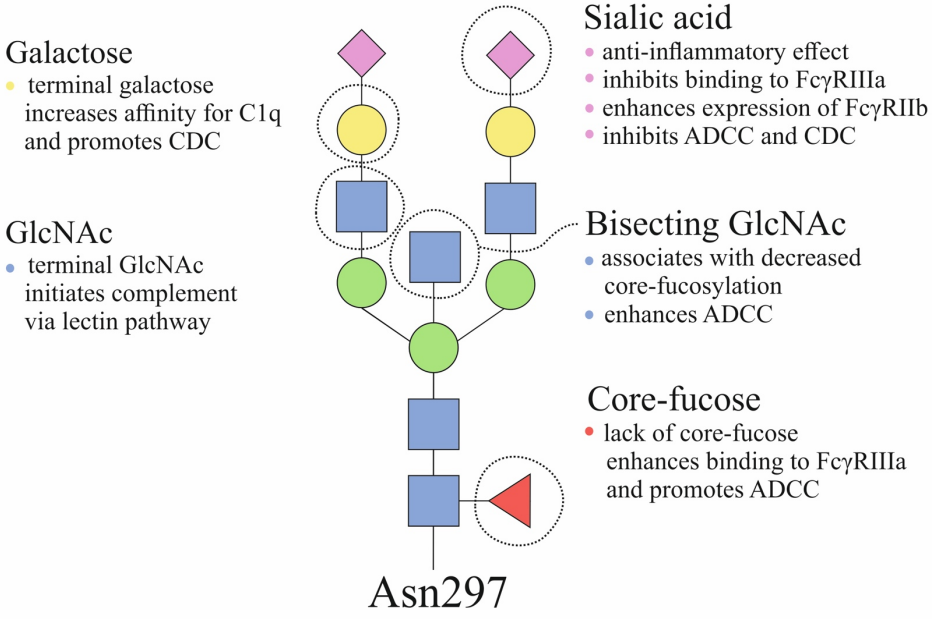

Figure 11. Impact of Fc-attached N-glycans on IgG effector functions.

It has been well documented that the absence of core-fucose on IgG Fc *N*-glycans enhances IgG affinity for FcγRIIIa/b and, in this manner, increases its ADCC efficacy [137, 138]. The latter effect is due to the glycan-glycan interaction that occurs between a fucosylated IgG Fc *N*-glycan and an Asn162-linked glycan on the FcγRIII receptor, which sterically hinders the Fc-FcγRIII binding [139].

This finding has been exploited to generate potent therapeutic antibodies for targeted anti-cancer treatment. For instance, mogamulizumab and obinutuzumab that are used for T-cell- and follicular lymphoma, respectively, were glycoengineered to contain low levels of core-fucose and, as a result, have enhanced ADCC activity [140]. Indirectly, a similar effect might be evoked by the presence of bisecting GlcNAc, since its addition prevents the attachment of core-fucose [141, 142]. The impact of Fc-attached *N*-glycans on IgG effector functions is summarized in *Figure 11*.

Besides the activation of FcγRIIIa/b by afucosylated IgG molecules, pro-inflammatory activity of IgG can also be exerted via a complement-dependent mechanism. Precisely, it has been demonstrated that the presence of terminal galactoses significantly increases IgG affinity for C1q, which leads to enhanced CDC [143]. Similarly, the presence of high-mannose and/or GlcNAc-terminated complex-type Fc *N*-glycans was shown to activate complement through the lectin pathway, by binding to MBL protein [144].

On the other hand, anti-inflammatory activity of IgG was shown to be attributed to the presence of terminal α2,6-linked sialic acid(s) [145]. For the first time, this correlation was reported for patients suffering from rheumatoid arthritis (RA), whose inflammatory condition was accompanied by decreased IgG sialylation and galactosylation [66]. Consistently, pregnancy-related RA remission was observed to coincide with an increase in IgG sialylation, whereas the postpartum relapse with its consecutive decrease [146]. In line with these findings, the anti-inflammatory property of intravenous immunoglobulin (IVIG; purified IgG fraction isolated from pooled plasma of more than a thousand donors, used to treat inflammatory diseases), was abrogated following the complete removal of IgG *N*-glycans and/or the selective removal of sialic acids [145]. Moreover, sialylated IgG molecules that were enriched from IVIG through lectin affinity techniques showed 10-fold enhanced anti-inflammatory activity compared to total IVIG [145]. Importantly, this protective effect of α2,6-linked sialic acids was shown to result from reduced ADCC activity due to decreased binding to FcγRIIIa on NK cells [147]. It has been hypothesized that bulky and far-reaching sialic acids might restrain flexibility of the hinge region and limit accessibility of the C_H2 domain that contains the binding site for FcγRIIIa [147]. Additionally, in transgenic mice models, anti-inflammatory activity of sialylated IgG *N*-glycans was shown to result from binding of sialylated Fc domain to humanized DC-SIGN receptor on macrophages. It was proposed that the latter binding induces production of interleukin (IL)-33 and IL-4 cytokines, leading to an increased expression of inhibitory FcγRIIb on effector macrophages [148]. Nevertheless, this mechanism remains controversial, as Temming et al. [149] found no evidence that human IgG_1 binds DC-SIGN, regardless of its sialylation status.

An anti-inflammatory effect of Fc sialylation can also be exerted via an FcγR-independent mechanism. Precisely, the terminal addition of sialic acid was shown to abrogate the binding of IgG_1 to C1q. The latter effect translates into a decreased level of C3b deposition on the target cell surface and ultimately reduced complement-mediated lysis [150]. Hence, by inhibiting ADCC and CDC,

the attachment of terminal α2,6-linked sialic acids serves as a molecular switch turning IgG from a pro- to an anti-inflammatory state.

1.1.5. IgG glycosylation in ovarian cancer

The first notion that aberrantly glycosylated IgG antibodies are present in the bloodstream of OC patients was reported almost 20 years ago [151]. In a meantime, Saldova et al. [152] demonstrated in a small cohort study that IgG isolated from OC patients' serum contains a lower proportion of monogalactosylated, digalactosylated, and sialylated *N*-glycan structures and a higher proportion of agalactosylated *N*-glycans. Since this discovery, the results of Saldova et al. have been confirmed in a number of studies, not only showing that OC is associated with altered IgG glycosylation but also that this altered profile correlates with disease severity and progression [153, 154]. Additionally, Qian et al. [154] demonstrated that the ratio of agalactosylated to galactosylated IgG structures is superior to CA 125 in discriminating between OC and benign gynecological conditions. Based on their results, the authors suggested that the latter ratio has the potential to serve as an adjunct diagnostic marker, which, in combination with CA 125, could reduce the number of false-positive outcomes [154]. More recently, Ruhaak et al. [155] quantified glycosylation profiles of the three major immunoglobulins, namely IgG, IgA, and IgM, isolated from serum of epithelial ovarian cancer (EOC) patients. Their results showed that IgG-specific glycosylation alterations are the most powerful in discriminating EOC and healthy individuals [155].

Despite the abundance of published data, there is no information available about IgG subclass-specific glycosylation changes in EOC, the most common and lethal type of ovarian cancer. Primarily, this is related to the fact that, in previous studies, IgG glycosylation was investigated at the level of enzymatically released *N*-glycans, without prior separation of IgG subclasses. As far as this approach is straightforward and time-efficient, information generated in this way is neither subclass- nor site-specific. Indeed, as described in the previous section, besides Fc-attached *N*-glycans, some IgG molecules contain additional *N*-glycans within their Fab arms that differ functionally and structurally. Although Ruhaak et al. [155] investigated IgG glycosylation at the level of tryptic glycopeptides, their study aimed at finding novel immunoglobulin glycosylation-based EOC markers rather than elucidating IgG subclass-specific EOC-related glycosylation profiles. As IgG subclasses were shown to differ in respect to various important characteristics, including antigen-binding, half-life, and triggering of effector function, IgG subclass-specific glycosylation analysis might provide an insight into biological mechanisms underlying the development and progression of ovarian cancer.

2. Materials and equipment

2.1. Materials

Chemicals and consumables:

- 4-Chloro-α-cyanocinnamic acid (ClCCA; Sigma Aldrich, Germany)
- Aluminium sulfate ($Al_2(SO_4)_3$; Sigma-Aldrich, Germany)
- Anti-human IgG_3 antibody (Abcam, Cambridge, England)
- Ammonium bicarbonate (ABC; Merck, Germany)
- Coomassie Brilliant Blue R-250 (CBB; ICN Biomedicals, USA)
- Cotton pads (Dirk Rossmann, Germany)
- Filter tips 10E 10 µl (Greiner Bio-One, Germany)
- Monopotassium phosphate (Merck, Germany)
- Monosodium phosphate (Merck, Germany)
- Peptide Calibration Standard II (Bruker Daltonics, Germany)
- Polyvinylidene fluoride membrane (GE Healthcare, The Netherlands)
- Potassium chloride (Carl Roth, Germany)
- Protein A Sepharose CL 4B (GE Healthcare, The Netherlands)
- Protein G Sepharose (GE Healthcare, The Netherlands)
- Serum tubes with clot activator (BD Vacutainer, USA)
- Sodium dodecyl sulphate (SDS; Serva Electrophoresis, Germany)
- Sodium chloride (NaCl; Carl Roth, Germany)

Enzymes:

- Trypsin Sequencing Grade (Promega, USA)

Solvents:

- Acetonitrile (ACN; VWR Chemicals, Germany)
- Ethanol (EtOH; Merck, Germany)
- Formic acid (FA; Honeywell Fluka, Germany)
- Milli-Q grade water
- Phosphoric (V) acid (H_3PO_4; Merck, Germany)
- Trifluoroacetic acid (TFA; Merck, Germany)

2.2. Equipment

- Analytical scale (Sartorius, Germany)
- Cold trap Unicryo MC2 x 21-60°C (Uniequip, Germany)
- Incubator 1000 (Dionex, Germany)

- MALDI-TOF/TOF mass spectrometer Ultraflex III (Bruker, Germany)
- Thermomixer (Eppendorf, Germany)
- Ultrasonic bath Sonorex TK52 (Bandelin, Germany)
- Vacuum pump (Vacuubrand, Germany)
- Water purification system MilliQ Plus (Millipore, Germany)

3. Methods

3.1. Sample collection

Eighty-seven primary EOC patients and 74 sex- and age-matched healthy controls were enrolled in this study, as indicated in *Table 2*. Written informed consent was obtained from all study participants and ethical approval was obtained from the Charité Institutional Ethics Committee (EA4/073/06) and the Ethics Committee of the Medical Association of Hamburg (#OB/V/03). Blood withdrawal was performed using clot activator serum tubes. After collection, blood was allowed to clot for 30 min to 2 h at room temperature. Afterward, serum was separated by centrifugation at 1200×g for 15 min. Aliquoted serum samples were stored at -80 °C until the time of further analysis.

Table 2. Demographics of the cohorts used in this study.

	Healthy	EOC
No of patients	74	87
Age [Mean ± SD]	59.8 ± 11.2	59.5 ± 10.3
CA 125 [Mean ± SD]	37.2 ± 106.8	929.4 ± 1482.0

Age is shown in years and CA 125 is shown as kU/L.

3.2. IgG purification

IgG was isolated from 5 µl of human serum by sequential two-step affinity purification using first Protein A Sepharose and then Protein G Sepharose, as depicted in *Figure 12*. Briefly, 30 µl of Protein A Sepharose slurry was transferred to a 1.5-ml tube containing 400 µl of phosphate-buffered saline (1×PBS). After the beads settled, the supernatant was discarded and replaced with 400 µl of 1×PBS, which step was repeated one more time. Following washing, the volume was brought up to 400 µl with 1×PBS and 5 µl of blood serum was added. The sample mixture was incubated under agitation at 650 rpm for 1 h at room temperature. Afterward, the entire mixture was applied into the shortened 200-µl filter tip. The flow-through I was collected, and Protein A Sepharose beads were washed with 5×200 µl of 1×PBS and 3×200 µl of MilliQ water. Captured IgG_1, IgG_2, and IgG_4 were eluted with 3×100 µl of 100 mM formic acid (FA) and evaporated in a vacuum centrifuge. Protein A Sepharose beads were regenerated by washing with 2×100 µl of 100 mM FA, 2×200 µl of MilliQ water, and 2×200 µl of 1×PBS. The Protein A flow-through I, collected in the previous step, was re-applied on the regenerated Protein A Sepharose column, and the secondary flow-through II was collected. Protein G Sepharose (30 µl of slurry) was conditioned as described above for Protein A Sepharose and re-suspended in the Protein A flow-through II. The following incubation, washing, and elution steps were performed the same way as described above for Protein A Sepharose. Collected eluates were dried in a vacuum centrifuge and stored at -20 °C until further analysis.

3.3. SDS-PAGE and Western blot

To assess potential cross-contamination, Protein A-bound IgG_1, IgG_2, IgG_4 fraction and Protein G-bound IgG_3 fraction were analyzed by sodium dodecyl sulfate-polyacrylamide gel electrophoresis (SDS-PAGE) followed by Coomassie Brilliant Blue staining and Western Blot using polyvinylidene fluoride membrane, using standard techniques. Sensitive Coomassie staining solution was prepared in-house using 0.02% CBB, 2% H_3PO_4, 5% $Al_2(SO_4)_3$, and 10% EtOH in MilliQ water. SDS-PAGE was performed using 10% acrylamide gel under reducing conditions. The presence of IgG_3 in Protein A and Protein G Sepharose-bound fractions was assessed by Western Blot using recombinant anti-human IgG_3 antibody (1:1000).

3.4. Tryptic digestion

Dried IgGs were dissolved in 50 µl of 50 mM ammonium bicarbonate (ABC) and were shaken for 5 min. Lyophilized sequencing grade modified trypsin (20 µg) was dissolved in 100 µl of ice-cold resuspension buffer provided by the manufacturer to obtain a final concentration of 0.2 µg/µl. Five microliters of the solution, corresponding to 1 µg of trypsin, was added to each IgG sample, followed by overnight incubation at 37 °C. The following day, digested IgGs were dried out in a vacuum centrifuge and stored at -20 °C until cotton-HILIC purification.

3.5. Cotton-HILIC purification

IgG glycopeptides were enriched using self-made micro-spin cotton-HILIC columns as described elsewhere [156], with minor modifications. Briefly, 10-µl filter tips were filled with fibers of cotton wool pads and conditioned by washing with 3×50 µl of MilliQ water and 3×50 µl of 80% acetonitrile (ACN). Afterward, dried IgG samples were resuspended in 50 µl of 80% ACN and loaded on the self-made cotton-HILIC microcolumns. Following the application of samples, columns were washed with 3×50 µl of 80% ACN containing 0.1% trifluoroacetic acid (TFA) and 3×50 of µl 80% ACN. The retained IgG glycopeptides were eluted with 6×50 µl of MilliQ water, dried out in a vacuum centrifuge, and stored at -20 °C until MALDI-TOF-MS measurement.

3.6. MALDI-TOF-MS measurement

Dried IgG glycopeptide samples were dissolved in MilliQ water and 1 µl was spotted on the stainless steel MALDI target plate. Once dried, the sample was overlaid with 1 µl of 2.5 mg/ml 4-chloro-α-cyanocinnamic acid (ClCCA) in 70% ACN and allowed to air-dry at room temperature. All measurements were performed on an Ultraflex III mass spectrometer equipped with Smartbeam laser (laser frequency 100 Hz). Prior to the measurement, the mass spectrometer was calibrated with Peptide Calibration Standard II. Mass spectra were recorded in reflectron negative ionization mode within the *m/z* window of 1000-5000. For each mass spectrum, 5000 laser shots were accumulated

using partial 'random-walk' laser movement mode. Exemplary spectra of Protein A-bound IgG_1, IgG_2, and IgG_4 fraction as well as Protein G-bound IgG_3 fraction are shown in *Figure 15*.

3.7. Data processing

Raw mass spectra were exported as ASCII text files, and the subsequent processing, which included re-calibration, baseline subtraction, and peak extraction, was performed with the MassyTools software [157]. Re-calibration was performed using the list of six IgG_1 glycopeptides (G0F, G1F, G0FN, G2F, G1FN, G2FS1) for mass spectra of Protein A Sepharose-bound IgG or the list of six IgG_3 glycopeptides (G0F, G1F, G0FN, G2F, G1FN, G2FS1) for mass spectra of Protein G Sepharose-bound IgG. The absolute intensities of the detected glycopeptides were normalized to the total area of IgG_1, IgG_2, and IgG_3. Then, by summing up relative intensities of respective glycopeptide structures, six (or five in the case of IgG_2) derived glycosylation traits, namely agalactosylation, monogalactosylation, digalactosylation, sialylation, bisection/bisecting GlcNAc, and fucosylation, were calculated separately for each IgG subclass according to the formulas:

Agalactosylation (Agal) = G0F + G0FN + G0 + G0N + mono G0F;
Monogalactosylation (Monogal) = G1F + G1FN + G1FS1 + G1 + G1N + G1S1 + mono G1F;
Digalactosylation (Digal) = G2F + G2FN + G2FS1 + G2 + G2N + G2S1;
Sialylation (Sial) = G1FS1 + G2FS1 + G1S1 + G2S1;
Bisection/ Bisecting GlcNAc (Bisec) = G0FN + G1FN + G2FN + G0N + G1N + G2N;
Fucosylation (Fuc) = G0F + G1F + G2F + G0FN + G1FN + G2FN + G1FS1 + G2FS1 + mono G0F + mono G1F.

Fucosylation of IgG_2 was not evaluated in this study as most of its afucosylated glycopeptides could not be determined due to the *m/z* overlap with fucosylated glycopeptides of IgG_4. Schematic representation of all detected structures can be found in *Table 4*.

3.8. Repeatability testing

To determine inter-day repeatability of an applied workflow, the entire analytical procedure including two-step IgG purification, tryptic digestion, cotton-HILIC enrichment, and MALDI-TOF-MS measurement was repeated using the same serum sample on three consecutive days. Mean, standard deviation (SD), and coefficient of variation (CV) values were calculated for the six most abundant glycopeptide structures of IgG_1, IgG_2, and IgG_3. Results of repeatability testing are presented in *Figure 16* and *Table 5*.

3.9. Statistical analysis

Statistical analysis was performed with SPSS version 25.0 (SPSS Inc, Chicago, USA). Means and SD values of IgG_1, IgG_2, and IgG_3 glycosylation traits in healthy controls and EOC patients were

calculated and are shown in *Table 6* and, in a form of bar graphs, in *Figure 18*. In order to assess associations between IgG glycosylation traits and EOC and to test whether detected EOC-related differences were statistically significant, a regression model was generated for each glycosylation trait. To minimize the effect of age on IgG glycosylation [158, 159], all regression models were corrected by including age as a covariate, which resulted in the following formulas: 'glycosylation trait Y ~ β_1*patient's status [0 = healthy control, 1 = EOC patient] + β_2*age + error'. Descriptive statistics of all regression models, i.e., regression beta coefficients (β), 95% confidence intervals (95% CI), and *p*-values, are listed in *Table 7*. In the following parts of this work, β_1 and p_1 values correspond to EOC-related association, whereas β_2 and p_2 values refer to age-related association. After Bonferroni correction for glycosylation traits, *p*-values smaller than 0.008 (for IgG_1 and IgG_3; 0.05/6 glycosylation traits) and smaller than 0.01 (for IgG_2; 0.05/5 glycosylation traits) were considered statistically significant. For each IgG subclass, the relation between agalactosylation and CA 125 diagnostic marker (log-transformed values) was assessed by fitting a linear model according to the formula 'IgG agalactosylation ~ β*CA 125 + error'. Linear graphs with coefficient of determination (R^2), β coefficients, and *p*-values are presented in *Figure 19*. For each regression model, the distribution of residuals was inspected and found to be normal.

In order to determine whether EOC-related IgG glycosylation alterations are as well detectable in younger patients suffering from an early-stage EOC, additional statistical analyses were performed stratifying both investigated cohorts into two age categories (younger: ≤ 55 years of age; older: ≥ 56 years of age) and the EOC cohort into two stage groups (early-stage: FIGO stage I and II; late-stage: FIGO stage III and IV). Demographics of the cohorts stratified by age and disease stage are shown in *Table 8*. Statistical significance of EOC-related alterations in both age groups (*Figure 20*) was determined using the Jonckheere-Terpstra test, as the independent variables consisted of three independent ordinal groups (healthy control < early-stage EOC < late-stage EOC) and the dependent variables were measured on a continuous scale. The null hypothesis was rejected when the Bonferroni corrected *p*-values were smaller than 0.05.

The ability of IgG subclass-specific glycosylation alterations to discriminate between healthy controls and EOC patients was determined using the Receiver Operating Characteristic (ROC) curve analysis as in Qian [154]. To allow for comparison with literature data, IgG glycosylation was represented in a form of a G0F/(G1F+G2F×2) ratio, calculated separately for each IgG subclass. Eventually, as shown in *Figure 21*, each graph included seven ROC curves; three curves of IgG subclass-specific glycosylation ratios, one curve of CA 125 biomarker alone, and three curves of combinations of CA 125 with respective IgG subclass-specific glycosylation ratio, obtained via binary logistic regression modelling.

4. Results

4.1. IgG purification

In this study, glycosylation profiles of the three most abundant IgG subclasses, namely, IgG_1, IgG_2, and IgG_3, isolated from sera of 87 EOC patients and 74 age-matched healthy controls, were analyzed by means of MALDI-TOF-MS. In order to obtain subclass-specific information, glycosylation analyses were performed at the level of tryptic glycopeptides. To this end, IgG was isolated from blood serum samples using a two-step affinity purification employing at first Protein A Sepharose that binds IgG_1, IgG_2, and IgG_4, and then Protein G Sepharose to capture the remaining IgG_3 contained in the Protein A Sepharose flow-through. Schematic representation of the applied IgG isolation procedure is presented in *Figure 12*.

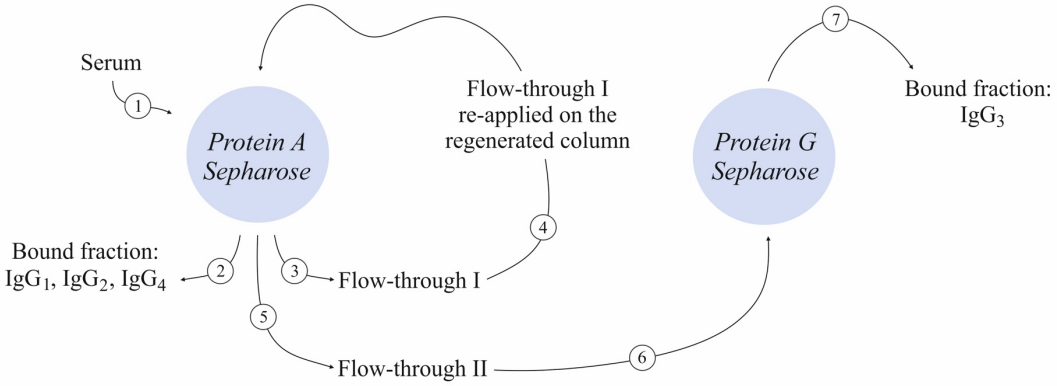

Figure 12. Two-step affinity purification of IgG.

Since the amino acid sequence of IgG_2 and IgG_3 glycopeptides is quite often identical [160, 161], the complete depletion of IgG_2 in the first purification step was essential for the subsequent analysis of IgG_3-specific glycosylation. As indicated in *Figure 12*, in order to remove all residual IgG_1, IgG_2, IgG_4 from the Protein A flow-through I fraction, the latter fraction was repeatedly loaded on the regenerated Protein A column. This procedure allowed for the complete binding of IgG_1, IgG_2 and IgG_4, which was confirmed by SDS-PAGE and Western Blot analyses. As can be seen in *Figure 13A*, the Protein G Sepharose-bound fraction was free of IgG_1, IgG_2, and IgG_4 subclasses and contained only the IgG_3 subclass. This can be deduced from the localization of IgG heavy chain bands on the Coomassie-stained SPS-PAGE gel.

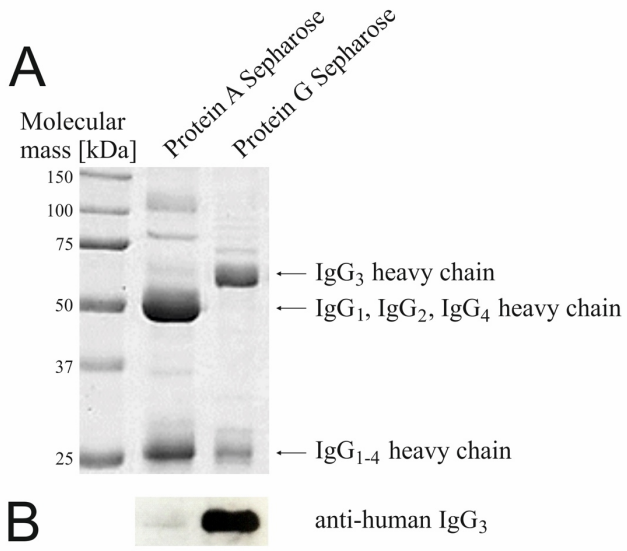

Figure 13. (A) SDS-PAGE and (B) Western Blot analysis of Protein A- and Protein G Sepharose-bound fractions.

Specifically, the heavy chain of IgG_3 has a higher molecular mass compared to IgG_1, IgG_2, and IgG_4 and hence migrates slower through the gel. The presence of IgG_3 in Protein A and Protein G Sepharose-bound fractions was determined with the help of recombinant anti-human IgG_3 antibody. As visible in *Figure 13B*, the Protein A Sepharose-bound fraction contains only a trace amount of IgG_3. Therefore, this cross-contamination was deemed negligible.

4.2. Tryptic digestion and cotton-HILIC enrichment

In this study, as IgG glycosylation was investigated at the level of glycopeptides, the isolated IgG fractions were subjected to tryptic digestion. By cleaving specifically at the carboxyl side of lysine and arginine, trypsin generates IgG *N*-glycopeptides of following sequences: EEQYNSTYR in IgG_1, EEQFNSTFR in IgG_2/IgG_3, and EEQFNSTYR in IgG_4, in which asparagine (N) is occupied by covalently linked *N*-glycans. Amino acid sequences of subclass-specific tryptic *N*-glycopeptides together with their molecular masses (without attached *N*-glycan) are shown in *Table 3*.

Table 3. Tryptic N-glycopeptides of human IgG subclasses.

IgG subclass	Fc *N*-glycopeptide sequence	Molecular mass [Da]
IgG_1	EEQYNSTYR	1188.51
IgG_2	EEQFNSTFR	1156.51
IgG_3	EEQFNSTFR	1156.51
IgG_4	EEQFNSTYR	1172.51

Amino acid sequences are given in terms of: E, glutamic acid; Q, glutamine; Y, tyrosine; F, phenylalanine; N, asparagine; S, serine; T, threonine; R, arginine.

Enrichment of glycopeptides prior to MS analysis is a crucial step since glycopeptides constitute only a small part of the entire tryptic digestion mixture and their ionization is suppressed by accompanying non-glycosylated peptides. In order to improve the detection of IgG glycopeptides, the enzymatic digestion was followed by hydrophilic interaction liquid chromatography solid-phase extraction (HILIC-SPE) using self-made cotton-HILIC columns as described elsewhere [156]. As visible in *Figure 14*, the cotton-HILIC enrichment step allowed the removal of a considerable number of IgG peptides, which significantly enhanced the detection of IgG Fc *N*-glycopeptides.

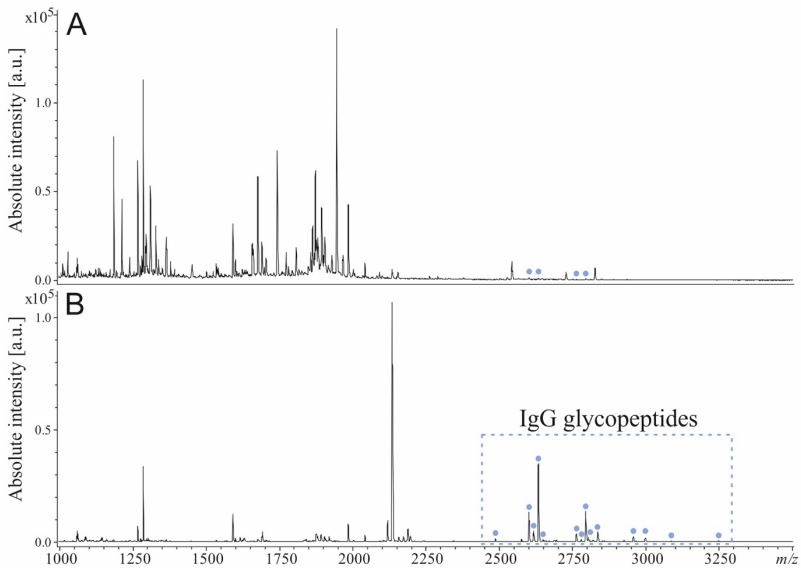

Figure 14. MALDI-TOF mass spectra $[M-H]^-$ of IgG glycopeptide fraction (A) prior to and (B) after cotton-HILIC enrichment. IgG glycopeptides are indicated with blue dots.

4.3. Detection of IgG Fc glycopeptides in MALDI-TOF-MS

The MALDI-TOF-MS measurements were performed in negative-ionization mode to enable the simultaneous detection of neutral and underivatized negatively charged (sialylated) IgG glycopeptides. Of all detected peaks, 17 corresponded to IgG_1 glycopeptides, 11 to IgG_2 glycopeptides, and 16 to IgG_3 glycopeptides. It should be noted that IgG_4 glycopeptides were not investigated in this study, due to their very low abundancy and the *m/z* overlap with afucosylated structures of the more abundant IgG_2 subclass [161]. In the case of IgG_1 and IgG_3, glycopeptides carrying both afucosylated and core-fucosylated *N*-glycans were analyzed. Contrarily, due to the above-mentioned *m/z* overlap with fucosylated IgG_4 structures [161], a majority of IgG_2 glycopeptides carrying afucosylated *N*-glycans could not be determined and therefore was excluded from the statistical analysis. Nevertheless, as core-fucosylated structures constitute on average 97% of all IgG_2 glycoforms [162], exclusion of afucosylated glycopeptides has a minor impact on the entire analysis. Almost all detected IgG glycopeptides carried biantennary complex-type *N*-glycans, bearing from zero to two galactoses. A minority of IgG glycopeptides was decorated by bisecting GlcNAc and/or terminal sialic acid. The exemplary MALDI-TOF mass spectra of Protein A- and Protein G-bound fractions, containing IgG_1, IgG_2, IgG_4, and IgG_3, respectively, are presented in *Figure 15*. All detected structures included in the IgG glycopeptide analysis are listed in *Table 4*.

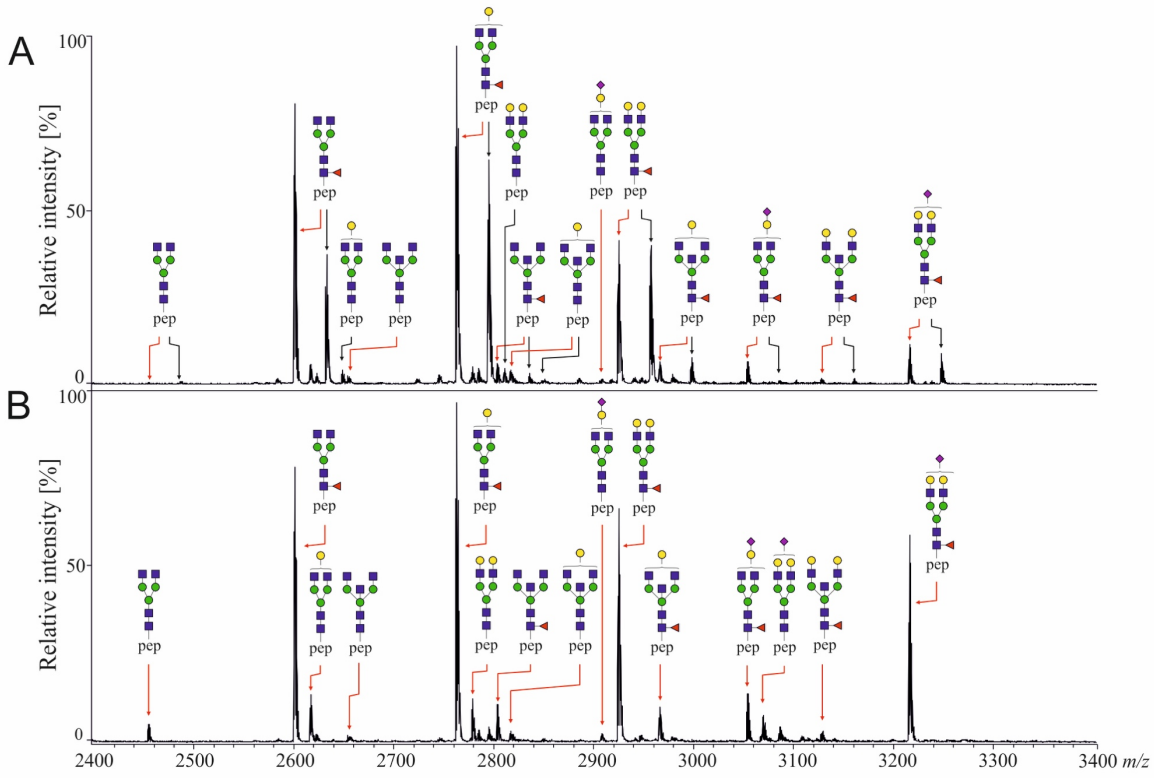

Figure 15. MALDI-TOF mass spectra [M-H]⁻ of (A) Protein A and (B) Protein G Sepharose-bound fractions. Black arrows indicate structures of IgG_1, whereas red arrows indicate those of IgG_2 (in A) and IgG_3 (in B).

Table 4. IgG N-glycopeptide structures investigated in this study.

Structural composition		*m/z* [M-H]$^-$ of detected glycoforms [Da]		
		IgG_1 (EEQYNSTYR)	IgG_2 (EEQFNSTFR)	IgG_3 (EEQFNSTFR)
G0F	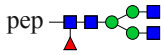	2632.04	2600.04	2600.04
G1F	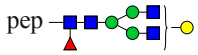	2794.09	2762.09	2762.09
G2F	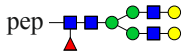	2956.14	2924.15	2924.15
G0FN	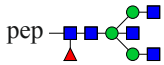	2835.12	2803.12	2803.12
G1FN	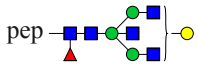	2997.17	2965.17	2965.17
G2FN	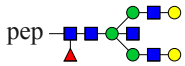	3159.22	3127.23	3127.23
G1FS1	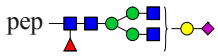	3085.18	3053.19	3053.19
G2FS1	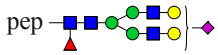	3247.24	3215.24	3215.24
Mono G0F	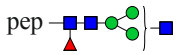	2428.96	-	-
Mono G1F	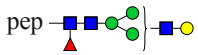	2591.01	-	-
G0	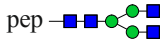	2485.98	2453.98	2453.98
G1	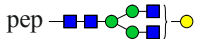	2648.03	-*	2616.04
G2	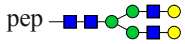	2810.08	-*	2778.09
G0N	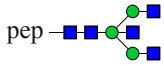	2689.06	2657.06	2657.06
G1N	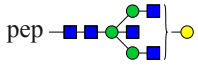	2851.11	-*	2819.12
G2N	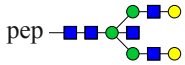	3013.16	-*	2981.17
G1S1	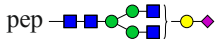	-	2907.13	2907.13
G2S1	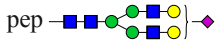	3101.18	-*	3069.18

Schematic representations are given in terms of: pink diamond, sialic acid; yellow circle, galactose; blue square, *N*-acetylglucosamine; green circle, mannose; red triangle, fucose; pep, peptide moiety. Structural composition is given in terms of: G, galactose; F, fucose; N, bisecting GlcNAc; S, sialic acid; Mono, monoantennary. * isomeric glycopeptide species of IgG_2 and IgG_4.

4.4. Repeatability testing

Inter-day repeatability of an applied workflow was determined by repeating the entire analytical procedure including two-step IgG purification, tryptic digestion, cotton-HILIC enrichment, and MALDI-TOF-MS measurement on three consecutive days, using the same healthy control serum sample. The results of repeatability testing are presented in *Figure 16*. For each investigated IgG subclass, mean, SD, and CV values were calculated for the six most abundant glycopeptide structures and are shown in *Table 5*. As can be seen in *Figure 16* and *Table 5*, the applied analytical workflow yielded highly repeatable results.

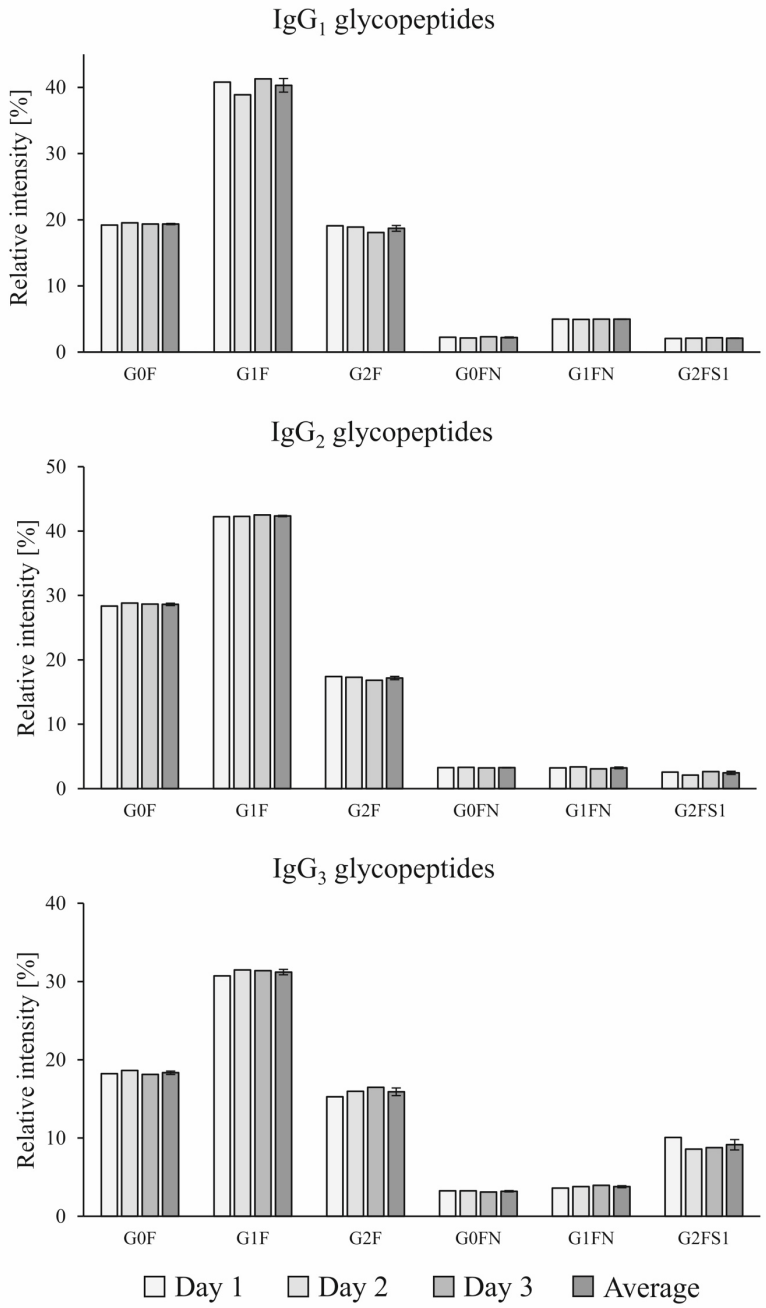

Figure 16. Inter-day repeatability testing of the IgG subclass-specific glycosylation analysis. Average is shown as mean ± SD.

Table 5. Mean, SD, CV, and mean CV values from inter-day repeatability testing of the IgG subclass-specific glycosylation analysis.

		G0F	G1F	G2F	G0FN	G1FN	G2FS1	Mean CV
IgG_1	Mean [%]	19.35	40.31	18.69	2.22	4.97	2.10	
	SD [%]	0.15	1.03	0.44	0.08	0.02	0.04	
	CV [%]	0.75	2.55	2.34	3.43	0.37	1.80	1.87
IgG_2	Mean [%]	28.61	42.34	17.18	3.26	3.22	2.45	
	SD [%]	0.19	0.11	0.26	0.04	0.14	0.25	
	CV [%]	0.65	0.25	1.50	1.13	4.20	10.10	2.97
IgG_3	Mean [%]	18.33	31.20	15.91	3.20	3.78	9.14	
	SD [%]	0.21	0.35	0.49	0.08	0.13	0.66	
	CV [%]	1.17	1.11	3.07	2.60	3.47	7.25	3.11

4.5. Age-related IgG glycosylation changes

As IgG glycosylation was shown to be age-dependent [158, 159], the profile of age-related IgG glycosylation changes was investigated in each IgG subclass. For this purpose, the relative abundance of the two most prominent glycopeptide structures, namely G0F and G2F, was examined in the entire healthy cohort and the healthy cohort divided into 5-year-broad age groups. As visible in *Figure 17A*, in all IgG subclasses, the abundance of G0F and G2F was observed to alter with increasing age. Consistent with previous studies [163, 164], the relative abundance of G0F was positively correlated with age, whereas G2F was negatively correlated, as it decreased with increasing age. Interestingly, for all IgG subclasses, the most noticeable age-related alteration was observed in subjects older than 55 (*Figure 17B*), which could potentially be related to hormonal

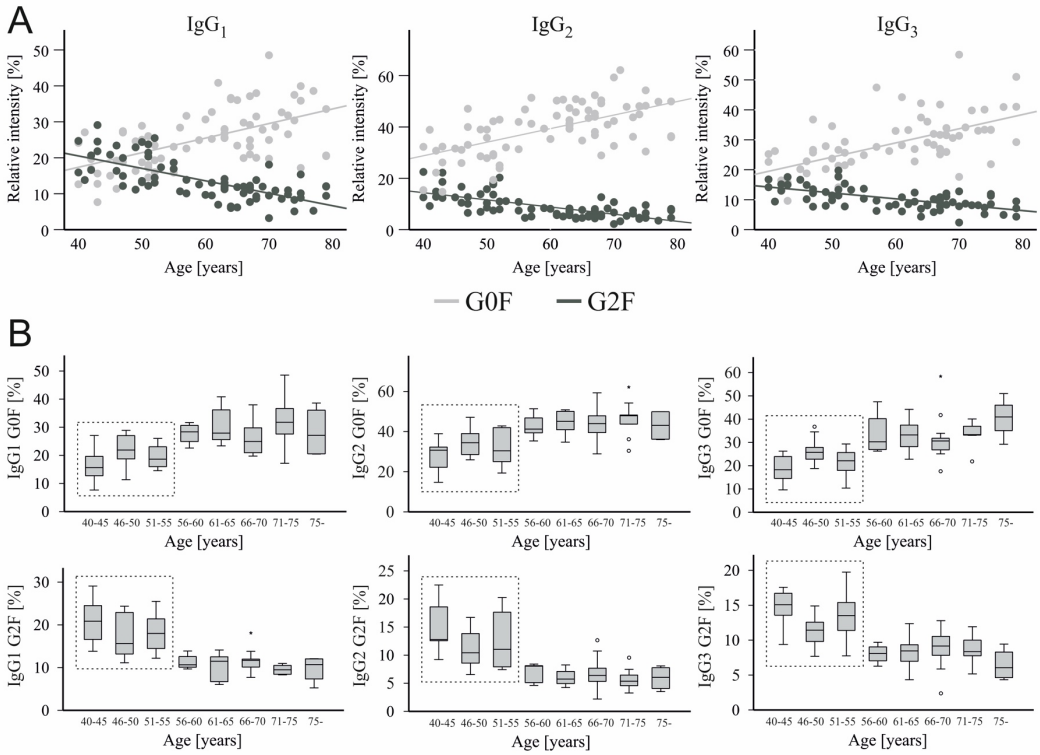

Figure 17. Age-related IgG glycosylation changes. Relative abundance of G0F and G2F in (A) the entire healthy cohort and (B) the healthy cohort divided into 5-year-broad age groups.

changes that accompany the occurrence of menopause. Importantly, the effect of age was also observed at the level of calculated glycosylation traits. As shown in *Table 7*, in all IgG subclasses, agalactosylation was positively correlated with age, whereas monogalactosylation, digalactosylation, and sialylation were negatively correlated, as judged by their respective β coefficient values. Interestingly, glycosylation of IgG_1 was the least affected by age, as only its three out of six glycosylation traits, i.e., agalactosylation, digalactosylation, and sialylation, showed a statistically significant association. On the contrary, in IgG_3, a significant association with age was observed for nearly all glycosylation traits, with fucosylation being the only trait whose *p*-value ($p_2 = 0.009$) was higher than the Bonferroni-corrected threshold of $\alpha = 0.008$ (0.05/6 glycosylation traits).

4.6. Subclass-specific IgG glycosylation in EOC

As IgG glycosylation was observed to be age-dependent, statistical significance of EOC-related changes in IgG subclass-specific glycosylation was determined with the help of regression models, in which age was considered as a covariate. Mean relative abundances of IgG glycosylation traits in EOC patients and healthy controls together with SD values are shown in *Table 6*. The results of the regression analysis are presented in *Table 7* and, in a form of bar graphs, in *Figure 18*.

Table 6. Mean relative abundances and SD values of IgG glycosylation traits in investigated cohorts.

Glycosylation trait	IgG subclass	Healthy [Mean ± SD]	EOC [Mean ± SD]
Agal	IgG_1	31.6 ± 9.6	42.7 ± 13.5
	IgG_2	46.8 ± 11.1	52.3 ± 12.7
	IgG_3	36.4 ± 11.0	44.4 ± 15.1
Monogal	IgG_1	49.4 ± 4.2	43.8 ± 7.7
	IgG_2	41.8 ± 5.9	38.3 ± 8.1
	IgG_3	40.4 ± 4.3	37.1 ± 6.9
Digal	IgG_1	19.0 ± 7.1	13.5 ± 6.4
	IgG_2	11.9 ± 5.9	9.5 ± 5.0
	IgG_3	23.2 ± 9.2	18.4 ± 9.2
Sial	IgG_1	3.2 ± 1.2	2.7 ± 1.3
	IgG_2	5.1 ± 1.7	5.1 ± 2.3
	IgG_3	14.8 ± 6.4	12.9 ± 6.3
Bisec	IgG_1	15.5 ± 4.5	14.6 ± 3.9
	IgG_2	11.1 ± 3.5	10.3 ± 2.9
	IgG_3	12.3 ± 3.2	11.6 ± 2.9
Fuc	IgG_1	94.5 ± 2.2	95.5 ± 1.8
	IgG_2	-	-
	IgG_3	91.4 ± 4.6	91.7 ± 4.8

Representations of glycosylation traits are given in terms of: Agal, agalactosylation; Monogal, monogalactosylation; Digal, digalactosylation; Sial, sialylation; Bisec, bisecting GlcNAc; Fuc, core-fucosylation.

Table 7. Associations between IgG glycosylation traits, EOC, and age.

		IgG_1			IgG_2			IgG_3		
		β	95% CI	*p*	β	95% CI	*p*	β	95% CI	*p*
Agal	(1) EOC	11.285	7.83, 14.738	**1.3E-9**	6.056	2.737, 9.374	**4.2E-4**	9.120	5.242, 12.998	**7.6E-6**
	(2) Age	0.418	0.256, 0.580	**9.9E-7**	0.524	0.369, 0.680	**4.4E-10**	0.609	0.428, 0.789	**5.7E-10**
Monogal	(1) EOC	-5.690	-7.630, -3.750	**3.6E-8**	-3.591	-5.666, -1.516	**8.0E-4**	-3.516	-5.369, -1.663	**2.6E-4**
	(2) Age	-0.118	-0.209, -0.027	0.011	-0.260	-0.357, -0.163	**4.2E-7**	-0.162	-0.249, -0.076	**3.0E-4**
Digal	(1) EOC	-5.596	-7.466, -3.726	**2.0E-8**	-2.465	-3.927, -1.003	**1.1E-3**	-5.604	-8.216, -2.992	**4.0E-5**
	(2) Age	-0.299	-0.387, -0.212	**2.8E-10**	-0.264	-0.333, -0.196	**2.3E-12**	-0.446	-0.568, -0.325	**2.5E-11**
Sial	(1) EOC	-0.576	-0.949, -0.202	**0.003**	-0.052	-0.644, 0.539	0.861	-2.360	-4.229, -0.492	0.014
	(2) Age	-0.039	-0.057, -0.022	**1.9E-5**	-0.072	-0.100, -0.044	**8.3E-7**	-0.275	-0.362, -0.188	**4.6E-9**
Bisec	(1) EOC	-0.852	-2.141, 0.437	0.193	-0.774	-1.764, 0.215	0.124	-0.564	-1.517, 0.388	0.244
	(2) Age	0.052	-0.008, 0.112	0.091	0.038	-0.009, 0.084	0.110	0.084	0.040, 0.128	**2.7E-4**
Fuc	(1) EOC	1.025	0.403, 1.648	**0.001**	-	-	-	0.459	-1.081, 1.998	0.557
	(2) Age	0.005	-0.024, 0.034	0.721	-	-	-	0.096	0.024, 0.168	0.009

For each glycosylation trait, regression beta coefficient (β) values are reported together with their 95% confidence interval (95% CI) and respective *p*-values (*p*). Bonferroni corrected *p*-values smaller than or equal to 0.008 (for IgG_1 and IgG_3; 0.05/6 glycosylation traits) and 0.01 (for IgG_2; 0.05/5 glycosylation traits) were considered statistically significant and are highlighted in bold. Representations of glycosylation traits are given in terms of: Agal, agalactosylation; Monogal, monogalactosylation; Digal, digalactosylation; Sial, sialylation; Bisec, bisecting GlcNAc; Fuc, core-fucosylation.

IgG_1 profiling

The glycosylation profile of IgG_1 was found to be the most markedly altered in EOC patients. As shown in *Figure 18* and *Table 7*, IgG_1 exhibited the most pronounced increase in agalactosylation (β_1 = 11.285, p_1 = 1.3E−9) and the most pronounced decrease in mono- and digalactosylation in EOC patients (β_1 = −5.690, p_1 = 3.6E−8 and β_1 = −5.596, p_1 = 2.0E−8, respectively). Additionally, even though IgG_1 was found to contain low levels of sialylated glycopeptides (*Table 6*), it was the only subclass in which sialylation was significantly decreased (p_1 = 0.003) in EOC patients. On the other hand, IgG_1 was found to contain the highest proportion of glycopeptides carrying bisecting GlcNAc (*Table 6*); however, no significant differences were observed between both investigated cohorts. A vast majority (94–96%) of all detected IgG_1 glycopeptides carried core-fucosylated *N*-glycans. Remarkably, even though the difference in IgG_1 core-fucosylation between healthy controls and EOC patients was minor (94.5 ± 2.2 in healthy controls vs. 95.5 ± 1.8 in EOC patients), the EOC-related increase in fucosylation was found to be statistically significant (p_1 = 0.001).

IgG_2 profiling

Partially, EOC-related glycosylation alterations of IgG_2 resembled those observed in IgG_1; however, they were less pronounced (*Figure 18* and *Table 7*). Agalactosylation of IgG_2 was significantly increased (β_1 = 6.056, p_1 = 4.2E−4), whereas monogalactosylation and digalactosylation were significantly decreased in EOC patients (β_1 = −3.591, p_1 = 8.0E−4 and β_1 = −2.465, p_1 = 1.1E−3, respectively). Notably, IgG_2 was found to be characterized by particularly high agalactosylation that was observed in both investigated groups of individuals. For instance, while agalactosylation of IgG_1 represented 31.6% and 42.7% in healthy controls and EOC patients, respectively, in IgG_2, these were 46.8% and 52.3%, respectively. Therefore, on average, IgG_2 agalactosylation was about 12.4% higher in each investigated group. This was reflected by very low IgG_2 digalactosylation, as it constituted only 11.9% and 9.5% in healthy controls and EOC patients, respectively (*Table 6*). IgG_2 sialylation was slightly higher than in IgG_1; nevertheless, no significant differences were detected between healthy controls and EOC patients. The abundance of bisecting GlcNAc in IgG_2 was not found to differ between both investigated cohorts. As mentioned in previous sections, IgG_2 fucosylation was not evaluated due to the *m/z* overlap with fucosylated glycopeptides of IgG_4.

IgG_3 profiling

Analysis of IgG_3 glycosylation is hindered by its high genetic polymorphism [160, 161]. In the Caucasian population, tryptic digestion of IgG_3 usually generates the glycopeptide of a peptide sequence EEQFNSTFR, which is identical to that of IgG_2 [160]. Due to genetic polymorphism, in some individuals, phenylalanine is replaced by tyrosine at position 296. In this study, 16 serum samples (7 healthy controls and 9 EOC patients) were excluded from the statistical analysis of the IgG_3 glycosylation due to the presence of alternative peptide sequences and different *m/z* values of

the resulting glycopeptide moieties, leading to normalization issues. Nonetheless, the exclusion of these 16 samples did not lead to an age mismatch of investigated groups; the mean age ± SD values remained at 61.6 ± 11.2 years and 59.8 ± 10.3 years in the healthy and the EOC group, respectively, with the difference being statistically insignificant (data not shown). As visible in *Figure 18* and *Table 7*, IgG_3-specific EOC-related glycosylation changes resembled those observed in other subclasses; however, they were less pronounced than in IgG_1 and more pronounced than in IgG_2. Consistently, agalactosylation of IgG_3 increased in EOC patients ($\beta_1 = 9.120$, $p_1 = 7.6E{-}6$), whereas monogalactosylation and digalactosylation decreased ($\beta_1 = -3.516$, $p_1 = 2.6E{-}4$ and $\beta_1 = -5.604$, $p_1 = 4.0E{-}5$, respectively). Notably, IgG_3 was found to be characterized by visibly higher sialylation than this observed in IgG_1 and IgG_2. Nevertheless, even though its decrease in EOC patients was clearly visible, due to Bonferroni correction the difference between both groups ($p_1 = 0.014$) was deemed statistically insignificant. As can be seen in *Figure 18* and *Table 7*, neither bisecting GlcNAc nor fucosylation of IgG_3 were significantly different between healthy controls and EOC patients.

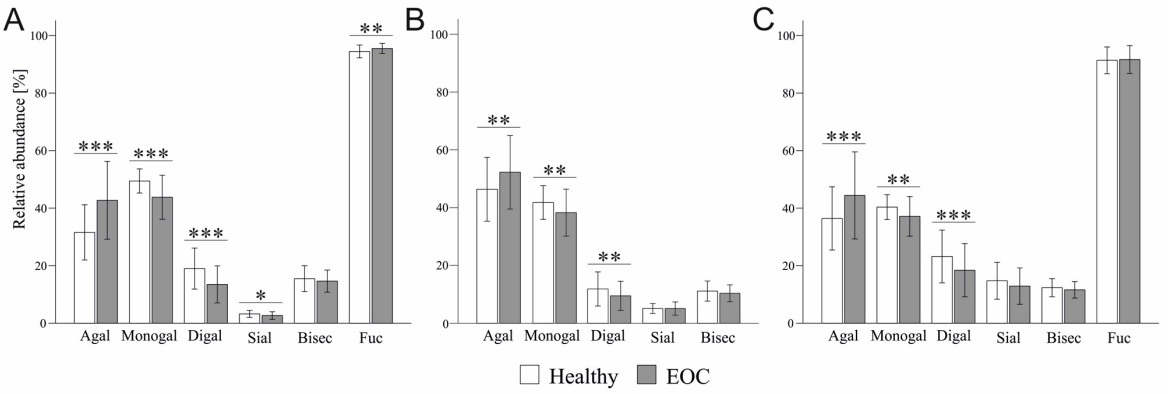

Figure 18. Comparison of (A) IgG_1-, (B) IgG_2-, and (C) IgG_3-specific glycosylation profiles between healthy controls and EOC patients. Relative abundance of given glycosylation traits was obtained by summing up relative intensities of the corresponding tryptic glycopeptides detected by MALDI-TOF-MS. Bars and error bars represent mean relative abundance and standard deviation, respectively. The p-values were obtained from regression analysis, adjusting for patients' status (0 = healthy control, 1 = EOC) and age. After Bonferroni correction for glycosylation traits, statistically significant differences are indicated as $*p \leq 0.008$, $**p \leq 0.001$, $***p \leq 0.0001$ in IgG_1 and IgG_3 and $*p \leq 0.01$, $**p \leq 0.002$, $***p \leq 0.0002$ in IgG_2.

Association of IgG agalactosylation with CA 125

Among all investigated glycosylation traits, IgG agalactosylation displayed the most prominent EOC-related alteration. For this reason, its association with CA 125, the most commonly used biomarker for OC, was assessed in the entire cohort using a linear regression model analysis. As can be seen in *Figure 19*, regardless of IgG subclass, agalactosylation showed a significant positive association with CA 125. As judged by R^2, β coefficient, and *p*-values, the strongest association was observed in IgG_1 ($\beta = 2.793$, $p = 1.7E{-}8$), whereas the weakest in IgG_2 ($\beta = 1.267$, $p = 0.009$). With an R^2 of 0.074, a β coefficient of 1.856, and a *p*-value of 9.6E−4, IgG_3 agalactosylation displayed a slightly stronger association with CA 125 than this observed in IgG_2 but weaker than this of IgG_1.

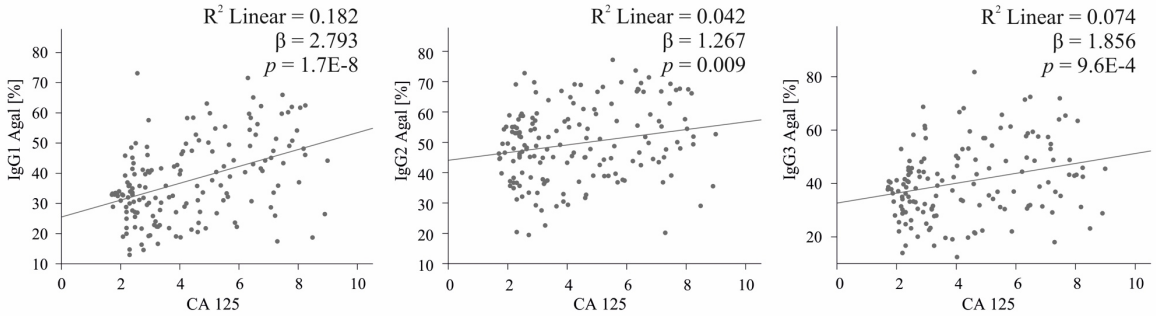

Figure 19. Association between IgG subclass-specific agalactosylation (Y-axis) and log (CA 125), the routine diagnostic marker (X-axis). Descriptive statistics are shown for the total cohort and are given in terms of: R^2 Linear, coefficient of determination; β, regression β coefficient; p, p-value. IgG_1 is shown on the left, IgG_2 in the middle, and IgG_3 on the right.

4.7. Potential of subclass-specific IgG glycosylation alterations to aid early EOC detection

In most cases, the diagnosis of OC occurs once the disease has already progressed to an advanced stage (FIGO stage III and IV) [165]. Additionally, ovarian cancers usually develop after menopause, with the majority of OC patients being 55 to 64 years old at the time of diagnosis [4]. In order to determine whether EOC-related IgG glycosylation alterations have the potential to aid early EOC detection, the subclass-specific glycosylation profiles have been re-investigated, stratifying both cohorts into the younger (≤ 55 years old) and the older (≥ 56 years old) groups (for the age cut-off value see section *4.5. Age-related IgG glycosylation changes*) and, additionally, stratifying the EOC cohort into the early- (FIGO stage I and stage II) and the late-stage (FIGO stage III and stage IV) group. Demographics of both cohorts stratified by age and EOC stage are presented in *Table 8*.

Table 8. Demographics of the cohorts stratified by age and EOC stage.

	≤ 55 years old			≥ 56 years old		
	Healthy	EOC Early	EOC Late	Healthy	EOC Early	EOC Late
No of patients	29	14	17	45	23	33
Age [Mean ± SD]	47.7 ± 4.4	48.6 ± 4.6	47.8 ± 4.4	67.5 ± 6	65.2 ± 6.7	66 ± 6
CA 125 [Mean ± SD]	22.1 ± 20.8	446.4 ± 779.2	1149.4 ± 1723.4	46.8 ± 134.2	587.6 ± 1057	1259.2 ±1686.3

Age is shown in years and CA 125 is shown as kU/L.

As visible in *Figure 20*, application of age-stratification revealed that, in each IgG subclass, differences between healthy controls and EOC patients are strongly apparent in the younger group and, with the exception of IgG_1, rarely detectable in the older group. In particular, IgG_2 glycosylation that in the non-stratified cohort analysis exhibited the least significant EOC-related differences (*Figure 18*) was found to displayed significant alterations already in the early stage of the disease, when only younger individuals were included in the analysis (*Figure 20C*). These trends suggest that age-related glycosylation changes might obscure EOC-specific alterations and, in this way, hinder

the detection of the disease particularly in older individuals. Importantly, the age- and the EOC stage-stratified analysis confirmed previous findings that the IgG_1 subclass displays the most pronounced EOC-related glycosylation alterations, irrespective of patients' age. Additionally, as visible in *Figure 20B,* applied stratification revealed that the EOC-related increase in IgG_1 fucosylation

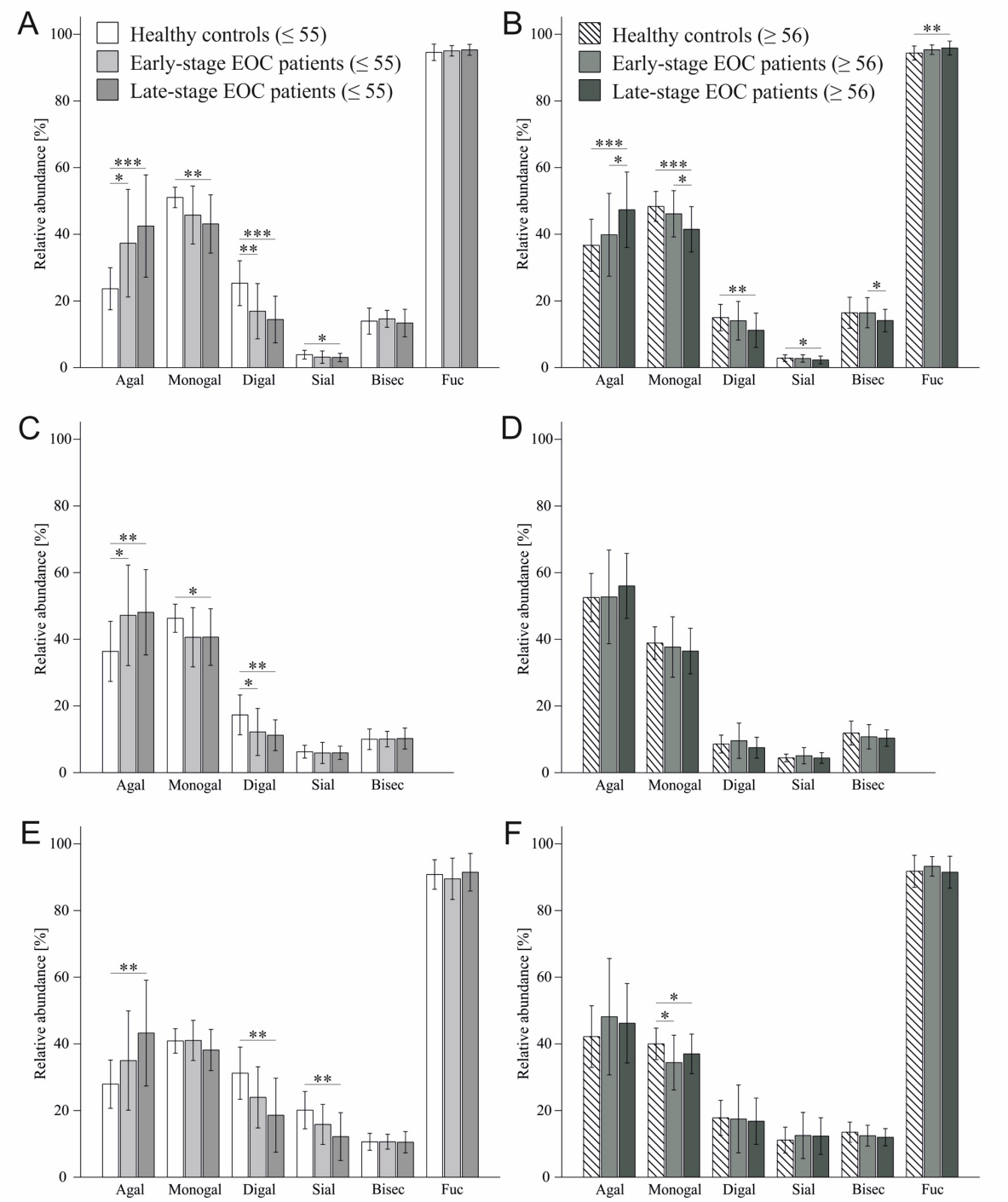

*Figure 20. Comparison of (A, B) IgG_1-, (C, D) IgG_2-, and (E, F) IgG_3-specific glycosylation profiles between healthy controls and EOC patients. Glycosylation trait profiles are shown separately for the cohort ≤ 55 years of age (A, C, E) and the cohort ≥ 56 years of age (B, D, F). Relative abundance of given glycosylation traits was obtained by summing up relative intensities of the corresponding tryptic glycopeptides detected by MALDI-TOF-MS. Bars represent mean relative intensity and error bars represent standard deviation. Statistical significance of observed differences was determined by Jonckheere-Terpstra-Test. The Bonferroni corrected p-values are indicated as * $p < 0.05$, ** $p < 0.01$, *** $p < 0.001$.*

is limited to advanced-stage EOC patients of the older group. When comparing stratified profiles of all three IgG subclasses, it can be noted that, in IgG_1 and IgG_3, EOC-related alterations seem to reflect disease activity, as differences observed in the late stage were more prominent than those observed in the early-stage EOC. Contrarily, the IgG_2-specific profile of early-stage EOC resembled

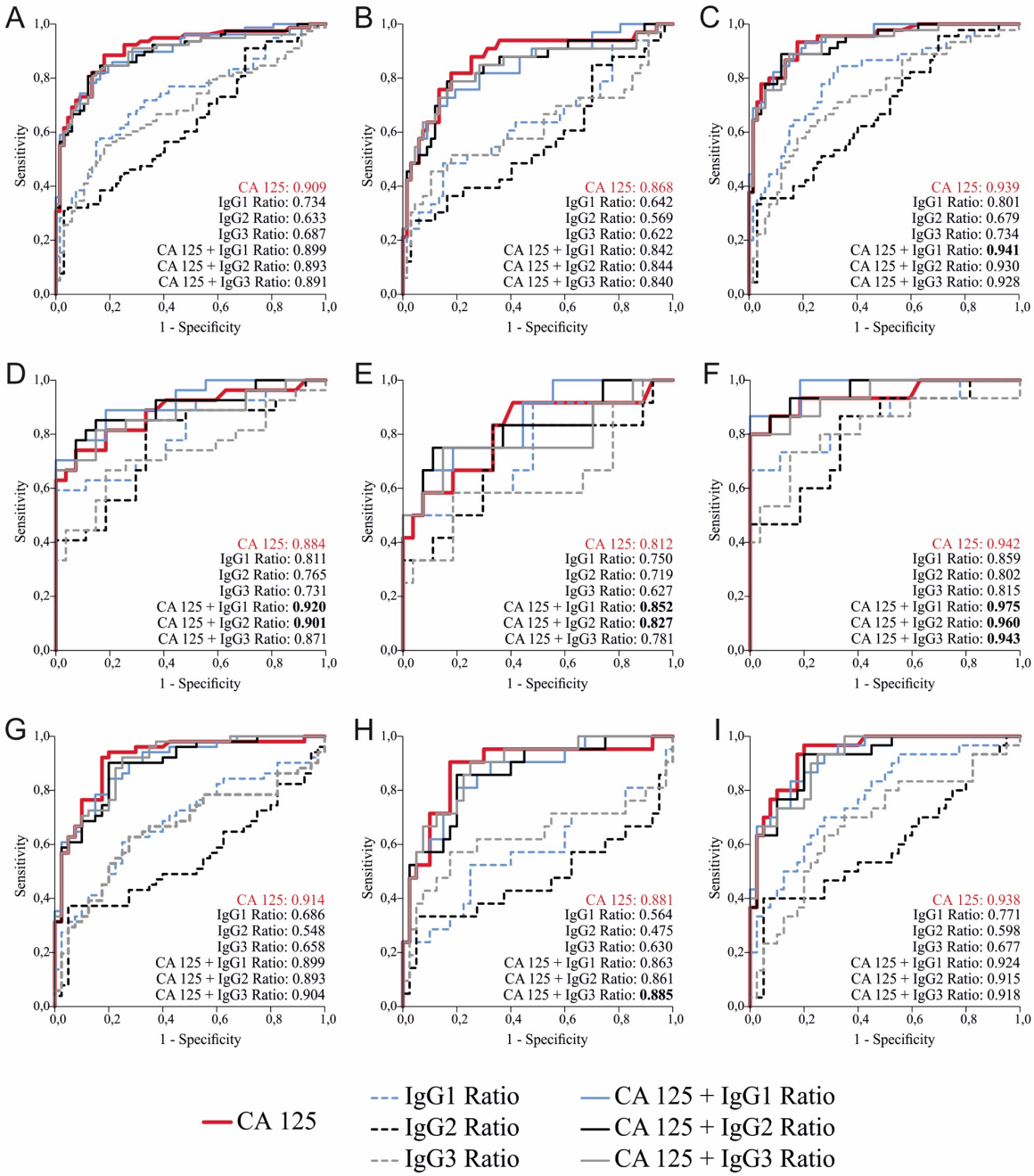

Figure 21. ROC curves for CA 125 diagnostic marker, IgG subclass-specific glycosylation ratios (G0F/(G1F+G2F×2), and CA 125 in combination with respective IgG glycosylation ratios. To determine the effect of age and EOC stage, ROC curves were generated separately for (A) all healthy controls and all EOC patients, (B) all healthy controls and all early-stage EOC patients, (C) all healthy controls and all late-stage EOC patients, (D) healthy controls and EOC patients younger than 56, (E) healthy controls and early-stage EOC patients younger than 56, (F) healthy controls and late-stage EOC patients younger than 56, (G) healthy controls and EOC patients older than 55, (H) healthy controls and early-stage EOC patients older than 55, (I) healthy controls and late-stage EOC patients older than 55. Area under the curve (AUC) values are shown for all generated curves, with AUC of CA 125 being shown in red. AUCs superior to the AUC of CA 125 alone are indicated in bold.

this of late-stage EOC rather than being an intermediate stage between healthy controls and late-stage EOC.

Finally, the diagnostic potential of IgG subclass-specific glycosylation alterations was evaluated using the ROC curve analysis as in Qian et al. [154]. To allow comparison with literature data, IgG glycosylation was defined as a G0F/(G1F+G2F×2) ratio, calculated separately for each IgG subclass. As visible in *Figure 21*, separate ROC curves were generated for CA 125, each IgG subclass-specific glycosylation ratio, and a combination of CA 125 with each respective IgG subclass-specific glycosylation ratio, obtained via binary logistic regression modeling. To address the effect of patients' age, ROC curve analyses were conducted at first using the entire cohort (non-age stratified; *Figure 21 A-C*) and, subsequently, using only the younger (≤ 55 years of age; *Figure 21 D-F*) or the older (≥ 56 years of age; *Figure 21 G-I*) cohorts separately. Similarly, to address the effect of disease stage, ROC analyses were first conducted on the whole EOC cohort (*Figure 21 A, D, G*) and then exclusively on the early- (*Figure 21 B, E, H*) and the late-stage EOC (*Figure 21 C, F, I*) cohort.

As can be seen in *Figure 21*, in all ROC curve analyses, IgG glycosylation ratios alone performed worse than the CA 125 routine marker in discriminating healthy controls and EOC patients. This is in contrast to results reported by Qian et al. [154], showing that the G0F/(G1F+G2F×2) ratio is superior to CA 125 marker alone in discriminating malignant OC and benign gynecological disease. However, it is important to note that, in the latter study, investigated cohorts were decisively smaller, younger, and not exactly age-matched (OC patients: n = 32, median age = 50.5 years; benign gynecological controls: n = 26, median age = 45 years), which could falsely enhance the performance of the IgG glycosylation-based ratio. Consistently, in the here presented study, the performance of each IgG subclass-specific glycosylation ratio was noticeably improved when only younger individuals were included in the analysis (*Figure 21 D-F*). For instance, while in the total cohort analysis area under the curve (AUC) values of IgG_1-, IgG_2-, and IgG_3-specific ratios were 0.734, 0.633, and 0.687 (*Figure 21 A*), respectively, they were increased to 0.811, 0.765, and 0.731 when only the younger cohort was analyzed (*Figure 21 D*). These observations further confirm that age-related glycosylation differences, being particularly evident in older individuals, obscure EOC-specific alterations and hinder disease detection.

Consequently, as visible in *Figure 21 A-C* and *G-I*, the combination of CA 125 with the IgG glycosylation ratio did not improve the diagnostic performance of CA 125 marker alone when the analysis was conducted on the entire non-age stratified cohort or the older cohort exclusively. On the contrary, when including only the younger cohort (*Figure 21 D-F*), the combination of CA 125 marker with IgG glycosylation ratios displayed better diagnostic potential than CA 125 alone (values superior to CA 125 alone are indicated in bold). Regardless of patients' age and disease stage, the best diagnostic performance was achieved for the combination of CA 125 with the IgG_1-specific glycosylation ratio, indicated in *Figure 21* with the blue continuous line.

5. Discussion

The aim of this study was to investigate the EOC-related glycosylation changes in the three most abundant IgG subclasses, namely IgG_1, IgG_2, and IgG_3, by means of MALDI-TOF-MS and to determine whether IgG subclass-specific glycosylation alterations have the potential to aid EOC detection. IgG glycosylation in OC has already been investigated by several research groups [152-155, 166], which demonstrated quantitative changes at the level of agalactosylation/galactosylation. Nevertheless, in a vast majority of previous studies, the analysis of IgG glycosylation was performed at the level of enzymatically released *N*-glycans. Due to the fact that 15–20% of circulating IgG molecules contain additional *N*-glycosylation sites within variable domains of their Fab fragments, such an approach generated information that is neither Fc/Fab site- nor subclass-specific. Hence, to provide more detailed information, in this study, the analysis of EOC-related changes in IgG glycosylation was performed at the level of tryptic glycopeptides. The incorporation of a two-step IgG affinity separation ensured the subclass-specificity of obtained glycosylation profiles and allowed a separate examination of the three most abundant IgG subclasses.

In agreement with previous studies [152-155], EOC was found to be associated with increased IgG agalactosylation and, correspondingly, decreased IgG galactosylation (in this study categorized as mono- and digalactosylation) in all investigated subclasses. Notably, these particular alterations were shown to have relevant biological consequences. Above all, agalactosylated IgG glycoforms were demonstrated to act in a pro-inflammatory manner, as they can activate the complement system via the alternative and the lectin pathway [132, 133, 167]. While molecular regulations of the above-described changes are still unclear, in rheumatoid arthritis, a similar pattern of reduced IgG galactosylation was shown to result from decreased activity of galactosyltransferase in IgG-producing plasma B cells [168].

Besides an EOC-related increase in agalactosylation/decrease in galactosylation, observed consistently in all three IgG subclasses, this study revealed some distinct subclass-specific trends. Among all investigated subclasses, IgG_1 showed the most prominent EOC-related glycosylation alterations. Precisely, it displayed the greatest reduction in mono- and digalactosylated glycopeptides and was the only subclass whose sialylation was significantly decreased in both the younger and the older EOC group. These findings imply that, in the face of EOC, IgG_1 undergoes the strongest transformation toward a pro-inflammatory phenotype and hence might play a particularly important role in EOC development and progression. Furthermore, IgG_1 was found to be the only subclass, in which EOC was accompanied by a significant increase in fucosylation. Interestingly, as the above trend was observed exclusively in advanced-stage EOC patients of the older group, this finding seems to be consistent with the results of Plomp et al. [162], who demonstrated that increased IgG fucosylation is characteristic for individuals with high systemic inflammation, a phenomenon known

to occur in both OC patients [169] and aged individuals [170]. Notably, as IgG core-fucosylation is known to reduce binding affinity toward FcγRIIIa and FcγRIIIb receptors, its increase can lead to reduced ADCC activity [171]. While detrimental to patients, reduced IgG_1 ADCC activity might be advantageous for cancer progression.

Most importantly, IgG_1 agalactosylation showed the strongest association with the CA 125 diagnostic marker, and the combination of IgG_1 glycosylation and CA 125 showed the best performance in distinguishing healthy controls from EOC patients. These observations are in line with the results of Ruhaak et al. [155] showing that glycopeptides of IgG_1 exhibit the highest diagnostic potential in EOC. It is important to note that IgG_1 has been suggested to play the most important role in tumor immunity, as it was the only IgG subclass whose decreased serum concentration was significantly correlated with poor prognosis in gastric cancer patients [172].

Being marked by notably high agalactosylation, the glycosylation profile of IgG_2 was found to be pretty different from those of IgG_1 and IgG_3. This finding provides strong proof that a common approach of simultaneous IgG_2 and IgG_3 analysis might lead to misleading results. As compared to other subclasses, in the total cohort analysis, IgG_2 glycosylation displayed the weakest EOC-related differences and the weakest association with the CA 125 marker. These observations seem to be in line with the results of Plomp et al. [162] showing that IgG_2 glycosylation is only weakly associated with markers of inflammation and metabolic health. Likewise, IgG_2 was reported to exhibit the lowest affinity for FcγRs and the lowest ADCC activity among all IgG subclasses [115, 125]. In addition, decreased IgG_2 concentration was reported in numerous cancer types, e.g., ovarian, gastric, and liver cancer [68, 162, 173], indicating that, just like in the case of inflammation, IgG_2 might play only a secondary role in cancer development. Yet, age- and disease stage-stratification implemented in this study provided evidence that the low discriminative potential of IgG_2 in the non-stratified cohort might be caused by a strong age-dependence of its glycosylation profile. Indeed, when including only younger individuals in the analysis, EOC-related IgG_2-specific glycosylation alterations became more evident, with statistically significant differences being detected already in early-stage EOC patients. Yet, since age- and disease stage-stratification reduced the number of patients in individual groups, those findings should be confirmed in a large multi-center study.

An essential part of this work was the investigation of IgG_3-specific glycosylation changes in EOC patients since it has not been studied so far. Despite constituting only 5–8% of total IgG, IgG_3 deserves special attention, as for many reasons it is a unique IgG subclass. Due to a particular feature of its amino acid sequence, namely the presence of arginine at position 435, IgG_3 does not bind to Protein A, which allows its separation from the other IgG subtypes [174]. Moreover, its superior affinity toward activating FcγRs and C1q makes IgG_3 the strongest inducer of Fc-mediated effector functions that include ADCC and CDC [115]. Yet, despite its discrete character, IgG_3 glycosylation

is rarely determined individually. Instead, it is investigated in a combination with IgG_2, which, as shown in this study, has a noticeably different glycosylation profile. In fact, the glycosylation profile and EOC-related glycosylation changes of IgG_3 were found to more closely resemble those of IgG_1 rather than IgG_2.

In line with previous studies [173, 175], IgG_3 was found to be characterized by overall high sialylation, which consequently decreased in EOC patients. Although the molecular regulation of elevated IgG_3 sialylation is not yet understood, it could result from better accessibility of IgG_3 Fc-attached *N*-glycans for sialyltransferases due to structural differences within its Fc-part [174]. In addition, it was suggested that increased IgG_3 sialylation could partly result from different processing by soluble B-cell-independent sialidases and sialyltransferases circulating in blood [176]. Notably, as the addition of sialic acid was shown to act as a functional switch turning IgG molecule from a pro- to an anti-inflammatory state, in physiological conditions (healthy controls), high IgG_3 sialylation could play a protective role by limiting excessive inflammatory responses. Contrarily, a strong EOC-related decrease in IgG_3 sialylation observed in the younger cohort might reflect disease-related transformation toward a pro-inflammatory state, a phenomenon described in other cancer types [63, 68].

IgG glycosylation was investigated in various cancer types, revealing associations with therapy response, survival rate, and diagnostic markers. In gastric cancer patients, a high level of digalactosylated IgG_2 glycoforms was an indicator of better survival [68], whereas proposed by Qin et al. [177] IgG glycosylation-based model was able to accurately predict the response to neoadjuvant therapy. In prostate cancer, the ratio of agalactosylated IgG structures to the sum of mono- and digalactosylated IgG correlated with the level of prostate-specific antigen (PSA), the most commonly used prostate cancer biomarker [65]. In this study, IgG agalactosylation showed a strong positive association with CA 125, the routine ovarian cancer marker. Importantly, even though comparisons between IgG glycosylation and the CA 125 marker were already reported [154, 155], this is the first study that shows the association of IgG glycosylation with CA 125 in a subclass-specific manner. Interestingly, while in all subclasses agalactosylation was significantly associated with the CA 125 marker, the strongest relation was observed for IgG_1 and IgG_3.

In agreement with previous studies [158, 159, 178], glycosylation profiles of all investigated IgG subclasses were found to alter with increasing age. Interestingly, glycosylation of IgG_1, which displayed the most pronounced EOC-related alterations, the strongest association with the CA 125 marker, and the best diagnostic potential, was the least affected by age. Consistently, in both IgG_2 and IgG_3, whose glycosylation profiles showed strong age-dependence, EOC-related alterations were less pronounced and detected primarily in the younger cohort. In line with these findings, the combination of IgG glycosylation with CA 125 displayed the best diagnostic potential when

distinguishing healthy controls and EOC patients of the younger group. All in all, these findings indicate that age-related glycosylation changes diminish differences between healthy controls and EOC patients, hindering discrimination of the disease, particularly in older individuals.

To summarize, by investigating EOC-related IgG glycosylation changes in a subclass-specific manner this study helps broadening the current understanding of EOC pathogenesis. Notably, while glycosylation alterations of all investigated IgG subclasses were observed to follow similar patterns, EOC-related changes were the most pronounced in IgG_1, which indicates its particularly important role in EOC. As subtle subclass-specific characteristics were also observed, this study highlights the importance of a separate analysis of IgG subclasses, especially with respect to IgG_2 and IgG_3.

Chapter IV *In situ N*-glycosylation of epithelial ovarian cancer tissue

1. Introduction

1.1. Glycan visualization in tissues

Aberrant protein glycosylation is a proven hallmark of cancer. While cancer-associated glycosylation alterations were broadly investigated at the level of total serum and individual serum proteins, much less is known about alterations occurring directly within affected tissues. In particular, so far, there is limited data available on *in situ N*-glycosylation in cancer, as a majority of studies included tissue homogenization in their analytical workflow prior to *N*-glycan release. Having in mind that *N*-glycans are essential for a great variety of biological processes, e.g., cell-cell communication and signaling, unraveling the glycosylation changes occurring directly on cancer cells and within their surrounding provides information of great diagnostic, prognostic, and therapeutic value.

1.1.1 Glycan-binding proteins

So far, the most common approach for visualizing tissue-contained carbohydrates has been by using specific glycan-binding proteins (GBPs), among others, lectins and anti-carbohydrate antibodies.

1.1.1.1. Lectins

Lectins constitute a large group of carbohydrate-binding proteins of non-immune origin that occur ubiquitously in plants, animals, microorganisms, and viruses. Based on their binding preferences, lectins were initially categorized as galactose-, GalNAc-, glucose-, GlcNAc-, L-fucose-, mannose-, sialic acid-, and maltose-specific [179]. However, with the emergence of data regarding their structural properties, the classification of lectins has evolved and nowadays is based on the homology of their amino acid sequence and probable evolutionary relatedness [180].

Over the decades, several hundred lectins have been identified, some of which are commercially available nowadays [181]. Notably, these primarily plant-derived GBPs have proved to be useful in a variety of analytical formats, including histochemistry, affinity chromatography, probing of electrophoretic gels, ELISA, and microarray assays [181]. The selection of commercially available lectins used as tools in glycosylation studies, together with their abbreviations, full names (referring to species of their origin), and binding specificities, are shown in *Table 9*.

Lectin-based histochemistry has readily been applied to investigate glycosylation alterations in various histopathological materials, including fresh-frozen and formalin-fixed, paraffin-embedded tissue sections. In particular, this technique has been employed to investigate glycosylation changes in cancer tissues, e.g., cervix, pituitary, pancreatic, and breast cancer [182-185].

Table 9. Lectins commonly used in N-glycosylation studies.

Abbreviation	Lectin	Binding specificity
Con-A	*Canavalia ensiformis* (Concanavalin A)	αMan > αGlc >> GlcNAc
LCA	*Lens culinaris*	αMan > αGlc >> GlcNAc
PEA	*Pisum sativum*	αMan > αGlc >> GlcNAc
WGA	*Tritricum vulgare* (Wheat germ agglutinin)	terminal β1,4-GlcNAc >> Neu5Ac
DSA	*Datura stramonium*	chitobiose core; β1,4-GlcNAc oligomer
PHA-L	*Phaseolus vulgaris leucoagglutinin*	tri-/ tetraantennary complex-type oligosaccharides
PHA-E	*Phaseolus vulgaris erythroagglutinin*	bisecting GlcNAc; biantennary complex-type *N*-glycans
RCA	*Ricinus communis*	βGal
AAL	*Aurelia aurantia*	α1,6-L-Fuc; α1,3-Fuc linked to *N*-acetyllactosamine
LTL	*Lotus tetragonolobus*	α1,3-L-Fuc linked to *N*-acetyllactosamine
MAL-I	*Maackia amurensis I*	Neu5Ac-α(2,3)Gal/GalNAc
SNA	*Sambucus nigra*	Neu5Ac-α(2,6)Gal/GalNAc; GalNAc
PSL	*Polysporus squamosus*	Neu5Ac-α(2,6)Gal/GalNAc (*N*-glycan-specific)

Lectin histochemistry can be executed either directly or indirectly as represented schematically in *Figure 22*. In the direct method, lectin binding is detected due to the presence of a fluorescent or an enzymatic label conjugated directly onto the lectin. In the indirect method, the binding of a native, unconjugated lectin to its carbohydrate ligand is typically visualized with the help of a labeled lectin-specific antibody. While the former approach is usually quicker and cheaper, it frequently suffers from reduced sensitivity, and its use is mostly restricted to the detection of highly abundant carbohydrate antigens. On the contrary, the more laborious indirect approach is more sensitive and allows detecting less abundant ligands. However, due to the use of secondary antibodies, this method is expensive and frequently suffers from non-specific background staining [181, 186].

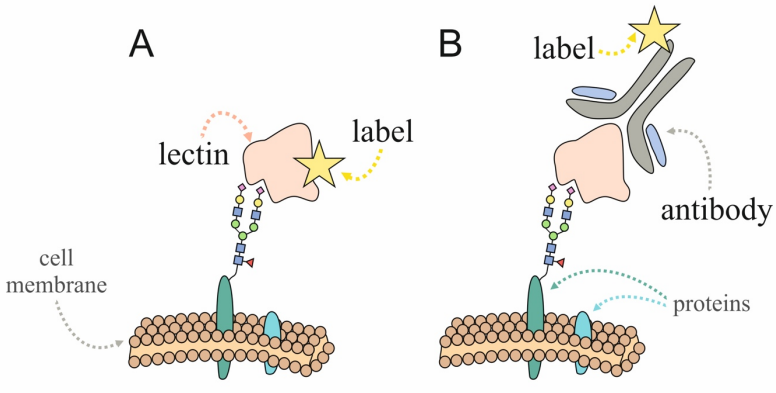

Figure 22. Lectin histochemistry. (A) Direct and (B) indirect methods are shown.

Despite their broad availability and affordable costs, the use of lectins for *N*-glycan visualization in tissues is limited by the low-affinity and low-specificity binding towards their designated carbohydrate epitopes. For low-molecular-weight epitopes, such as mono- and disaccharides, dissociation constant (K_d) values are frequently in the high micromolar to low millimolar range,

indicating very weak lectin-carbohydrate interactions [180]. Consequently, for many lectins, multivalent interactions are necessary to elicit high-avidity binding, which prerequisite cannot always be met in biological materials [187]. Additionally, as the majority of lectins recognize terminal structural epitopes of 2-4 monosaccharides, they rarely allow precisely defining the type and carrier of detected glycan (e.g., *N*-glycan, *O*-glycan, glycolipid). For instance, while SNA and MAL-I were reported to predominantly react with α2,6- and α2,3-linked sialic acid on *N*-glycan epitopes, respectively, both of these lectins are able to weakly bind sialylated *O*-glycan structures. Additionally, in the absence of sialic acid residues, these two lectins can also react with structures terminating with GalNAc or Galβ1-4GlcNAc epitopes [188, 189]. Hence, due to their broad specificities, lectins have primarily been used to monitor general alterations of tissue-contained carbohydrates and to track distinct epitope types, e.g., glycans containing terminal fucose.

1.1.1.2. Anti-carbohydrate antibodies

Anti-carbohydrate antibodies (ACAs) are naturally found in human and animal bodies. For instance, in humans, a representative pool of serum-contained IgM and IgG molecules recognizes diverse carbohydrate antigens. Among the most abundant are those targeting α-rhamnose and α-1,3-linked galactose, two epitopes widely occurring on gut microbial glycoconjugates, as well as those targeting Neu5Gc, a non-human monosaccharide, incorporated into human cells from dietary sources such as red meats [190, 191].

Like lectins, ACAs are being employed to determine the expression of carbohydrate antigens in biological samples using a variety of analytical techniques, including immunohistochemistry, Western blotting, ELISA, and antibody arrays. Additionally, some highly specific ACAs found usage in diagnostic and clinical applications, with the best-known examples being anti-CA 19-9 and anti-GD2 antibodies. The CA 19-9-specific antibody recognizes sialyl-Lewis A antigen, a tetrasaccharide structure with a composition αNeu5Ac(2,3)-β-D-Gal(1,3)(α-L-Fuc[1,4])-D-GlcNAc that serves as a tumor marker for pancreatic cancer [192]. In turn, anti-GD2 antibodies, which target disialoganglioside-GD2, are used for treatment of neuroblastoma [193].

Over the years, more than 1000 monoclonal ACAs have been reported, of which approximately one-third is commercially available [194]. Yet, as many of them recognize the same glycan epitopes, the actual number of ACAs targeting unique glycan determinants is considerably lower. Although there are some commercially available ACAs targeting *O*-glycan-, glycosaminoglycan-, and glycolipid-specific carbohydrate epitopes, there are currently no commercial antibodies recognizing epitopes typical of *N*-linked glycans [195]. At most, a small number of *N*-glycan-specific ACAs isolated from blood sera of HIV patients are available via consortia (e.g., National Institute of Health AIDS Reagent program). However, as they were shown to recognize families of structurally

related *N*-glycans (e.g., high-mannose *N*-glycans) rather than a single distinct *N*-glycan structure, they are unsuitable for precise *N*-glycan profiling [194].

The majority of commercially available ACAs are raised in murine rodents and are of IgM isotype [194]. They are typically generated by immunizing the host animal with natural materials, including whole-cell lysates, cell and/or tissue preparations, purified glycoproteins, glycosaminoglycans, glycolipids, and synthetic antigens, e.g., bovine or human serum albumin conjugates. Eventually, generated carbohydrate-specific antibodies are isolated from the host animal's serum by affinity chromatography [196]. Nevertheless, due to similarities between the human and murine glycomes, many carbohydrate determinants are poorly immunogenic. In consequence, immunization of rodents with human material frequently results in the formation of low abundant and unspecific ACAs. While for some glycan epitopes antigenic response can be enhanced by using unique knockout mice strains that lack enzymes synthetizing particular carbohydrate structures [196], this issue significantly hinders the development of carbohydrate-specific antibodies. As a result, the currently available ACAs cover only a narrow set of all described carbohydrate structures.

Moreover, similarly to lectins, a majority of available ACAs recognize carbohydrate epitopes composed of 1-4 monosaccharides [195]. As such, they typically do not allow defining the type of carrier glycan. Additionally, recent data indicate that many ACAs might be far less specific than officially reported. In fact, as determined in the carbohydrate microarray binding study, 14 of 27 tested commercially available antibodies were observed to display substantial cross-reactivity, whereas 2 did not show any binding to their designated carbohydrate antigen [197]. This inaccuracy might lead to a false over- or underestimation of respective carbohydrate antigen expression levels in an investigated biological material.

1.1.2 MALDI-MSI

As opposed to lectin- and antibody-based methods, MALDI mass spectrometry imaging (MALDI-MSI) is a non-targeted technique that enables highly sensitive and specific visualization of tissue-contained analytes. The description of MALDI-MSI as a tool for *in situ* analysis of *N*-glycans in tissue specimens can be found in section *3.2.2. MALDI-MS Imaging* of *General Introduction*.

1.2. MALDI-MSI of *N*-glycans in cancer tissues

By combining mass spectrometry and histology, MALDI-MSI allows visualizing tissue-specific glycosylation changes that occur upon the development and/or progression of cancer. In fact, since MALDI-MSI is compatible with both frozen and formalin-fixed paraffin-embedded (FFPE) tissue materials, it allows retrieving data from a large number of archival FFPE samples, which makes it invaluable for cancer biomarker discovery.

In the last decade, MALDI-MSI has been successfully applied to investigate *in situ N*-glycosylation in a number of malignant tissues, among others, liver, prostate, pancreatic, ovarian, and colorectal cancer [113, 198-200]. As opposed to the classical analytical approach that requires tissue homogenization and extraction of analytes, in the above-mentioned MALDI-MSI studies, the *N*-glycan profiling was obtained while retaining intact tissue architecture. Importantly, the information generated in this way was not only site-specific but also provided a great insight into the tumor microenvironment. Typically, *in situ* PNGase F digestion allowed the detection of 15-60 unique *N*-glycan structures per tissue, of which many displayed highly regiospecific distribution. In particular, *N*-glycans of high-mannose-type were repeatably shown to be abundant in tumor regions of investigated tissues. This trend is believed to reflect a disrupted/incomplete *N*-glycan biosynthesis that occurs in rapidly proliferating cancer cells. Compared to high-mannose *N*-glycans, the tissue distribution of complex-type *N*-glycan structures was shown to be more differential and dependent on the glycan composition, e.g., the presence or absence of core-fucose. For instance, in colon adenocarcinoma, the distribution of the biantennary *N*-glycan structure H5N4 at *m/z* 1663.3 was shown to be different as compared to its core-fucosylated H5N4F1 counterpart. In fact, while both of these structures were predominantly detected in tissue stroma, the H5N4F1 *N*-glycan was noticeably more abundant and detected as well in adenocarcinoma regions of the colon tumor tissue [201]. In the case of tri- and tetraantennary *N*-glycan structures, the spatial distribution within the tissue was shown to vary not only depending on the presence or absence of fucose residue but also on the type of investigated tissue. For instance, while in colon carcinoma the triantennary fucosylated *N*-glycan H6N5F1 (*m/z* 2174.9) was equally abundant in stroma and adenocarcinoma regions, in ovarian cancer, the same structure was detected only in stroma [200, 201]. So far, little reliable information is available regarding sialylated *N*-glycans in cancer tissues, as their detection was, to a considerable extent, impeded by ionization biases and sialic acid loss due to in- and post-source fragmentation. So far, the distribution of sialylated *N*-glycans could be accurately profiled only in few studies, in which labile sialic acids were chemically stabilized [113, 202] Interestingly, as demonstrated for colon carcinoma, α2,3- and α2,6-sialylated *N*-glycans showed distinct tissue distribution. Precisely, while α2,3-sialylated structures were mainly observed in stroma, tumor, and necrotic regions, α2,6-sialylated structures were mostly localized to necrotic and collagen-rich areas [113]. In turn, in pancreatic cancer tissue, sialylated *N*-glycan structures were predominantly observed in primary tumor and tumor stroma regions, with α2,3-sialylated structures being mostly detected in stroma, whereas tumor regions were observed to be decorated with a mixture of α2,3- and α2,6-sialylated *N*-glycan structures.

1.2.1. MALDI-MSI of *N*-glycans in ovarian cancer tissue

At the time of writing this thesis, there were only two published studies in which MALDI-MSI technique was employed to determine *in situ* *N*-glycosylation in ovarian cancer tissue, namely Everest-Dass et al. [200] and Briggs et al. [203].

Everest-Dass et al. [200] performed the analysis of three FFPE tissue sections, all of which were derived from different FIGO stage III OC patients. In parallel to MALDI-MSI analysis, the OC *N*-glycome was investigated off-tissue using porous graphitized carbon (PGC)-LC-ESI-MS/MS, operated in negative ionization mode. In total, the latter combined methodology allowed the detection of 40 individual *N*-glycan masses that included high-mannose-, hybrid-, and complex-type structures. The spatial distribution of detected *N*-glycans was shown to be class- and tissue type-dependent. Specifically, high-mannose *N*-glycans were predominantly detected in tumor regions, pauci-mannose (*N*-glycans composed of three to four mannose residues attached to a chitobiose core) were indicative of adipose tissue, whereas both complex-type neutral and sialylated *N*-glycans were primarily observed in the adjacent stromal regions. Based on their results, Everest-Dass et al. proposed four distinct *N*-glycan structures as discriminants of different tissue types. These were as follows: the biantennary H3N4 structure at *m/z* 1339.4 for necrotic tissue, the triantennary core-fucosylated H6N5F1 structure at *m/z* 2175.5 for stroma, the high-mannose H8N2 structure at *m/z* 1743.5 for tumor regions, and the pauci-mannose H3N2 structure at *m/z* 933.3 for adipose tissue regions. The discriminative potential of the above-mentioned glycans was confirmed by ROC curve analyses, which showed high AUC values ranging between 0.84 and 0.99.

In the follow-up study of Briggs et al. [203], investigated material included three early- and three late-stage serous OC tissue specimens as well as one tissue microarray (TMA) slide consisting of six cores of FIGO stage I and seven cores of FIGO stage III OC tissue, all of which were FFPE tissues. The aim of this study was to determine whether tissue-contained *N*-glycans have the potential to serve as markers of OC progression. As in the study of Everest-Dass et al. [200], the MALDI-MSI was accompanied by negative ionization mode PGC-LC-ESI-MS/MS analysis of tissue-extracted *N*-glycans. Although this combined methodology allowed the detection of 42 *N*-glycan structures, only 14 signals corresponding to *N*-glycans were observed in MALDI-MSI spectra. Based on obtained ion intensity maps, high-mannose *N*-glycans were reported to be clearly more abundant in late-stage as compared to early-stage OC tissues. Likewise, some complex-type neutral and sialylated structures, including H5N4F1 at *m/z* 1809.6 and H5N4S1 at *m/z* 1977.6, and the bisected structure H5N5F1 at *m/z* 2012.7 were observed only in the late-stage OC tissues. However, while high-mannose structures were shown to be predominantly localized to tumor regions, the distribution of complex-type neutral *N*-glycans in late-stage OC tissues was less tissue type-specific, as they were abundant in both tumor and adjacent stroma regions. In fact, only some individual complex-type neutral *N*-glycan structures showed distinct tissue type-specific distribution. For instance,

the biantennary fucosylated H3N4F1 structure at *m/z* 1485.5 was shown to be indicative of tissue necrotic regions, whereas the above-mentioned H5N4F1 (*m/z* 1809.6) was predominantly detected in tumor regions of late-stage OC tissue. Regarding TMA material, the MALDI-MSI analysis resulted in the detection of only 12 *N*-glycan-specific *m/z* values, which was due to the lack of detection of sialylated *N*-glycan structures. Only two *N*-glycan structures out of the 14 detected, namely H5N4F1 at *m/z* 1809.6 and H4N4F1 at *m/z* 1647.6, were more prominent in tissue cores of late-stage OC.

Importantly, although in the above-mentioned studies some *N*-glycan discriminants of OC tissue regions were proposed, the presented data might, to a considerable extent, be distorted by inadequate detection of sialylated *N*-glycans. In fact, as positive ion mode MALDI-MSI analysis was performed without stabilizing labile sialic acid residues, the in- and post-source fragmentation of sialic acid residues most likely contributed to erroneously low or no detection of sialylated *N*-glycans and, in consequence, inadequately high detection of their neutral counterparts. Due to their terminal position, sialylated *N*-glycans play a particularly important role in tissue homeostasis and pathology. Further analysis should be performed to reliably profile their occurrence, distribution, and sialic acid-linkage in OC tissue.

2. Materials and equipment

2.1. Materials

Chemicals and consumables:

- 1-Hydroxybenzotriazole hydrate (HOBt; Sigma-Aldrich, Germany)
- 1-Ethyl-3-(3-(dimethylamino)propyl) carbodiimide (EDC; Fluorochem, UK)
- 3'-Sialyl-*N*-acetyllactosamine (3'-SialLacNAc; Sigma-Aldrich, Germany)
- 6'-Sialyl-*N*-acetyllactosamine (6'-SialLacNAc; Sigma-Aldrich, Germany)
- α-2,4-hydroxycinammic acid (CHCA; Bruker Daltonics, Germany)
- Amicon Ultra-0.5 ml centrifugal filters 10 kDa (Merck, Germany)
- Citric acid (Carl Roth, Germany)
- Dextran hydrolysate prepared in-house from Dextran (DH; Oxford, UK)
- Eosin Y (Sigma-Aldrich, Germany)
- Eukitt (O. Kindler, Germany)
- IGEPAL CA-630 (Sigma-Aldrich, Germany)
- Indium tin oxide (ITO) glass slides (Bruker Daltonics, Germany)
- Natrium hydroxide (NaOH; Sigma-Aldrich, Germany)
- Peptide Calibration Standard II (Bruker Daltonics, Germany)
- Poly-L-lysine (Sigma-Aldrich, Germany)
- Super-DHB MALDI matrix (s-DHB; Sigma-Aldrich, Germany)

Enzymes:

- PNGase F Prime (*N*-Zyme Scientifics, USA)

Solvents:

- Acetonitrile (ACN; VWR Chemicals, Germany)
- Ammonium hydroxide solution 25 % (Merck, Germany)
- Ethanol (EtOH; Merck, Germany)
- Dimethylamine 40% (DMA; Sigma-Aldrich, Germany)
- Dimethyl sulfoxide water free (DMSO; Applichem, Germany)
- Hematoxylin solution, Mayer's (Sigma-Aldrich, Germany)
- Methanol (Carl Roth, Germany)
- Milli-Q grade water
- Trifluoroacetic acid (TFA; Merck, Germany)
- Xylene (Merck, Germany)

2.2. Equipment

- Analytical scale (Sartorius, Germany)
- Block heater (Cole-Parmer, UK)
- Centrifuge Mikro 200R (Hettich, Germany)
- Coplin jars (Sigma-Aldrich, Germany)
- Drigalski spatula (Carl Roth, Germany)
- Heating oven (Heraeus Instruments, Germany)
- HTX TM-Sprayer (HTX Technologies LLC, Germany)
- Peri dishes (DWK Life Sciences, Germany)
- rapifleX MALDI Tissuetyper (Bruker, Germany)
- Reaction tray made in-house of inert material
- Slide scanner MF 5000 (Reflecta, Germany)
- Syringe pump NE-300 Just Infusion™ (New Era Pump Systems Inc., USA)
- Transmitted light microscope (Kern & Sohn, Germany)
- Ultrasonic bath, Sonorex TK52 (Bandelin, Germany)
- Vacuum desiccator (Thermo Fisher Scientific, Germany)
- Vacuum pump (Vacuubrand, Germany)
- Water bath (Elma Schmidbauer, Germany)
- Water purification system MilliQ Plus (Millipore, Germany)

3. Methods

3.1. Preparation of poly-L-lysine coated indium tin oxide glass slides

A poly-L-lysine solution was prepared by mixing 5 ml of MilliQ water with equal volume of poly-L-lysine and 10 µl of IGEPAL CA-630 in a 15-ml Falcon tube. The poly-L-lysine coating solution was aliquoted and stored at 4 °C for up to 6 months. Glass slides were wiped with 100% ethanol (EtOH), and 20 µl of the poly-L-lysine solution was dropwise spotted on their indium tin oxide (ITO)-coated side. Using a glass Drigalski spatula, the applied solution was homogeneously distributed across the slide, coating it entirely. Prepared slides were dried at 60 °C on a hot plate for 2 minutes, cooled, and stored in a slide holder at room temperature.

3.2. Tissue sample collection

All tissue specimens were collected intraoperatively at the Department of Gynecology, Charité - Universitätsmedizin Berlin and were provided by Prof. Dr. med. Elena Ioana Braicu and Prof. Dr. med. Jalid Sehouli. Written informed consent was obtained from all patients. The study was ethically approved by the Charité Institutional Ethics Committee (EA4/073/06). EOC tissue preservation and histotyping were performed by an experienced pathologist, Dr. med. Eliane Taube, at the Institute of Pathology, Charité - Universitätsmedizin Berlin. All surgical specimens were formalin-fixed and paraffin-embedded (FFPE) according to standard protocols. They consisted of two single high-grade serous ovarian carcinoma (HGSOC) tissue specimens (in duplicate) and four tissue microarrays (TMAs) composed of tissue cores of three different EOC histotypes, i.e., low-grade serous ovarian carcinoma (LGSOC), ovarian clear cell carcinoma (OCC), endometrioid carcinoma, (EC) as well as borderline ovarian tumor (BOT). Tissue sections (5 µm thickness) were water bath mounted onto the poly-L-lysine-coated indium tin oxide (ITO) glass slides. After overnight drying at room temperature, tissue slides were stored protected from light at 4 °C until further use.

3.3. Deparaffinization and rehydration of FFPE tissue sections

Prior to deparaffinization and rehydration steps, all slides were heat-treated at 60 °C for 1 h in an oven in order to denature tissue-embedded proteins and enhance the adherence of tissues to ITO glass slides. Subsequently, melted paraffin was removed by sequential washing in 100 % xylene (1×5 min, 1×10 min; each in a separate glass Coplin jar) and 100 % EtOH (2×2 min; each in a separate glass Petri dish). Afterward, the deparaffinized tissue slides were rehydrated by sequential immersing in MilliQ water (2×5 min; each in a separate glass Coplin jar), dried, and stored overnight at room temperature in a vacuum desiccator.

3.4. Antigen retrieval

Deparaffinized and rehydrated tissue slides were incubated for 10 min in near-boiling 10 mM citric acid (98 °C, pH adjusted to 6.0 with 3 M NaOH) in a glass Coplin jar. This was followed by 30 min

incubation at 98 °C on a heating plate. After cooling down, slides were immersed in MilliQ water (2×1 min; each in a separate glass Coplin jar) and dried in a vacuum desiccator (~10 min).

3.5. Chemical derivatization of sialic acids

Sialic acids were derivatized according to the protocol adapted from Holst et al. [113]. Briefly, dried tissue slides were incubated in 4 ml of DMSO containing 250 mM EDC, 500 mM HOBt, and 250 mM DMA for 2 h 15 min at 60 °C in a moist chamber placed in a pre-heated oven. This was followed by addition of 1.6 ml of 25% ammonium hydroxide and further incubation for 2 h at 60 °C. Upon completion of the reaction, tissue slides were rinsed thoroughly with 100% EtOH (~15 ml) and then were sequentially immersed in fresh 100% EtOH (2×2 min; each in a separate glass Petri dish) and MilliQ water (2×5 min, each in a separate glass Coplin jar). Eventually, tissue slides were dried in a vacuum desiccator.

3.6. PNGase F buffer exchange

Prior to MALDI-MSI experiments, PNGase F PRIME enzyme was buffer-changed from 1×PBS (original solution) to MilliQ water, using a 10 kDa Amicon Ultra-0.5 ml centrifugal filter. For this purpose, the Amicon filter was first pre-rinsed and then filled with MilliQ water (450 µl). Fifteen µl of PNGase F PRIME solution (2 µg/µl; 30 µg) was added, and the Amicon filter was centrifuged at 13910×g for 10 min at 4 °C. The flow-through fraction was discarded, and the concentrated at the filter's bottom PNGase F enzyme was resuspended in 400 µl of MilliQ water. The latter step was repeated twice. Following the last washing step, the concentrated and buffer-exchanged PNGase F solution was recovered by reverse centrifugation at 3000×g for 3 min at 4 °C. Eventually, the concentrate (~60 µl) was brought up to 250 µl with MilliQ water. The PBS-free PNGase F solution was prepared freshly on the day of enzyme deposition and stored on ice until use.

3.7. On-tissue PNGase F digestion and *N*-glycan extraction

In order to test the efficacy of *N*-glycan release with buffer-exchanged PNGase F, one HGSOC tissue was subjected to on-tissue PNGase F digestion followed by *N*-glycan extraction. For this purpose, dewaxed, rehydrated, and chemically derivatized tissue was covered with buffer-changed PNGase F solution and was incubated overnight at 37 °C in a humid chamber. Notably, in order to obtain partial site-specific information, the deposition of the enzymatic solution was performed carefully in a drop-wise manner over four different tissue areas (marked A to D in *Figure 26)*. The following day, the residual solution was collected (each drop in a separate tube) and released *N*-glycans were further extracted by carefully depositing 50 µl of MilliQ water on each region of the tissue. After 15 min incubation at 37 °C, MilliQ water drops were collected with a micropipette and pooled with the residual solution collected previously. The latter step was repeated one more time. All four extracted fractions were purified using cotton-HILIC columns as described in *Chapter III: 3.5. Cotton-HILIC*

purification and eventually were measured in MALDI-TOF-MS in positive ionization mode using super-DHB as MALDI matrix.

3.8. *In situ* PNGase F deposition and digestion

The PNGase F solution (~250 µl/slide) was homogeneously deposited on each tissue slide using an automated spraying device (HTX TM-Sprayer). Prior to spraying the enzyme, the sprayer's wires were flushed with 50% ACN for 30 min at a flow speed of 30 µl/min. The enzymatic solution was introduced into the sprayer device using a glass syringe equipped with a Luer-lock. The tissue slides were mounted on the spraying platform and secured with adhesive tape. The localization of the tissue within the glass slide (X and Y coordinates) was specified, allowing 5-mm additional edge for the spray head to turn around off the tissue. The spraying parameters were set as follows:

- Temperature: 30 °C
- Flow rate: 0.015 ml/min
- Passes: 15
- Pattern: criss-cross (CC)
- Velocity: 750 mm/min
- Track spacing: 2 mm
- Gas flow rate: 2 l/min
- Pressure: 10 psi
- Drying time: 0
- Noozle height: 40 mm

Following the enzymatic deposition, tissue slides were carefully transferred to the pre-heated humid chamber and were incubated overnight at 37 °C in an oven.

In order to identify *N*-glycan signals resulting from PNGase F digestion, one consecutive EOC tissue section served as a negative control and was protected from spraying with PNGase F using a glass coverslip, secured on the sides with adhesive tape. After PNGase F spraying, the glass coverslip was carefully removed, and the slide was processed exactly the same way as PNGase F-treated tissues.

3.9. Slide scanning and MALDI matrix deposition

The following day, the slides were carefully removed from the incubation chamber and were let to air-dry. Using a white Tipp-Ex, three navigation points were marked in each tissue surrounding, and the slides were scanned at high resolution using a digital slide scanner. Subsequently, 1 µl of DH standard was spotted on each slide within the tissue-free area. After drying, tissue slides were mounted on the spraying platform, and the MALDI matrix solution (CHCA, 7g/l in 70% ACN with 0.1% TFA) was deposited over entire tissue slides. The spraying parameters were set as follows:

- Temperature: 77 °C
- Flow rate: 0.1 ml/min

- Passes: 6
- Pattern: criss-cross (CC)
- Velocity: 1300 mm/min
- Track spacing: 3 mm
- Gas flow rate: 2 l/min
- Pressure: 10 psi
- Drying time: 0
- Noozle height: 40 mm

Following the spraying, tissue slides were either directly measured by MALDI-TOF-MS or stored in a vacuum desiccator until the measurement to prevent oxidation of the matrix.

3.10. MALDI-MSI measurement

The MALDI-MSI analysis was performed in positive ion reflectron mode on a rapifleX MALDI Tissuetyper system, within an *m/z* window of 1000-5000 (in the case of TMAs, an *m/z* window of 1100-5000 was used due to the presence of contamination cluster in a *m/z* range 1000-1099), a raster width of 50 µm, 500 laser shots per spot, and sampling rate of 1.25 GS s^{-1}. Acquisition of MSI data was enabled by the flexImaging 5.1 and flexControl 3.0 software (Bruker Daltonics). Prior to the measurement, external calibration was performed using a dextran ladder.

3.11. Hematoxylin and eosin staining

Following the measurement, CHCA was removed by submerging the slides in 70% EtOH for 1 min. The slides were rinsed with MilliQ water, after which they were incubated in a ready-to-use Mayer's hematoxylin solution for 10 min. The excess of hematoxylin was washed away by rinsing the slides with warm running tap water for 10 min. The efficiency of the staining was verified using a standard transmitted light microscope (cell nuclei are expected to stain blue, whereas the background/connective tissue should remain grey). Afterward, hematoxylin-stained slides were rinsed with MilliQ and were counterstained with 1-2% eosin solution for 5 min (erythrocytes should turn bright red, whereas connective tissue should stain pink/light red). Following the staining, tissue slides were rinsed with MilliQ water and then were dehydrated in increasing concentrations of EtOH (70%, 80%, 90%, 96%, 3×100%; 1 min each) and xylene (3×100%; 1 min each). In the end, hematoxylin and eosin (H&E) stained tissues were air-tightly sealed using Eukitt medium. Eventually, tissue regions were annotated by an experienced pathologist.

3.12. Data analysis

Processing of recorded mass spectra was conducted in flexControl 3.0 (Bruker Daltonics). MALDI-TOF mass spectra were total ion current normalized, and the detected peaks were revised manually. The annotation of the corresponding *N*-glycan structures was performed with the assistance of the

GlycoWorkbench software [204], based on detected *m/z* values as well as the knowledge of glycobiological processing. Statistical analysis and annotation of regions of interest were performed in SCiLS Lab software, Version 2019a Pro (Bruker Daltonics). The discriminative analysis was performed using ROC curve analysis. To correct for unequal tissue sizes, the ROC curve analyses were performed on a random subset of collected mass spectra, assuring that in each test the number of mass spectra was identical for both compared groups. An area under the curve (AUC) value of 0.65 was considered to be a cut-off value. The discriminative potential of indicated *N*-glycan structures was classified as poor (AUC between 0.65 and 0.70), fairly good (AUC between 0.7 and 0.8), good (AUC between 0.8 and 0.9), very good (AUC between 0.9 and 0.95), and excellent (AUC above 0.95).

4. Results

In-depth identification of molecular EOC features is a prerequisite for the development of novel approaches for OC diagnostics and treatment. However, to date, a majority of glycomic studies was performed with body fluids, lysed cells, or homogenized tissues as starting materials. As a result, data available on the spatial distribution of *N*-glycans in EOC tissue is still sparse, particularly in respect to tissue-contained intact sialylation. Hence, in this study, the *N*-glycosylation profile of the most common EOC histotypes was determined *in situ* using the MALDI-MSI technique.

4.1. Optimization of the analytical workflow

All investigated tissues were formalin-fixed and paraffin-embedded (FFPE). For this reason, the enzymatic *N*-glycan release was preceded by tissue dewaxing and rehydration. As shown in *Figure 23*, initially, these steps were directly followed by a linkage-specific sialic acid derivatization, according to the protocol by Holst et al. [113]. Although time-consuming, the derivatization reaction was important for two reasons: 1) it stabilizes labile sialic acids and prevents their in- and post-source decay; 2) due to implementation of two linkage-specific amidation steps, it enables the differentiation of α2,3- from α2,6-linked sialic acids and hence provides deeper biological information.

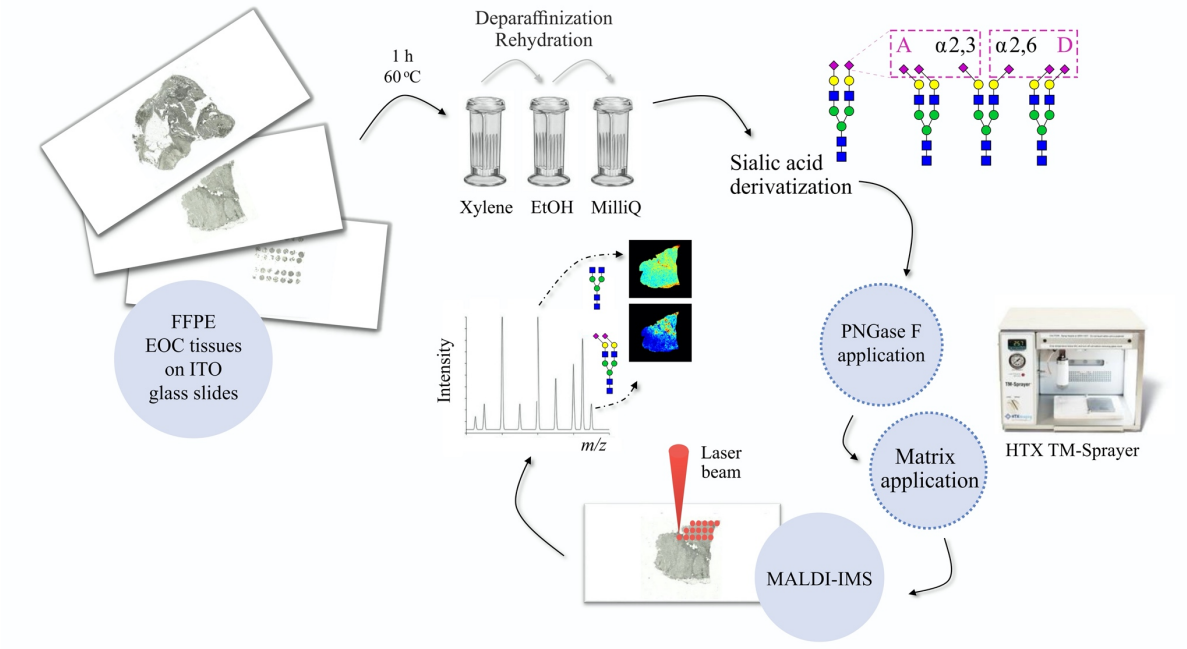

Figure 23. Schematic representation of the initial in situ N-glycan analysis workflow using MALDI-MSI technique.

The derivatization reaction, which mechanism is shown in *Figure 24A*, utilizes 1-ethyl-3-(3-dimethyl-aminopropyl) carbodiimide (EDC) as carboxylic acid activator, 1-hydroxybenzotriazol (HOBt) as catalyst, and dimethylamine (DMA) and ammonium hydroxide as donors of amine functional groups. In the first step, tissue slides are incubated with derivatization solution containing EDC, HOBt, and DMA. Under these conditions, carboxylic groups of α2,6-linked sialic acids

become stably dimethylamidated, whereas carboxylic groups of α2,3-linked sialic acids react with hydroxylic groups of the adjacent galactose residues forming unstable lactones. In the next step, all previously formed lactones hydrolyze upon the addition of ammonium hydroxide, whereas dimethylamidated α2,6-linked sialic acids remain unchanged. The reaction introduces a mass increment of 27.047 Da and a mass decrease of 0.984 Da for each α2,6- and α2,3-linked sialic acid, respectively. The specificity and efficacy of the reaction was determined off-tissue using 6'- and 3'-sialyl-*N*-acetyllactosamine (SialLacNAc) standards. As visible in *Figure 24B*, the reaction resulted in almost complete dimethylamidation of α2,6-linked sialic acids and amidation of α2,3-linked sialic acids. Following the derivatization, sialylated structures were detected predominantly as monosodiated $[M+Na]^+$ ions, which facilitates peak identification and data analysis.

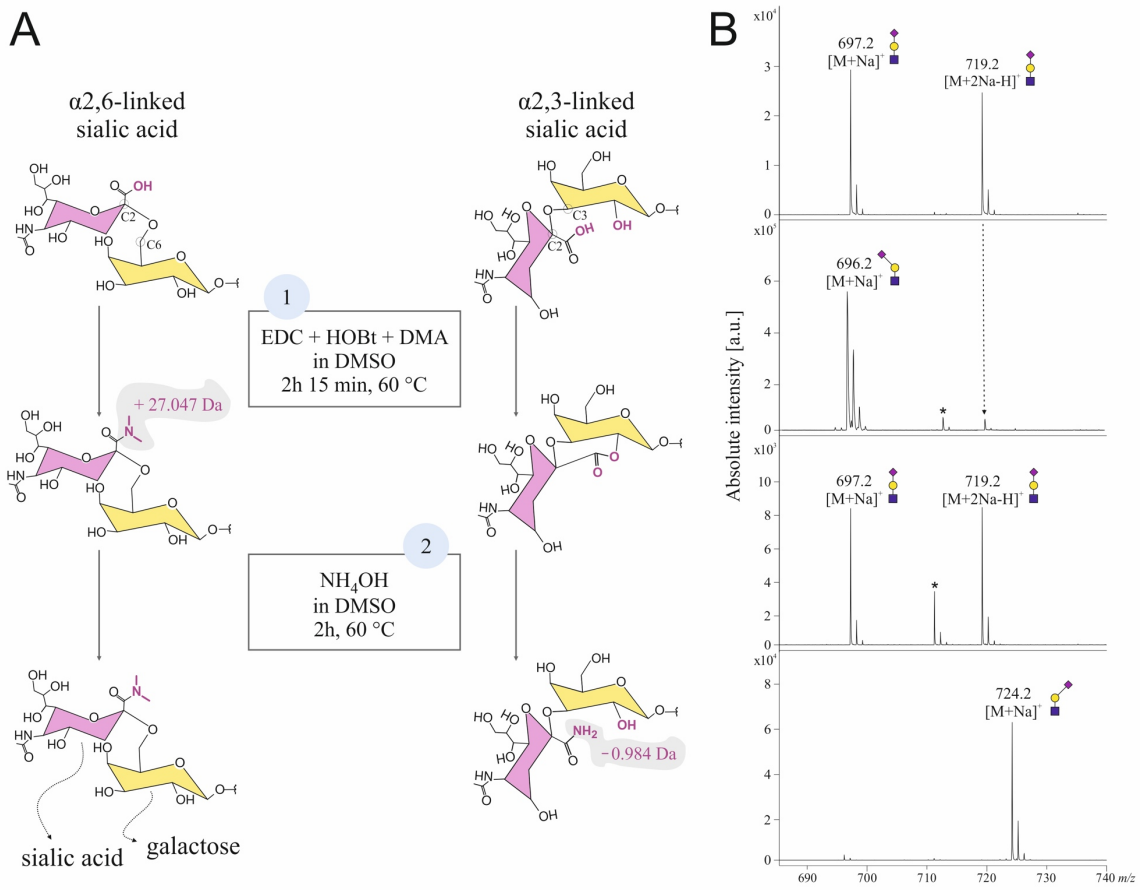

*Figure 24. Linkage-specific sialic acid derivatization. (A) Schematic representation of the reaction mechanism (modified from [113]). Sialic acid is marked in pink, whereas galactose is marked in yellow. (B) MALDI-TOF mass spectra of non-derivatized and derivatized 3'- and 6'-SialLacNAc standards. From top to bottom: underivatized 3'- SialLacNAc, derivatized 3'-SialLacNAc, underivatized 6'-SialLacNAc, derivatized 6'-SialLacNAc. Monosaccharides are represented as follows: blue square, GlcNAc; yellow circle, Gal; pink diamond, Sia. Sialic acid leaning to the left and right represents α2,3- and α2,6-linkage, respectively. * unidentified peak.*

Prior to its application on the tissue, PNGase F was buffer-changed to MilliQ water, as the original solution consisting of 1×PBS is incompatible with subsequent MALDI-MS experiments [205]. Besides suppressing the ionization, non-volatile salts, i.e., sodium chloride (NaCl) contained in 1×PBS, were observed to hinder homogeneous crystallization of MALDI matrix, which is an essential prerequisite for obtaining good-quality MALDI-MSI images. The influence of NaCl on CHCA matrix crystallization is shown in *Figure 25*.

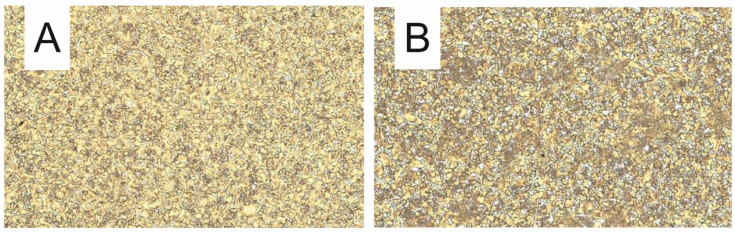

Figure 25. Microscopic pictures of CHCA MALDI matrix crystallization (A) in the absence and (B) presence of NaCl in the PNGase F enzyme solution.

Subsequently, the efficacy of tissue processing steps including the on-tissue *N*-glycan release using the buffer-changed PNGase F solution was tested. For this purpose, one single HGSOC tissue section was processed as shown in *Figure 23* up until the *N*-glycan derivatization step. Then, instead of spraying the enzyme with the HTX TM-Sprayer, the buffer-changed PNGase F solution (4×50 µl) was carefully pipetted over four separate tissue parts, as indicated in *Figure 26*. Following overnight incubation at 37 °C in a humid chamber, released *N*-glycans were extracted with MilliQ water, concentrated, and purified using self-made cotton-HILIC columns. Eventually, each extracted *N*-glycan fraction was measured separately by MALDI-TOF-MS in positive ionization mode using super-DHB as MALDI matrix.

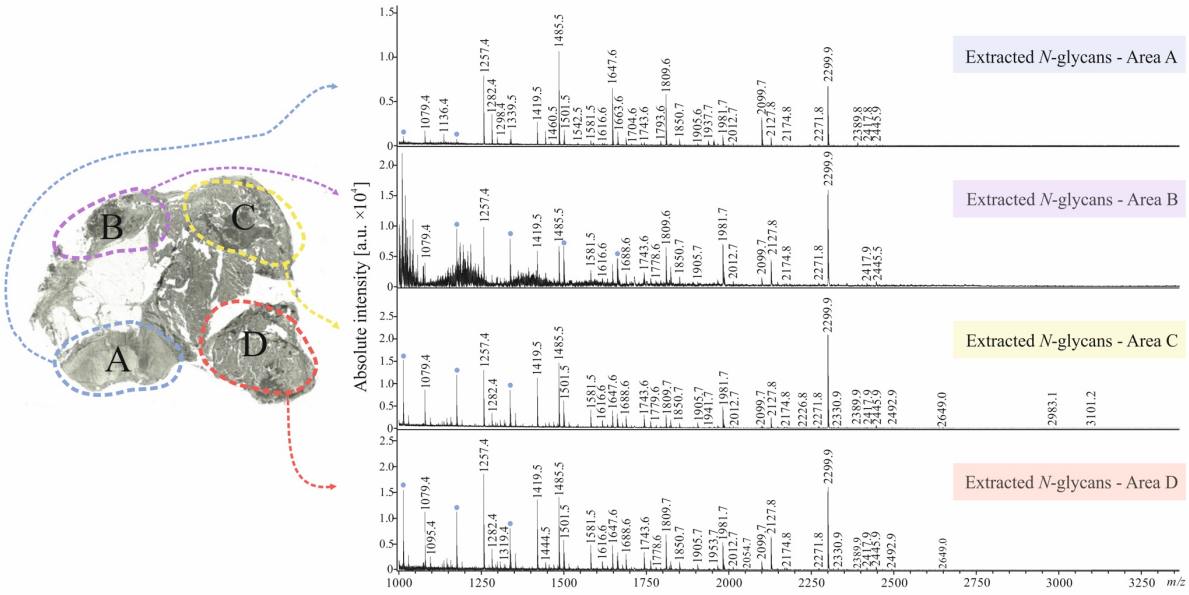

Figure 26. MALDI-TOF mass spectra $[M+Na]^+$ of N-glycan fractions extracted from different EOC tissue regions. Schematic representation of indicated m/z species are shown in Table 10. Blue dots: non-carbohydrate contaminants.

As shown in *Figure 26*, the applied procedure allowed the detection of both neutral and derivatized sialylated *N*-glycans, with *m/z* 2299.9 that corresponds to di-α2,6-sialylated biantennary complex-type *N*-glycan structure representing one of the highest peaks in all extracted fractions. Markedly, *N*-glycan profiles were found to vary between different tissue regions, highlighting the importance of site-specific *N*-glycosylation analysis.

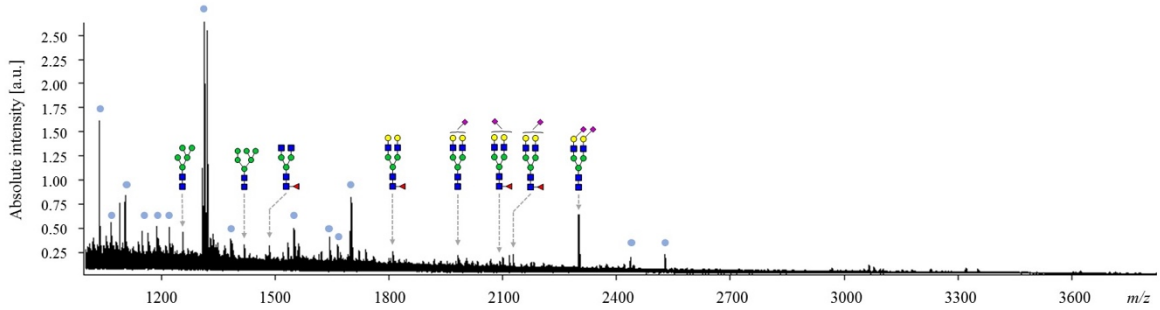

Figure 27. Average MALDI imaging mass spectrum $[M+Na]^+$ of a FFPE HGSOC tissue processed according to the protocol without antigen retrieval. Blue dots: non-carbohydrate contaminants.

Subsequently, the consecutive whole EOC tissue slide was used for the MALDI-MSI analysis, implementing the complete procedure visualized in *Figure 23*. Briefly, after chemical derivatization, the HGSOC tissue was homogeneously overlaid with the buffer-changed PNGase F solution using the HTX TM-Sprayer and incubated overnight at 37 °C in a humid chamber. The following day, the slide was covered with CHCA, the MALDI matrix, using the HTX TM-Sprayer and measured by rapifleX MALDI Tissuetyper. However, as visible in *Figure 27*, the applied procedure resulted in an inadequate *N*-glycan detection, as *N*-glycan-specific signals were minor compared to non-glycan *m/z* species observed in the average mass spectrum.

In an attempt to improve *in situ N*-glycan release and detection, the analytical workflow presented in *Figure 23* was modified by implementing a heat-induced antigen retrieval (HIAR) step, prior to the *N*-glycan derivatization. HIAR is a common immunohistochemistry technique applied in order to remove covalent cross-links introduced between proteins during the formalin fixation of the tissue. To this end, the deparaffinized and rehydrated tissue was immersed in a nearly boiling citric acid solution (98 °C, 10 min), after which it was incubated for further 30 min on a heat block pre-heated to 98 °C. Eventually, the antigen-retrieved slide was cooled down and rinsed with MilliQ water.

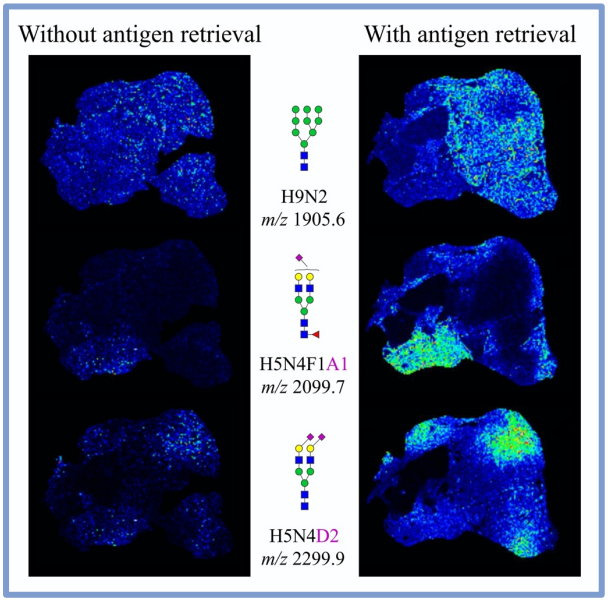

Figure 28. MALDI-MSI detection of three exemplary N-glycan structures using protocols that are either devoid of (left) or including (right) an antigen retrieval step.

Although it has been suggested that, unlike DNA, RNA, and proteins, *N*-glycans are not prone to become a part of formalin cross-linked network [206], HIAR could facilitate PNGase F digestion by improving the accessibility of buried *N*-glycan moieties. Indeed, in this work, the implementation of the antigen retrieval step noticeably improved the detection of *N*-glycans in EOC tissue. Importantly, the high temperature did not result in sialic acid loss as both α2,3- and α2,6-sialylated *N*-glycans were readily detected in the antigen-retrieved tissue (*Figure 28*).

The final analytical workflow including additionally implemented steps, i.e., HIAR and PNGase F buffer-exchange, is shown in *Figure 29*.

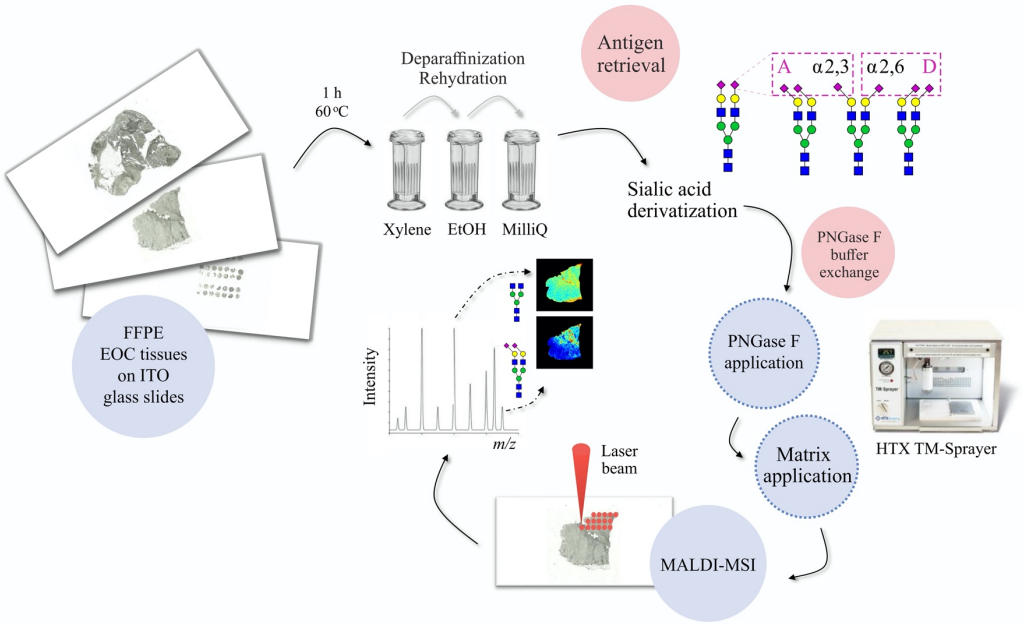

Figure 29. Schematic representation of the final in situ N-glycan analysis workflow using MALDI-MSI technique.

4.2. *In situ N*-glycosylation of EOC tissue

The optimized analytical workflow was subsequently applied to investigate tissue-specific *N*-glycosylation profiles of the most common EOC histotypes. The tissue sample set comprised of two different single sections of high-grade serous ovarian carcinoma tissue (referred to as HGSOC-1 and HGSOC-2) and four tissue microarray (TMA) sections, of which three consisted of tissue cores of less common EOC histotypes, i.e., low-grade serous ovarian carcinoma (LGSOC), clear cell carcinoma (OCC), endometrioid carcinoma (EC), whereas one contained tissue specimens of non-

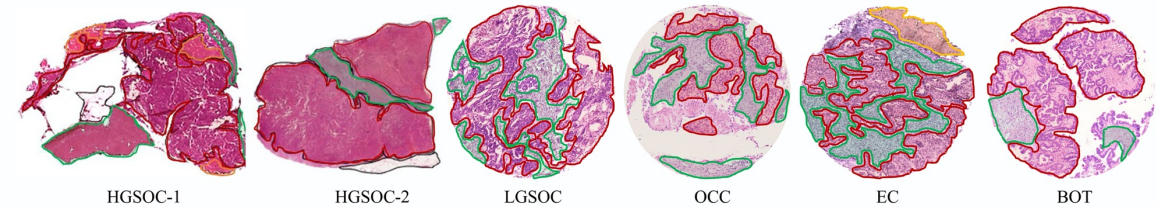

Figure 30. H&E stains of HGSOC whole tissue specimens and exemplary TMA tissue cores. Tumor regions are marked in red, non-tumor/tumor-stroma in green, and necrotic regions in yellow.

malignant borderline ovarian tumor (BOT). In parallel, to allow the identification of PNGase F-released *N*-glycans from contaminants, one consecutive HGSOC-2 tissue section was processed omitting the PNGase F digestion step and served as a negative control. Following the MALDI-MSI analysis, investigated tissues were stained with hematoxylin and eosin (H&E). Morphological regions, such as tumor, non-tumor/stroma, necrosis, and adipose tissue, were annotated by an experienced pathologist. Annotation of both HGSOC whole tissue sections and exemplary TMA cores of each investigated EOC histotype is shown in *Figure 30*.

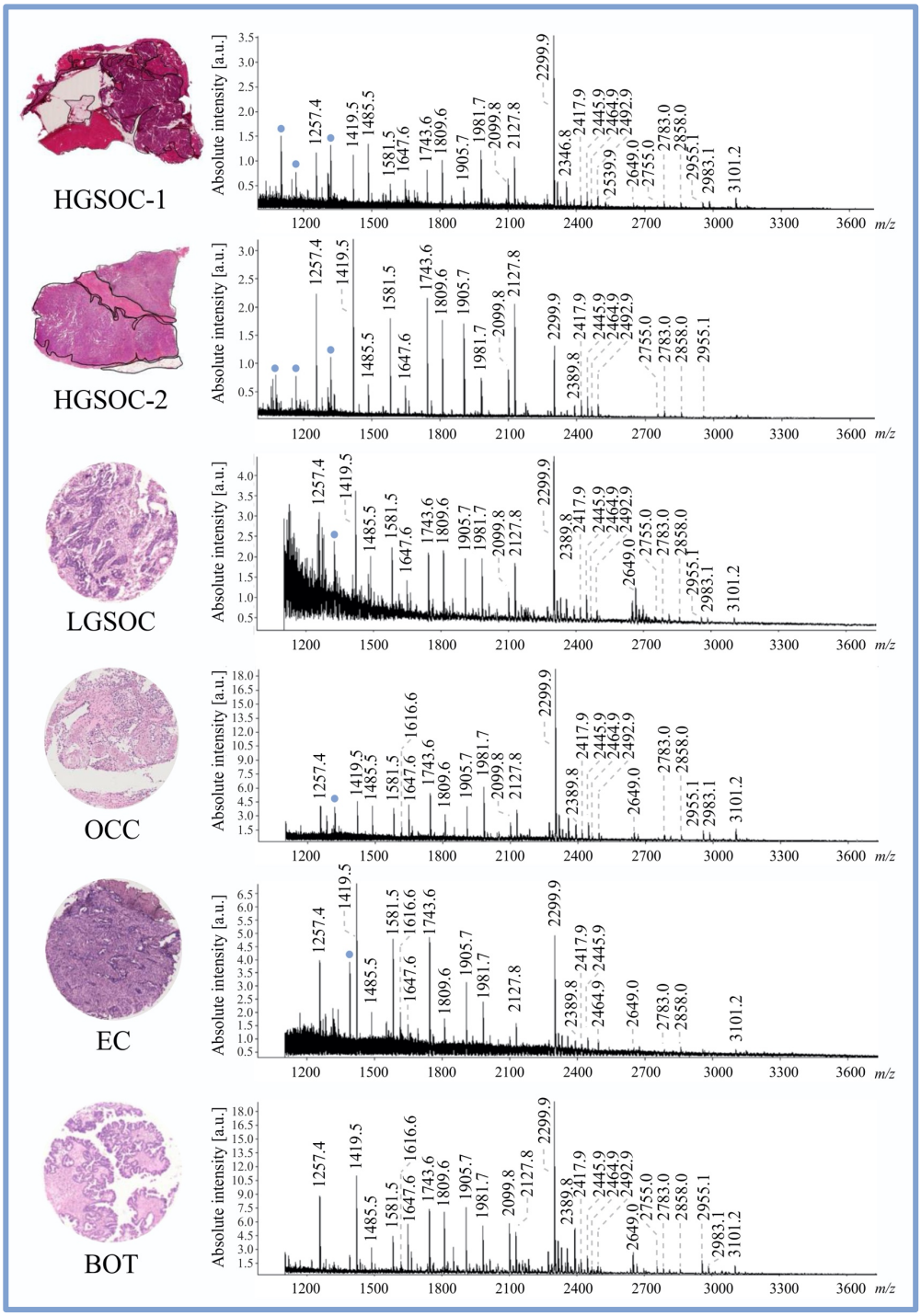

Figure 31. Average MALDI imaging mass spectra $[M+Na]^+$ of all investigated EOC tissue specimens. Schematic representations of indicated m/z species are shown in Table 10. For each TMA slide, only one representative tissue core is shown. Blue dots: non-carbohydrate contaminants.

A varying number of *N*-glycan structures was detected across all investigated EOC tissue specimens, with over 60 *N*-glycan species being detected in HGSOC-1 and less than 20 in EC-TMA tissue. Observed structures included high-mannose-, hybrid-, and complex-type neutral and sialylated *N*-glycans, frequently decorated with fucose residue. Although all investigated EOC tissues showed different average *N*-glycosylation profiles, in each case, recorded mass spectra were primarily dominated by *m/z* species corresponding to complex-type sialylated and high-mannose *N*-glycans. Importantly, due to implementation of chemical derivatization, the discrimination of α2,3- and α2,6-sialylated *N*-glycan species was possible, revealing the dominance of α2,6- over α2,3-sialylated *N*-glycans. Average mass spectra of all investigated EOC tissues are shown in *Figure 31*, whereas an overview of all detected *N*-glycan structures is shown in *Table 10*.

Table 10. N-Glycan structures detected by MALDI-MSI across all investigated EOC tissue specimens.

m/z $[M+Na]^+$			Single tissues			TMAs			
	Composition	Structure	Neg.	HGSOC-1	HGSOC-2	LGSOC	OCC	EC	BOT
1079.37	H3N2F1			✓	✓	n.d.	n.d.	n.d.	n.d.
1095.37	H4N2			✓	✓	n.d.	n.d.	n.d.	n.d.
1136.40	H3N3				✓				
1257.42	H5N2			✓	✓	✓	✓	✓	✓
1282.45	H3N3F1			✓	✓				
1298.45	H4N3	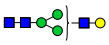			✓				
1339.48	H3N4				✓				
1419.48	H6N2			✓	✓	✓	✓	✓	✓
1444.51	H4N3F1	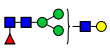		✓	✓				✓
1485.53	H3N4F1			✓	✓	✓	✓	✓	✓
1501.53	H4N4	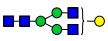		✓	✓	✓			✓
1581.53	H7N2			✓	✓	✓	✓	✓	✓
1616.60	H4N3D1	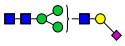		✓	✓		✓		✓
1647.59	H4N4F1	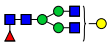		✓	✓	✓	✓		✓
1663.58	H5N4			✓	✓	✓	✓		✓
1688.61	H3N5F1			✓	✓				✓
1704.61	H4N5	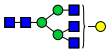		✓					✓
1743.58	H8N2			✓	✓	✓	✓	✓	✓
1762.65	H4N3F1D1	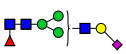		✓	✓				✓

Table 10. Continued.

m/z [M+Na]$^+$			Single tissues			TMAs			
	Composition	Structure	Neg.	HGSOC-1	HGSOC-2	LGSOC	OCC	EC	BOT
1778.64	H5N3D1	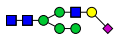		✓					✓
1809.64	H5N4F1	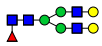		✓	✓	✓	✓	✓	✓
1819.68	H4N4D1			✓					✓
1825.63	H6N4	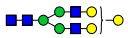		✓					✓
1850.67	H4N5F1	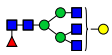		✓	✓	✓	✓		✓
1866.66	H5N5	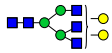		✓					✓
1891.69	H3N6F1			✓					
1905.63	H9N2	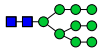		✓	✓	✓	✓	✓	✓
1937.70	H4N4F1A1			✓					
1953.70	H5N4A1	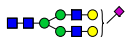		✓	✓		✓		✓
1965.73	H4N4F1D1	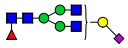		✓	✓	✓			✓
1981.73	H5N4D1	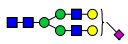		✓	✓	✓	✓	✓	✓
2012.72	H5N5F1	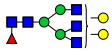		✓	✓	✓	✓	✓	✓
2028.71	H6N5	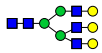		✓					✓
2053.75	H4N6F1	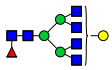		✓					
2099.76	H5N4F1A1	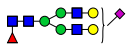		✓	✓	✓	✓	✓	✓
2127.79	H5N4F1D1	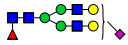		✓	✓	✓	✓	✓	✓
2168.82	H4N5F1D1	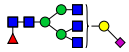		✓	✓	✓			✓
2174.77	H6N5F1	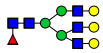		✓	✓	✓			✓
2184.80	H5N5D1	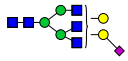		✓	✓	✓	✓		✓
2243.81	H5N4A2			✓					✓
2271.85	H5N4A1D1	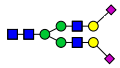		✓	✓	✓	✓		✓
2299.88	H5N4D2	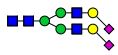		✓	✓	✓	✓	✓	✓
2330.87	H5N5F1D1	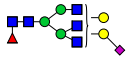		✓	✓	✓	✓	✓	✓
2346.86	H6N5D1	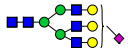		✓	✓	✓	✓		✓
2389.88	H5N4F1A2	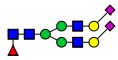		✓	✓	✓	✓	✓	✓
2417.91	H5N4F1A1D1			✓	✓	✓	✓		✓

Table 10. Continued.

m/z [M+Na]$^+$			Single tissues			TMAs			
	Composition	Structure	Neg.	HGSOC-1	HGSOC-2	LGSOC	OCC	EC	BOT
2445.94	H5N4F1D2			✓	✓	✓	✓	✓	✓
2464.89	H6N5F1A1	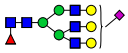		✓	✓	✓	✓		✓
2492.91	H6N5F1D1	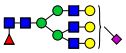		✓	✓	✓	✓	✓	✓
2502.95	H5N5D2	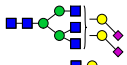		✓	✓	✓	✓		✓
2539.90	H7N6F1	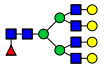		✓	✓				
2636.97	H6N5A1D1	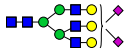		✓	✓		✓		✓
2649.00	H5N5F1D2	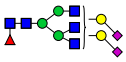		✓		✓	✓		✓
2665.00	H6N5D2	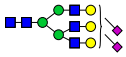		✓			✓		✓
2696.00	H6N6F1D1	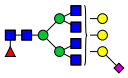				✓	✓		✓
2755.00	H6N5F1A2	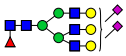		✓	✓		✓		✓
2783.03	H6N5F1A1D1	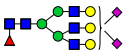		✓	✓	✓	✓		✓
2811.06	H6N5F1D2	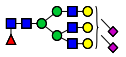		✓	✓	✓	✓		✓
2830.01	H7N6F1A1	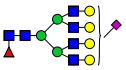		✓	✓				
2858.05	H7N6F1D1	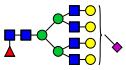		✓	✓	✓	✓	✓	✓
2955.11	H6N5A1D2	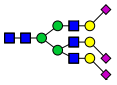		✓	✓	✓	✓		✓
2983.14	H6N5D3	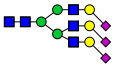		✓		✓	✓		✓
3045.12	H6N5F1A3	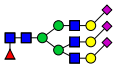		✓	✓		✓		✓
3073.14	H6N5F1A2D1	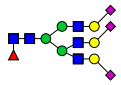		✓	✓		✓		✓
3101.17	H6N5F1A1D2	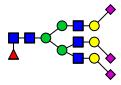		✓	✓	✓	✓	✓	✓
3148.16	H7N6F1A1D1	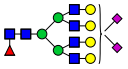		✓	✓		✓		✓
3158.19	H6N6A1D2	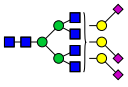		✓			✓		✓

Neg. – negative control; n.d. – no data; ✓ – detected peak.

Spatial N-glycan distribution in HGSOC whole tissue sections

As visible in *Figure 32* and *Figure 33,* the spatial distribution of *N*-glycan structures matched morphological features of investigated HGSOC tissues. Precisely, high-mannose *N*-glycans, i.e., H5N2 at *m/z* 1257.4, H6N2 at *m/z* 1419.5, H7N2 at *m/z* 1581.5, H8N2 at *m/z* 1743.6, and H9N2

at *m/z* 1905.6, were detected in tumor areas of both investigated HGSOC whole tissue sections, which is in line with the results of Everest-Dass et al. [200]. Contrarily, complex-type neutral structures, such as H3N4F1 at *m/z* 1485.5, H4N4F1 at *m/z* 1647.6, H5N4 at *m/z* 1663.6, H5N4F1 at *m/z* 1809.6, and H6N5F1 at *m/z* 2174.8, were more abundant in non-tumor regions and, as observed for H3N4 at *m/z* 1339.5, H4N5F1 at *m/z* 1850.7, and H5N5F1 at *m/z* 2012.7, in adipose-rich areas. Most importantly, α2,3- and α2,6-sialylated *N*-glycan structures showed very distinct distribution in both investigated HGSOC tissues. Precisely, as observed in HGSOC-1 tissue, the distribution of α2,6-sialylated structures, including mono-α2,6-sialylated H5N4D1 at *m/z* 1981.7 and H5N5F1D1 at *m/z* 2330.9, di-α2,6-sialylated H5N4D2 at *m/z* 2299.9, H5N4F1D2 at *m/z* 2445.9,

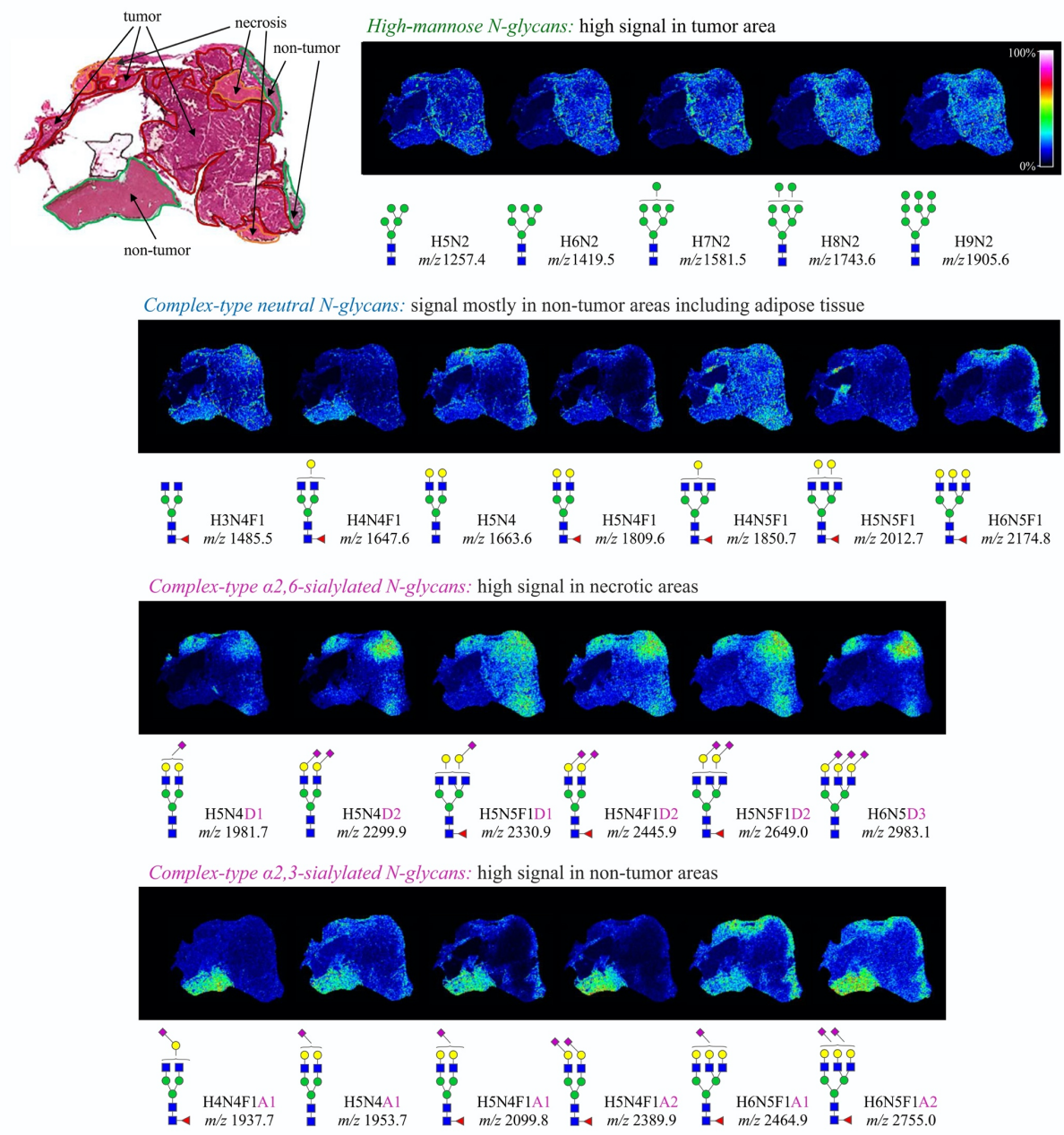

Figure 32. Spatial distribution of exemplary N-glycan structures in HGSOC-1 tissue section as determined by MALDI-MSI.

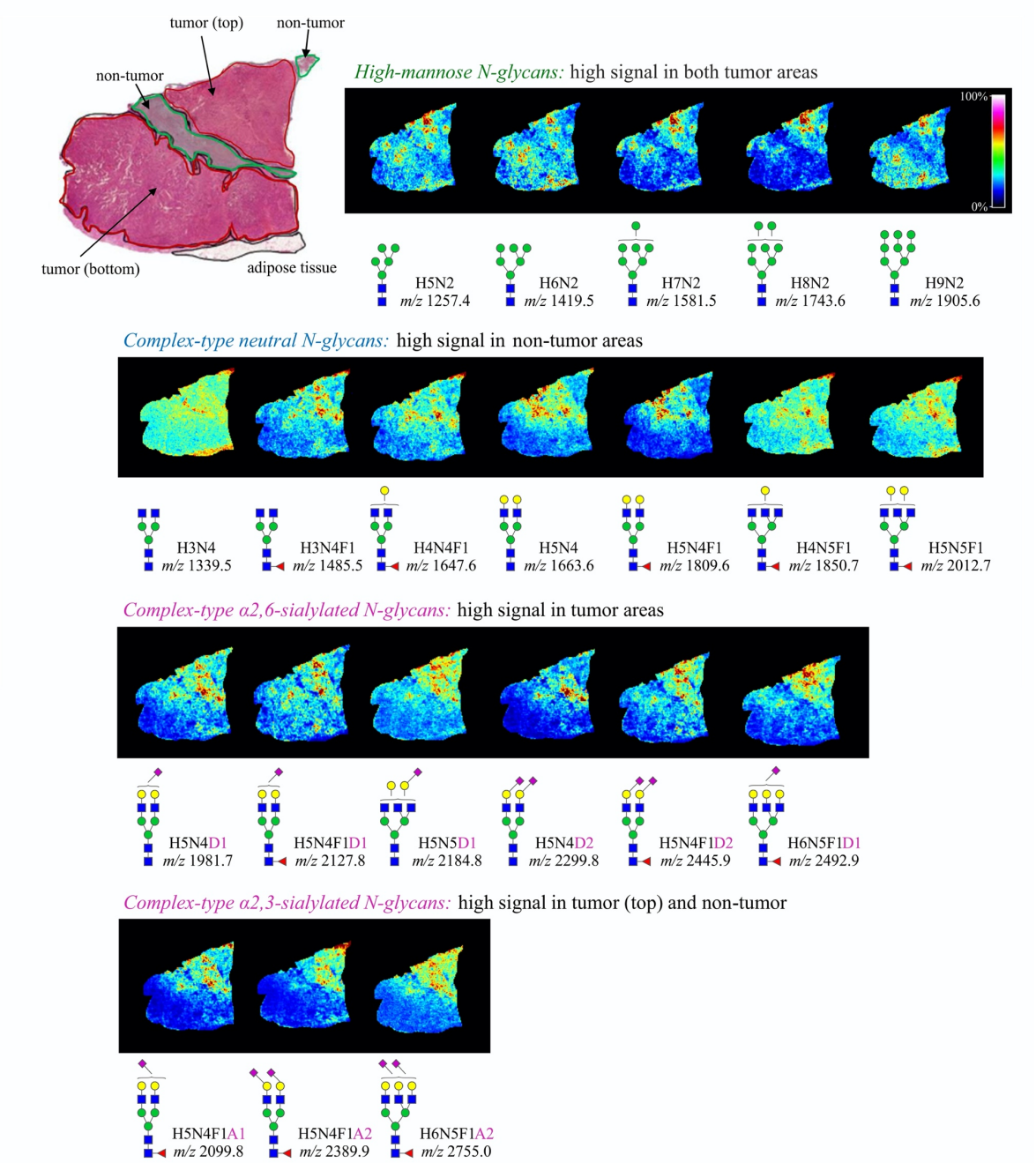

Figure 33. Spatial distribution of exemplary N-glycan structures in HGSOC-2 tissue section as determined by MALDI-MSI.

H5N5F1D2 at *m/z* 2649.0, and tri-α2,6-sialylated H6N5D3 at 2983.1, showed strong co-localization with necrotic regions. In HGSOC-2 tissue specimen, which lacks necrotic cores, α2,6-sialylated *N*-glycan structures were predominantly observed in tumor (top) region and, to a lesser degree, in tumor (down) region. On the opposite, α2,3-sialylated structures, such as mono-α2,3-sialylated H4N4F1A1 at *m/z* 1937.7, H5N4A1 at *m/z* 1953.7, H5N4F1A1 at *m/z* 2099.8, H6N5F1A1 at *m/z* 2464.9, and di-α2,3-sialylated H5N4F1A2 at *m/z* 2389.9 and H6N5F1A2 at *m/z* 2755.0, were predominantly observed in non-tumor areas (in HGSOC-1) or non-tumor and tumor areas (in HGSOC-2).

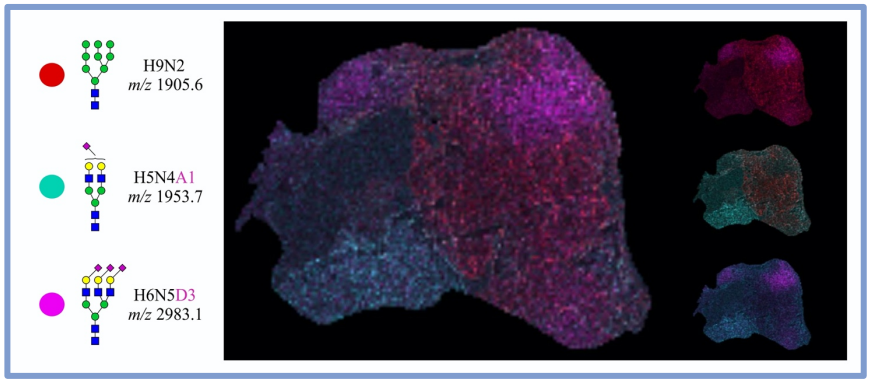

Figure 34. An overlay image of the three N-glycan structures showing distinct tissue type-specific distribution. The high-mannose H9N2 is primarily detected in tumor, the α2,3-sialylated H5N4A1 in non-tumor, whereas the α2,6-sialylated H6N5D3 in necrotic regions of HGSOC-1 tissue specimen.

As visualized for HGSOC-1 tissue in *Figure 34* with H9N2 at *m/z* 1905.6, H5N4A1 at *m/z* 1953.7, and H6N5D3 at *m/z* 2983.1, *in situ*-released *N*-glycans were able to differentiate three distinct morphological tissue regions, i.e., tumor, necrosis, and non-tumor. Notably, receiver operating characteristic (ROC) curves were built for the different *N*-glycan structures, further confirming their potential to serve as tissue type-specific discriminators. The ROC plots of the above-mentioned H9N2, H5N4A1, and H6N5D3 *N*-glycan structures are presented in *Figure 35*, whereas area under the curve (AUC) values for *N*-glycans exhibiting the highest discriminatory potential as determined by tumor vs. non-tumor, tumor vs. necrosis, necrosis vs. non-tumor, non-tumor vs. tumor, necrosis vs. tumor, and non-tumor vs. necrosis analyses, are shown in *Table 11*.

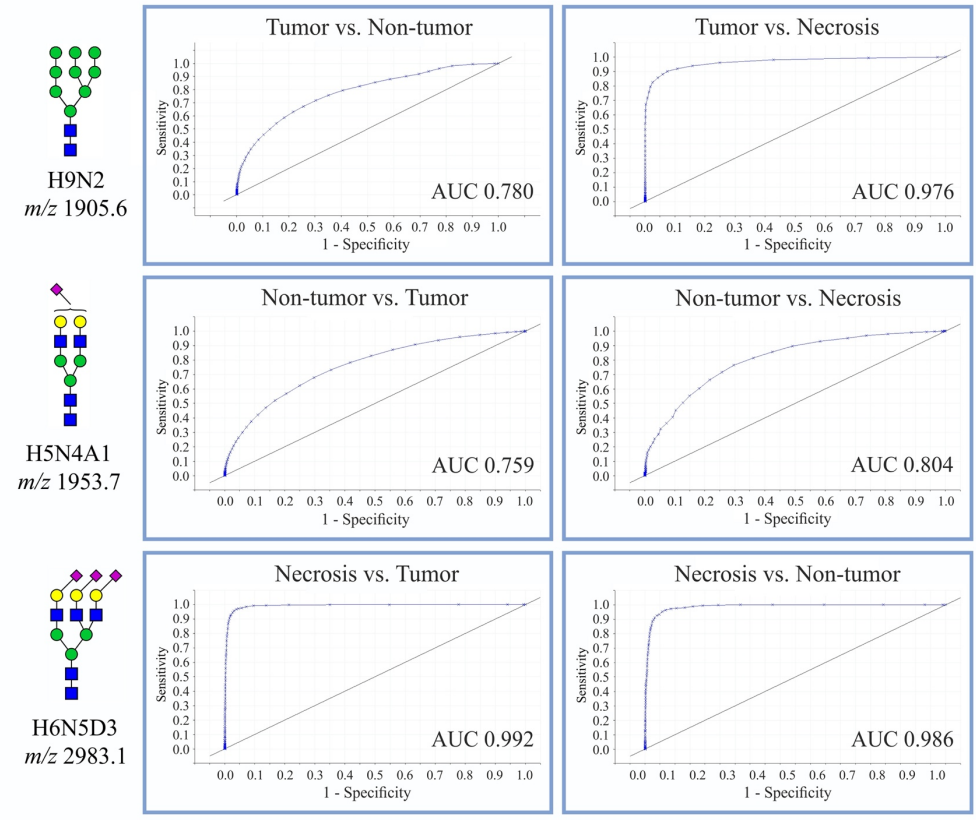

Figure 35. ROC curves of the three most discriminatory N-glycan structures as determined for tumor, non-tumor, and necrotic tissue areas of both investigated HGSOC tissue specimens.

Table 11. The five most discriminative N-glycan structures as determined by ROC curve analysis of tumor vs. non-tumor, tumor vs. necrosis, necrosis vs. non-tumor, non-tumor vs. tumor, necrosis vs. tumor, and non-tumor vs. necrosis regions of both HGSOC tissues.

Tumor vs. Non-tumor			Tumor vs. Necrosis			Necrosis vs. Non-tumor		
m/z	Composition	AUC	*m/z*	Composition	AUC	*m/z*	Composition	AUC
1905.6	H9N2	0.780	1905.6	H9N2	0.976	3101.2	H6N5F1A1D2	0.986
1743.6	H8N2	0.772	1743.6	H8N2	0.973	2983.1	H6N5D3	0.985
1762.7	H4N3F1D1	0.745	1581.5	H7N2	0.960	2299.8	H5N4D2	0.980
1581.5	H7N2	0.729	1419.5	H6N2	0.960	2955.1	H6N5A1D2	0.980
1419.5	H6N2	0.713	1257.4	H5N2	0.825	2649.0	H5N5F1D2	0.971

Non-tumor vs. Tumor			Necrosis vs. Tumor			Non-tumor vs. Necrosis		
m/z	Composition	AUC	*m/z*	Composition	AUC	*m/z*	Composition	AUC
1953.7	H5N4A1	0.759	2983.1	H6N5D3	0.992	2099.8	H5N4F1A1	0.979
1663.6	H5N4	0.746	3101.2	H6N5F1A1D2	0.991	1809.6	H5N4F1	0.956
2464.9	H6N5F1A1	0.741	2299.9	H5N4D2	0.987	2389.9	H5N4F1A2	0.944
2099.8	H5N4F1A1	0.739	2955.1	H6N5A1D2	0.986	2755.0	H6N5F1A2	0.881
1647.6	H4N4F1	0.726	2271.8	H5N4A1D1	0.971	1444.5	H4N3F1	0.868

ROC curves showed that the high-mannose *N*-glycans H9N2 (*m/z* 1905.6), H8N2 (*m/z* 1743.6), H7N2 (*m/z* 1581.5), and H6N2 (*m/z* 1419.5) were fairly good discriminants (AUC between 0.7 and 0.8) of HGSOC tumors, as determined by comparing tumor with non-tumor tissue regions, and excellent discriminants (AUC between 0.95 and 1) of HGSOC tumors when comparing tumor and necrotic regions (*Table 11*). Contrarily, α2,3-sialylated structures, such as H5N4A1 (*m/z* 1953.7), H6N5F1A1 (*m/z* 2465.9), and H5N4F1A1 (*m/z* 2099.8), together with the complex-type neutral structures H5N4 (*m/z* 1663.6) and H4N4F1 (*m/z* 1647.6), decreased in tumor areas and displayed fairly good discriminative potential (AUC between 0.7 and 0.8) when comparing non-tumor with tumor tissue regions (*Table 11*). In turn, the α2,6-sialylated structures H6N5D3 (*m/z* 2983.1) and H5N4D2 (*m/z* 2299.9) increased in necrotic areas as shown from their excellent discriminative potential (AUC values between 0.95 and 1) when comparing necrotic and tumor tissue areas. Notably, equally excellent performances were obtained for *N*-glycans carrying both α2,6- and α2,3-sialic acids, namely H6N5F1A1D2 (*m/z* 3101.2), H6N5A1D2 (*m/z* 2955.1), and H5N4A1D1 (*m/z* 2271.8). Consistently, as can be seen in the right upper panel of *Table 11*, the ROC analysis of necrotic vs. non-tumor regions of HGSOC tissues indicated α2,6-sialylated (H6N5D3 at *m/z* 2983.1, H5N4D2 at *m/z* 2299.8, and H5N5F1D2 at *m/z* 2649.0) and α2,3/α2,6-sialylated *N*-glycans (H6N5F1A1D2 at *m/z* 3101.2, H6N5A1D2 at *m/z* 2955.1) as excellent discriminants (AUC between 0.95 and 1). Contrarily, the ROC analysis of non-tumor vs. necrotic regions indicated the α2,3-sialylated *N*-glycan H5N4F1A1 (*m/z* 2099.8) and the complex-type neutral *N*-glycan H5N4F1 (*m/z* 1809.6) as excellent discriminants (AUC between 0.95 and 1) of non-tumor regions of HGSOC tissues.

Spatial N-glycan distribution in other EOC histotype TMA sections

In order to determine whether the tissue type-specific *N*-glycan distribution observed in HGSOC was also valid for less aggressive EOC histotypes and non-malignant ovarian disease, the following MALDI-MSI experiments were performed using tissue specimens of LGSOC, OCC, EC, and BOT patients. Additionally, to allow simultaneous analysis of multiple tissues, the above tissue specimens were investigated in TMA format.

As compared to whole tissue slides, the use of TMA material allows the simultaneous analysis of tens to hundreds of patients' tissue samples, significantly improving the throughput. However, due to their small size, TMA cores are prone to damage and detachment in the course of analysis. In this experiment, significant TMA core loss was observed as a result of high-temperature treatments, in particular antigen retrieval and sialic acid derivatization steps. For the final analysis, only well-preserved TMA cores were included, resulting in six cores of LGSOC and OCC and seven cores of EC and BOT. The H&E stains of all included in the analysis TMA cores are shown in *Figure 36*.

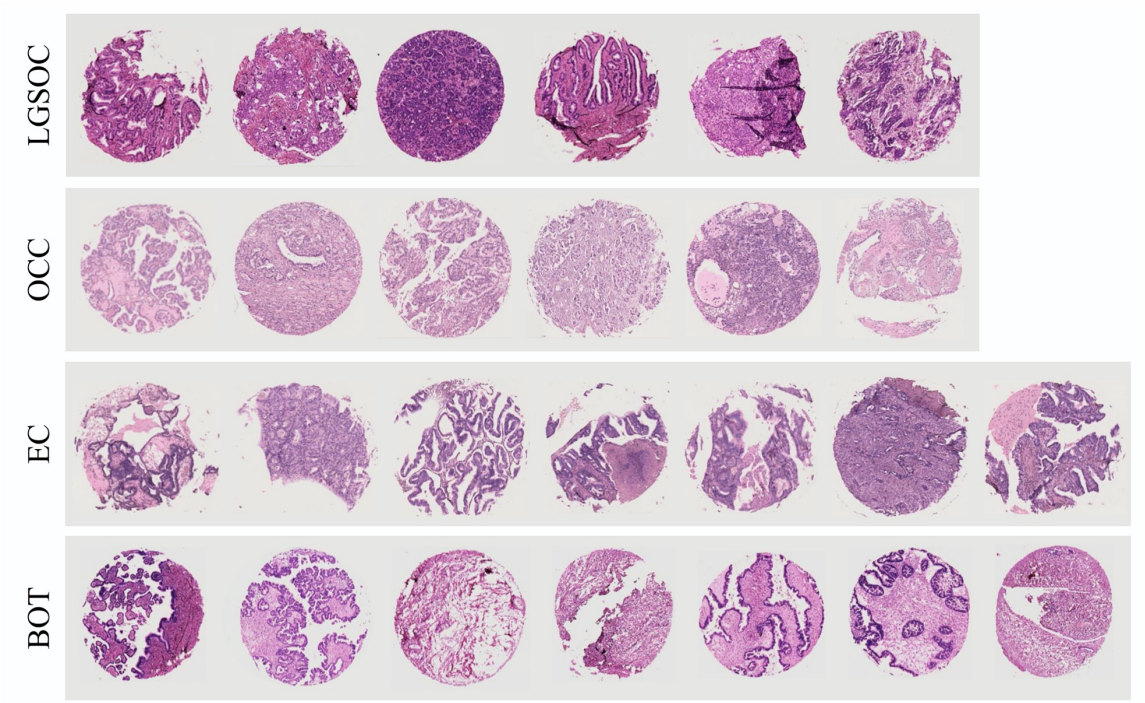

Figure 36. H&E stains of TMA cores included in the MALDI-MSI analysis.

It should be noted that, since all TMA cores were originally extracted from tumor-containing regions of donor FFPE tissue specimens, annotation of non-tumor areas within investigated tissue cores was technically impossible. For this reason, in this experiment, investigated tissue regions were differentiated into tumor and tumor-stroma. The latter category encompassed tumor-surrounding areas, which contained distinctly less tumor cells as compared to solid tumor regions although they were not entirely tumor-free. The annotation of tumor and tumor-stroma regions in exemplary TMA cores is shown in *Figure 30*.

Table 12. The most discriminative N-glycan structures as determined by ROC curve analyses of tumor vs. tumor-stroma regions of LGSOC, OCC, EC, and BOT tissues.

Tumor vs. Tumor-Stroma												
LGSOC			OCC			EC			BOT			
m/z	Composition	AUC	*m/z*	Composition	AUC	*m/z*	Composition	AUC	*m/z*	Composition	AUC
2330.9	*H5N5F1D1*	*0.648*	1743.6	H8N2	0.658	1981.7	H5N4D1	0.740	2330.9	H5N5F1D1	0.806
2649.0	*H5N5F1D2*	*0.628*				2330.9	H5N5F1D1	0.735	2649.0	H5N5F1D2	0.775
						2445.9	H5N4F1D2	0.728	1905.6	H9N2	0.759
						2127.8	H5N4F1D1	0.727	1419.5	H6N2	0.758
						1647.6	H4N4F1	0.722	2346.9	H6N5D1	0.732
						2492.9	H6N5F1D1	0.682	2696.0	H6N6F1D1	0.724
						1419.5	H6N2	0.670	1581.5	H7N2	0.719
						1581.5	H7N2	0.667	3101.2	H6N5F1A1D2	0.700

- *only N-glycan structures with AUC > 0.60 are shown*
- *for EC and BOT, only eight N-glycan structures with the highest AUC values are shown*
- *N-glycan structures with AUC >0.600 but < 0.649 are indicated in italics*

ROC curves comparing tumor vs. tumor-stroma regions were generated separately for each EOC histotype and BOT specimen, the results of which are shown in *Table 12*. Although in OCC, EC, and BOT some *N*-glycan structures did show discriminatory potential (AUC > 0.65), the AUC values were overall lower than those observed for the tumor vs. non-tumor analysis in HGSOC whole tissue specimen. In LGSOC, no *N*-glycan structure displayed AUC > 0.65.

Notably, as revealed by the tumor vs. tumor-stroma ROC curve analysis, in all investigated EOC histotypes, the best discrimination of tumor regions was achieved with α2,6-sialylated complex-type and high-mannose *N*-glycans, which is in line with the results of HGSOC whole tissue section analysis. Precisely, in LGSOC, the highest AUC values were observed for H5N5F1D1 at *m/z* 2330.9 and H5N5F1D2 at *m/z* 2649.0. Nevertheless, as their respective AUC values of 0.648 and 0.628 were below the predetermined threshold of 0.65, none of these glycans performed good enough to qualify as potential discriminant of LGSOC tumor tissue. In the case of OCC, AUC > 0.65 was observed only for the high-mannose *N*-glycan H8N2 (*m/z* 1743.6), which qualified as poor discriminant of OCC tumor regions (AUC: 0.658). Contrarily, in EC, eight *N*-glycans showed AUC > 0.65, of which five structures (H5N4D1 at *m/z* 1981.7, H5N5F1D1 at *m/z* 2330.9, H5N4F1D2 at *m/z* 2445.9, H5N4F1D1 at *m/z* 2127.8, and H4N4F1 at *m/z* 1647.6) displayed fairly good discriminative potential (AUC between 0.7 and 0.8).

Interestingly, the best results of the tumor vs. tumor-stroma ROC curve analysis were observed for BOT-TMA specimen. Consistently with all investigated EOC histotypes, the best discriminators of BOT tumor tissue were α2,6-sialylated complex- and high-mannose-type *N*-glycans. Among α2,6-sialylated glycans, the H5N5F1D1 structure at *m/z* 2330.9 showed good discriminative potential (AUC 0.806), whereas H5N5F1D2 at *m/z* 2649.0, H6N5D1 at *m/z* 2346.9, and H6N6F1D1 at *m/z* 2696.0 displayed fairly good discriminative potential.

Table 13. The most discriminative N-glycan structures as determined by ROC curve analysis of tumor-stroma vs. tumor regions of LGSOC, OCC, EC, and BOT tissues.

Tumor-Stroma vs. Tumor												
LGSOC			OCC			EC			BOT			
m/z	Composition	AUC	*m/z*	Composition	AUC	*m/z*	Composition	AUC	*m/z*	Composition	AUC
			2099.8	H5N4F1A1	0.901	2389.9	H5N4F1A2	0.757	2099.8	H5N4F1A1	0.743
			1953.7	H5N4A1	0.825	2099.8	H5N4A1	0.734	1809.6	H5N4F1	0.670
			1981.7	H5N4D1	0.822	*2755.0*	*H6N5F1A2*	*0.607*	2012.7	H5N5F1	0.662
			2955.1	H6N5A1D2	0.815				*1825.6*	*H6N4*	*0.616*
			2665.0	H6N5D2	0.774				*1953.7*	*H5N4A1*	*0.602*

- *only N-glycan structures with AUC > 0.60 are shown*
- *for OCC, only five N-glycan structures with the highest AUC values are shown*
- *N-glycan structures with AUC > 0.600 and < 0.649 are indicated in italics*

Similarly good results were achieved for high-mannose *N*-glycans, such as H9N2 at *m/z* 1905.6, H6N2 at *m/z* 1419.5, and H7N2 at *m/z* 1581.5. Likewise, the ROC curve analysis of tumor-stroma vs. tumor regions of LGSOC, OCC, EC, and BOT tissue revealed glycan patterns similar to those

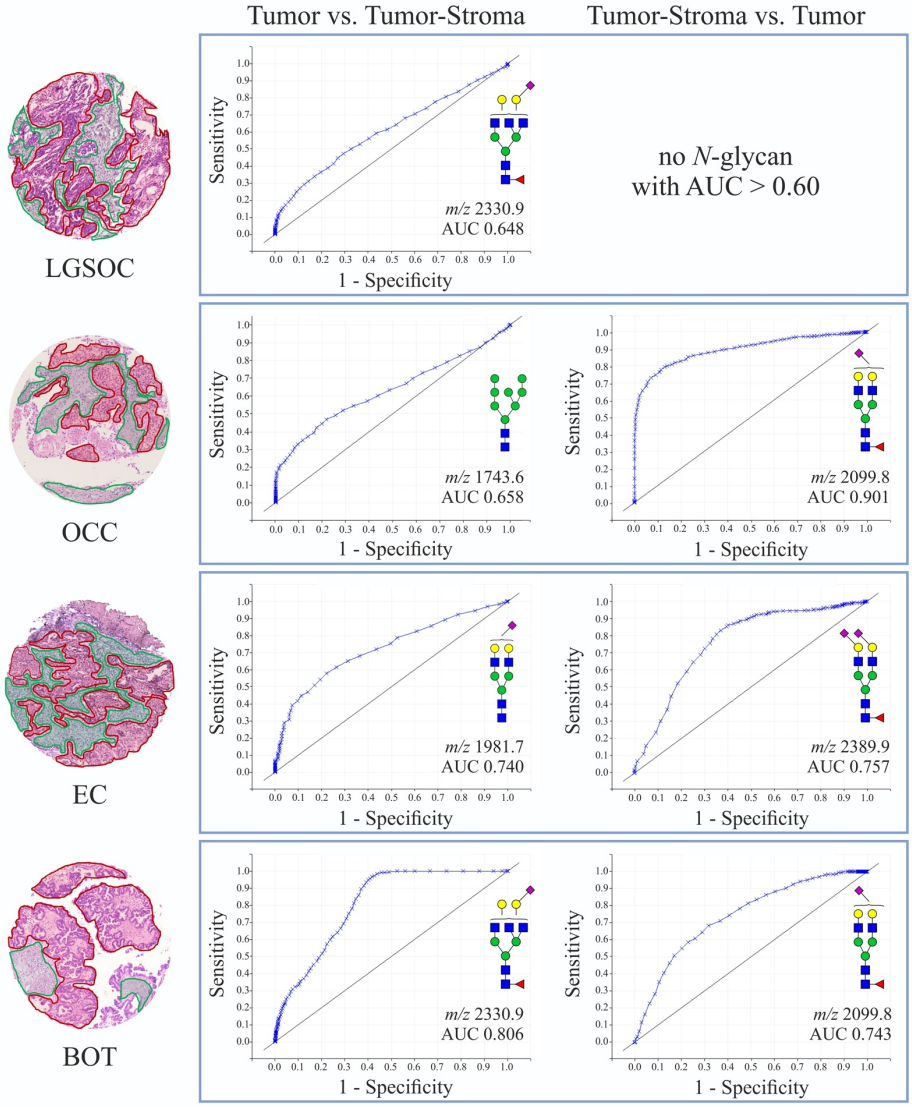

Figure 37. ROC curves of the most discriminatory N-glycan structures as determined for tumor and tumor-stroma in LGSOC, OCC, EC, and BOT TMA specimens. Only exemplary tissue cores are shown. Tumor regions are marked in red, whereas tumor-stroma is marked in green.

observed previously in HGSOC tissues. As can be seen in *Table 13*, in OCC, EC, and BOT, the best performance in discriminating between tumor-stroma and tumor regions was achieved for α2,3-sialylated *N*-glycans. Above all, H5N4F1A1 at *m/z* 2099.8 was revealed a very good discriminant (AUC 0.901) of tumor-stroma in OCC and a fairly good in EC and BOT specimens. In the case of LGSOC, no *N*-glycan structure showed discriminative potential as determined by ROC curve analysis of tumor-stroma vs. tumor regions. The ROC curves and the AUC values of the most discriminative *N*-glycan structures across all investigated TMA specimens (tumor vs. tumor-stroma and tumor-stroma vs. tumor) are shown in *Figure 37*.

5. Discussion

Aiming at deepening the understanding of OC-related *N*-glycosylation changes, in this study, the analysis of enzymatically released *N*-glycans was executed directly on-tissue, implementing the novel and fast-evolving MALDI-MSI technique.

The current knowledge on OC-related *N*-glycosylation changes has predominantly been gained from studies on glycoproteins contained in body fluids using serum/plasma/blood or ascites as starting material [47, 152, 207-210]. Throughout the years, this approach revealed a number of *N*-glycosylation alteration patterns, holding the potential for improving OC diagnosis, monitoring, and treatment. Nevertheless, as glycoproteins and *N*-glycans shed from tumor lesion represent only a minute fraction of all molecules contained in body fluids, glycosylation changes determined at the level of total serum/plasma/blood primarily reflect the systemic response of the host to the tumor, rather than tumor glycosylation profile itself.

Until recently, the visualization of *N*-glycans and other carbohydrates within tissues was only possible with the help of specific carbohydrate-binding proteins, e.g., lectins and anti-carbohydrate antibodies [211]. As far as this methodology is routinely applied in the clinic (e.g., measurement of CA 19-9 in the prognosis of pancreatic cancer [212]), anti-carbohydrate antibody- and lectin-based visualization is a highly targeted approach, in which investigated epitopes must be known and defined prior to the analysis. Additionally, as both lectins and anti-carbohydrate antibodies recognize structural carbohydrate motifs composed of 1-4 monosaccharides, they lack specificity toward glycan class and carrier. As such, their use does not allow determining whether detected glycans stem from glycolipids or *N*- or *O*-linked glycoproteins [213].

Importantly, the above-described limitations can be readily circumvented by using MALDI-MSI, a cutting-edge imaging technique that combines the high sensitivity of mass spectrometry with spatial distribution information, typical of immuno-histochemistry stainings. Following its successful employment in proteomics, lipidomics, and metabolomics [214-216], MALDI-MSI slowly paved its way to glycomics, where it is being used in an increasing number of applications, with tumor tissue analysis ranking high on the list. Besides colon, hepatic, and prostate cancer [113,

199, 217], MALDI-MSI has been employed to investigate *in situ N*-glycosylation in OC [200, 203], which despite decades of research remains the most lethal gynecological malignancy in women.

While previous studies provided solid information regarding the distribution of high-mannose and complex-type neutral *N*-glycans in OC tissue, the available data regarding sialylated *N*-glycans was very limited. Notably, this lack of data was predominantly due to the poor detection of non-derivatized sialylated structures in MALDI-TOF-MS operated in positive ionization mode. Hence, to fill the above-described gap, in this study, epithelial OC (EOC) tissue-specific *N*-glycosylation analysis was further expanded by introducing linkage-specific sialic acid derivatization [113], which not only significantly improved MALDI-MSI detection of sialylated *N*-glycans but also enabled the discrimination of their α2,3- and α2,6-linkage to subterminal galactoses. As demonstrated for HGSOC tissue specimens, implementation of this chemical derivatization was of pivotal importance, as it allowed revealing distinctive spatial distributions of α2,3- and α2,6-sialylated *N*-glycans that were strongly associated with EOC tissue morphology. Specifically, the results of this work demonstrated that, apart from high-mannose *N*-glycans described in previous studies [200, 203], tumor and in particular tumor-associated necrotic regions of EOC tissues are marked by a high abundance of complex-type α2,6-sialylated *N*-glycans. In fact, the biantennary bi-α2,6-sialylated H5N4D2 structure represented one of the most abundant *N*-glycan structures in all investigated EOC tissues. In turn, adjacent non-tumor/stroma regions were observed to be enriched in complex-type α2,3-sialylated and neutral *N*-glycans. Importantly, statistical analyses revealed a collection of *N*-glycans holding the potential to serve as markers of distinct EOC tissue regions. Among these, α2,6-sialylated H5N5F1D1 as well as high-mannose H9N2 and H8N2 *N*-glycan structures performed particularly well as discriminants of tumor regions, whereas α2,3-sialylated H5N4A1 and H5N4F1A1 structures showed a great performance at discriminating non-tumor/stroma from tumor/tumor-related necrotic regions.

Importantly, the tissue type-specific *N*-glycan distribution, described above for HGSOC specimens, was also observed in less aggressive EOC histotypes and BOT tissue, however with a weaker statistical significance. It is plausible that the better discriminating performance of *N*-glycans in HGSOCs, as compared to LGSOC, OCC, EOC, and BOT tissues, is due to the use of single whole tissue specimens instead of TMA material. In fact, the small size of TMA cores, together with the limited resolution of the measuring device and high heterogeneity of pathologically altered tissue, hinders the generation of high-accuracy ion images that are essential for reliable statistical analysis. Nevertheless, since trends observed in HGSOC whole tissue specimens were to a considerable extend replicated in investigated TMA slides, the utility of TMA technology in *N*-glycan imaging studies should be further examined, as it provides a gateway to high-throughput analyses.

Interestingly, the results of this work are partly in contradiction with the findings of Briggs et al. [203], who showed that sialylated *N*-glycans represent only a minor fraction of all detected in OC

tissue structures, whereas complex-type neutral *N*-glycans are predominantly localized to its tumor regions. However, since in the above-mentioned study highly labile sialic acid residues were not stabilized/neutralized prior to MALDI-MSI analysis, this inconsistency might be caused by an overestimation of complex-type neutral *N*-glycan signals as a result of the degradation of their sialylated counterparts. This adverse effect has already been described by Holst et al. [113], who established the linkage-specific sialic acid derivatization reaction employed in this study.

At the same time, the results of this work are mostly in agreement with data reported by Anugraham et al. [218], who investigated membrane *N*-glycosylation in two non-cancerous (HOSE 6.3, HOSE 17.1) and four cancerous ovarian cell lines (SKOV3, IGROV1, A2780, OVCAR3) using PGC-LC-ESI-MS/MS. Specifically, Anugraham et al. demonstrated that high-mannose *N*-glycans are more abundant in cancerous cell lines, whereas complex-type neutral structures are higher in non-cancerous cells. Furthermore, by implementing α2,3-sialidase treatment, Anugraham et al. demonstrated that, in terms of sialylation, membranes of cancerous ovarian cells are predominantly decorated with α2,6-sialylated *N*-glycans, with many structures being observed exclusively in cancer cells. The latter results were further confirmed at the genetic level, as only cancerous cell lines showed high expression of ST6GAL1, a gene encoding for sialyltransferase catalyzing the addition of α2,6-linked sialic acids. Besides increased high-mannosylation and the prevalence of α2,6-sialylation, OC cell line-specific *N*-glycosylation profiles were shown to be marked by the presence of specific bisecting and LacdiNAc-type *N*-glycans, with the latter representing less than 1% of total relative ion intensities. Since, as opposed to PGC-LC-ESI-MS/MS, the MALDI-MSI device implemented in this work did not allow the enrichment and fragmentation of *in situ* detected analytes, the presence and distribution of these low abundant *N*-glycan species could not be validated in investigated EOC tissues. Nevertheless, since the results of Anugraham and coworkers are largely in line with presented MALDI-MSI data, OC cell lines seem to represent a quite reliable *in vitro* model of OC tissue-specific *N*-glycosylation.

It is important to note that EOC tissue-specific *N*-glycosylation profiles, marked by high-mannosylation and α2,6-sialylation, might have important functional and clinical implications. For instance, as shown by Parks et al. [219], in cholangiocarcinoma (CCA), an epithelial neoplasm of bile ducts, the elevation of extended high-mannose *N*-glycans (i.e., H7N2, H8N2, H9N2) on the surface of cancer cells was associated with their enhanced metastatic spread. Notably, an increased abundance of high-mannose structures in CCA cells was shown to result from the diminished expression of α-1,2-mannosidase-coding genes, mainly MAN1A1, whose protein product is responsible for trimming immature *N*-glycans prior to their processing to hybrid- and complex-type structures. In agreement with this data, forced overexpression of MAN1A1 in metastatic CCA cell lines hampered tumor growth *in vivo* [219]. Furthermore, it was demonstrated that the migratory and invasive capabilities of metastatic CCA cells can be compromised by masking extracellular α1,2-

mannosylation with mannose-binding lectin, ConA. It is however uncertain to what extend the above trend is valid for OC, as the analysis of over 200 surgical tissue specimens, performed by Hamester et al. [220], revealed that OC tissues are marked by increased (rather than decreased) expression of MAN1A1. Furthermore, high MAN1A1 levels were shown to be positively correlated with the advanced OC stage, the presence of distant metastasis, and shorter relapse-free survival. However, as the subsequent analysis of three OC cell lines, i.e., SKOV3, OVCAR8, and OAW42, revealed great variance in MAN1A1 expression level, it seems that the expression of the latter gene may be cell- and tissue type-specific. Hence, since tumor regions used in this study were marked by increased abundance of high-mannose *N*-glycans, further research should be done to more precisely define molecular backgrounds and regulations of this glycosylation feature in OC tissue. Additionally, as Hamester et al. [220] demonstrated that treatment with kifunensine, a potent mannosidase I inhibitor, increases the migration ability of OVCAR8 cells, it is essential to determine whether high-mannose structures decorating OC cell surface could serve as therapeutic targets to prevent tumor metastasis.

Besides increased abundance of high-mannose *N*-glycans, EOC tissues investigated in this work were characterized by particularly high α2,6-sialylation, which might likewise have major clinical implications. Hypersialylation has long been associated with enhanced cell survival and metastatic behavior, which effects are elicited by diverse molecular mechanisms. For instance, increased α2,6-sialylation of the Fas death receptor was shown to impair Fas-mediated apoptosis, allowing cancer cells to evade a major mechanism of programmed cell death [221]. Similarly, as demonstrated in colon cancer cells, an increase in terminal α2,6-sialylation on β1-integrins blocks their binding to extracellular galectin-3, inhibiting galectin-3-mediated apoptosis [222]. Of note, resistance to apoptosis is crucial for cancer cell survival and tumor progression, for which reason it is classified as a hallmark of cancer [223]. Interestingly, the above-described inhibition of galectin-3 binding was shown to occur specifically in the presence of α2,6- and not α2,3-sialylated oligosaccharides [224], which further emphasizes the necessity of linkage-specific examination of sialylated glycoforms in cancer tissues. Furthermore, as demonstrated in OV4 ovarian cancer cells that lack endogenous sialyltransferase activity, forced expression of ST6Gal-I resulted in α2,6-sialylation of β1-integrin that led to reduced cell-cell adherence and increased motility of affected cells [225]. A similar effect of forced ST6Gal-I expression was described in MDA-MB-435 breast carcinoma cells [226], which further confirms that increased α2,6-sialylation associates with an invasive phenotype. Additionally, Schultz et al. [88] showed that upregulated endogenous or forced expression of ST6Gal-I in OC cell lines is linked to cisplatin resistance. Significantly, the latter finding indicates that efficiency of OC treatment, which besides operative debulking typically consists of platinum-based chemotherapy, is, among other factors, dependent on cancer cells' sialylation status. In line with these findings, elevated expression of ST6Gal-I was shown to be correlated with poor prognosis in breast and colorectal cancer patients [91, 227].

The visualization of tissue-contained *N*-glycans highlighted another important issue that contributes to EOC disease complexity, namely tumor heterogeneity. In particular, this feature was visible in HGSOC-2 tissue specimens, in which two neighboring tumor regions of the same lesion exhibited different *N*-glycosylation patterns despite their very similar histopathological appearance. This intra-tumoral heterogeneity (ITH), manifested by varying abundance of some high-mannose, α2,3-, and α2,6-sialylated *N*-glycans, might reflect the coexistence of different cell populations within the tumor lesion. Importantly, ITH that arises from clonal expansion of individual cancer cells plays a crucial role in tumor metastasis, recurrence, and therapeutic resistance [228, 229]. Although there is little data available regarding glycosylation-based ITH in OC, in HCC tissue, expression of ST6Gal-I was shown to be up- or down-regulated within different groups of cells [92]. This heterogeneity was suggested to reflect an activation of different oncogenic pathways and varied cancer cell's differentiation stage, as lower ST6Gal-I expression was detected in less differentiated HCC specimens.

Certainly, understanding of the observed EOC tissue-specific *N*-glycosylation profile and its implications for OC progression and treatment could be greatly complemented by the identification of the corresponding tissue-contained glycan carrier proteins. Admittedly, consecutive slides of TMA specimens analyzed in this work constituted a part of the EOC tissue material investigated in the MALDI-MSI proteomic study, in which generated data were processed using various machine learning methods to discriminate histologic subtypes of EOC [230]. Nevertheless, the latter study specifically aimed at computing peptide-based EOC histotype-specific classifiers rather than determining spatial distribution of individual proteolytic peptides within investigated EOC tissues. For this reason, the co-registration of the *N*-glycome data generated in this study and the peptidomics data reported by Klein et al. [230] was not technically possible. Hence, further analyses are necessary in order to define protein carriers of tumor-contained high-mannose and α2,6-sialylated *N*-glycans as well as non-tumor/tumor-stroma-contained α2,3-sialylated *N*-glycans in OC tissue.

In summary, by reliably profiling the *in situ* spatial distribution of both neutral and sialylated *N*-glycan species, this study provides a valuable insight into molecular changes occurring directly within EOC tissue. Most importantly, the MALDI-MSI analysis allowed defining several tissue type-specific *N*-glycans that hold the potential to serve as discriminants of non-cancerous and pathologically altered ovarian cancer tissue regions. Nevertheless, as the data presented here was generated based on a small number of tissue specimens, the discriminatory potential of those pre-defined *N*-glycans should be confirmed in a larger cohort study. Finally, the results of this study highlight the importance of linkage-specific analysis of sialylated *N*-glycans and indicate that altered *N*-glycosylation should be considered as a factor contributing to intra- and inter-tumoral EOC heterogeneity.

Chapter V Final conclusion

Despite significant advances in its treatment, EOC persistently remains the most lethal gynecological malignancy in women. While molecular signatures of EOC disease have been broadly studied at the genetic and proteomic level, the EOC-related glycosylation alterations, which likewise significantly contribute to disease complexity, have not yet been investigated thoroughly. Interestingly, this is despite the fact that a majority of tumor diagnostic and prognostic markers, including the CA 125 marker, are glycoproteins or carbohydrate epitopes. Hence, by defining IgG subclass- and tissue-specific glycosylation alterations in blood serum and preserved biopsied tissue material, respectively, this study provided a valuable insight into the molecular changes occurring in the pathology of EOC.

The analysis of EOC patients' serum-derived IgG confirmed previous findings that changes in IgG glycosylation accompany the development and progression of EOC disease. Importantly, since altered glycosylation profiles were observed already at an early stage of the disease, IgG glycosylation showed the potential to serve as a complementary marker facilitating timely diagnosis of the disease, an essential prerequisite for improving oncological outcome. Importantly, the presented data indicate that due to physiological age-related glycosylation changes, the performance of IgG glycosylation as EOC complementary screening marker depends on patients' age and hence is decisively better in pre-menopausal women. Moreover, by providing subclass-specific glycosylation information, the results of this work fill an existing knowledge gap left by previous studies, in which EOC-related *N*-glycosylation alterations were investigated at the level of total serum IgG and enzymatically released *N*-glycans. An implemented approach revealed that, despite high homology at the amino acid level, IgG_1, IgG_2, and IgG_3 subclasses differ in respect to Fc glycosylation profiles and their EOC-related alterations. This finding is of particular importance in respect to IgG_2 and IgG_3, which due to technical reasons are typically investigated collectively. Notably, data presented in this study revealed that IgG_1 is the most indicative of an ongoing EOC disease and, in combination with CA 125, shows the most improved diagnostic potential as compared to CA 125 marker alone. Considering its high concentration in blood, IgG_1 represents a promising candidate for an adjuvant EOC disease marker.

While the analysis of glycosylation alterations in IgG protein provided an insight into the host's immune system response to the ongoing EOC disease, the following analysis of *N*-glycans expressed in EOC tissue allowed determining glycosylation changes occurring directly on malignantly transformed cells. Since carbohydrate coating of cancer cells is engaged in various cellular processes, many of which are crucial for tumor progression and metastasis, the in-depth examination of EOC cell surface *N*-glycome holds promise for revealing novel diagnostic markers and/or therapeutic targets. Indeed, *N*-glycosylation patterns observed in investigated EOC tissue specimens exhibited strong tissue type-specificity. Precisely, while high-mannose and α2,6-sialylated complex-type *N*-glycans were predominantly localized to tumor and tumor-related necrotic regions, non-tumor areas of all investigated EOC tissues were characterized by an increased abundance of complex-type

neutral and α2,3-sialylated structures. These findings confirm that besides genetic alterations that are considered a primary cause of cancer development malignant transformation of ovarian epithelial cells is accompanied by specific alterations in protein *N*-glycosylation. In particular, presented data indicate that EOC development is marked by aberrant cell surface sialylation, which glycosylation feature was shown to be linked to tumor progression and metastasis. Importantly, apart from defining spatial glycomic fingerprints of EOC tissue, this work revealed a collection of *N*-glycan structures with biomarker potential. Their effectiveness in distinguishing the pathologically altered tumor from healthy surrounding tissue will be evaluated in a bigger cohort study. Moreover, to gain more detailed information about molecular alterations occurring in EOC tissue, in the future, it is planned to incorporate other types of 'omics' (in particular proteomics) into the presented glycomic pipeline. The *N*-glycomic signatures presented in this work might be of value for a better understanding of EOC intra-tumoral heterogeneity and the identification of new targets for specific drug delivery systems. Additionally, presented data might help to unravel (potentially glycan-involving) mechanisms underlying variable patients' responsiveness/sensitivity to targeted anti-cancer therapeutics.

Chapter VI References

[1] American Cancer Society. (2018) Global Cancer Facts & Figures 4th Edition.

[2] Bray, F., Ferlay, J., Soerjomataram, I., Siegel, R. L., Torre, L. A., and Jemal, A. (2018) Global cancer statistics 2018: GLOBOCAN estimates of incidence and mortality worldwide for 36 cancers in 185 countries, *CA Cancer J Clin 68*, 394-424.

[3] Prat, J., and Figo Committee on Gynecologic Oncology. (2015) FIGO's staging classification for cancer of the ovary, fallopian tube, and peritoneum: abridged republication, *J Gynecol Oncol 26*, 87-89.

[4] National Cancer Institute. (2020) Cancer Stat Facts: Ovarian Cancer, In *The Surveillance, Epidemiology, and End Results (SEER) Registry*.

[5] Meinhold-Heerlein, I., Fotopoulou, C., Harter, P., Kurzeder, C., Mustea, A., Wimberger, P., Hauptmann, S., and Sehouli, J. (2016) The new WHO classification of ovarian, fallopian tube, and primary peritoneal cancer and its clinical implications, *Arch Gynecol Obstet 293*, 695-700.

[6] Auersperg, N. (2013) The origin of ovarian cancers-hypotheses and controversies, *Front Biosci (Schol Ed) 5*, 709-719.

[7] Rojas, V., Hirshfield, K. M., Ganesan, S., and Rodriguez-Rodriguez, L. (2016) Molecular Characterization of Epithelial Ovarian Cancer: Implications for Diagnosis and Treatment, *Int J Mol Sci 17*.

[8] National Academies of Sciences. (2016) The Biology of Ovarian Cancers, In *Ovarian Cancers: Evolving Paradigms in Research and Care.*, The National Academies Press, Washington (DC).

[9] Kurman, R. J. (2013) Origin and molecular pathogenesis of ovarian high-grade serous carcinoma, *Ann Oncol 24 Suppl 10*, 16-21.

[10] Kurman, R. J., and Shih Ie, M. (2011) Molecular pathogenesis and extraovarian origin of epithelial ovarian cancer-shifting the paradigm, *Hum Pathol 42*, 918-931.

[11] Kurman, R. J., and Shih Ie, M. (2016) The Dualistic Model of Ovarian Carcinogenesis: Revisited, Revised, and Expanded, *Am J Pathol 186*, 733-747.

[12] Shih Ie, M., and Kurman, R. J. (2004) Ovarian tumorigenesis: a proposed model based on morphological and molecular genetic analysis, *Am J Pathol 164*, 1511-1518.

[13] Kurman, R. J., and Shih Ie, M. (2008) Pathogenesis of ovarian cancer: lessons from morphology and molecular biology and their clinical implications, *Int J Gynecol Pathol 27*, 151-160.

[14] Orr, B., and Edwards, R. P. (2018) Diagnosis and Treatment of Ovarian Cancer, *Hematol Oncol Clin North Am 32*, 943-964.

[15] Kabawat, S. E., Bast, R. C., Jr., Bhan, A. K., Welch, W. R., Knapp, R. C., and Colvin, R. B. (1983) Tissue distribution of a coelomic-epithelium-related antigen recognized by the monoclonal antibody OC125, *Int J Gynecol Pathol 2*, 275-285.

[16] O'Brien, T. J., Beard, J. B., Underwood, L. J., Dennis, R. A., Santin, A. D., and York, L. (2001) The CA 125 gene: an extracellular superstructure dominated by repeat sequences, *Tumour Biol 22*, 348-366.

[17] Yin, B. W., and Lloyd, K. O. (2001) Molecular cloning of the CA125 ovarian cancer antigen: identification as a new mucin, MUC16, *J Biol Chem 276*, 27371-27375.

[18] Bast, R. C., Jr., Klug, T. L., St John, E., Jenison, E., Niloff, J. M., Lazarus, H., Berkowitz, R. S., Leavitt, T., Griffiths, C. T., Parker, L., Zurawski, V. R., Jr., and Knapp, R. C. (1983) A radioimmunoassay using a monoclonal antibody to monitor the course of epithelial ovarian cancer, *N Engl J Med 309*, 883-887.

[19] Kenemans, P., van Kamp, G. J., Oehr, P., and Verstraeten, R. A. (1993) Heterologous double-determinant immunoradiometric assay CA 125 II: reliable second-generation immunoassay for determining CA 125 in serum, *Clin Chem 39*, 2509-2513.

[20] Bast, R. C., Jr., Feeney, M., Lazarus, H., Nadler, L. M., Colvin, R. B., and Knapp, R. C. (1981) Reactivity of a monoclonal antibody with human ovarian carcinoma, *J Clin Invest 68*, 1331-1337.

[21] Bressan, A., Bozzo, F., Maggi, C. A., and Binaschi, M. (2013) OC125, M11 and OV197 epitopes are not uniformly distributed in the tandem-repeat region of CA125 and require the entire SEA domain, *Dis Markers 34*, 257-267.

[22] Norum, L. F., Erikstein, B., and Nustad, K. (2001) Elevated CA125 in breast cancer-A sign of advanced disease, *Tumour Biol 22*, 223-228.

[23] Yamamoto, M., Baba, H., Toh, Y., Okamura, T., and Maehara, Y. (2007) Peritoneal lavage CEA/CA125 is a prognostic factor for gastric cancer patients, *J Cancer Res Clin Oncol 133*, 471-476.

[24] Hedman, M., Arnberg, H., Wernlund, J., Riska, H., and Brodin, O. (2003) Tissue polypeptide antigen (TPA), hyaluronan and CA 125 as serum markers in malignant mesothelioma, *Anticancer Res 23*, 531-536.

[25] Bairey, O., Blickstein, D., Stark, P., Prokocimer, M., Nativ, H. M., Kirgner, I., and Shaklai, M. (2003) Serum CA 125 as a prognostic factor in non-Hodgkin's lymphoma, *Leuk Lymphoma 44*, 1733-1738.

[26] Lehtovirta, P., Apter, D., and Stenman, U. H. (1990) Serum CA 125 levels during the menstrual cycle, *Br J Obstet Gynaecol 97*, 930-933.

[27] Baalbergen, A., Janssen, J. W., and van der Weiden, R. M. (2000) CA-125 levels are related to the likelihood of pregnancy after in vitro fertilization and embryo transfer, *Am J Reprod Immunol 43*, 21-24.

[28] Cheng, Y. M., Wang, S. T., and Chou, C. Y. (2002) Serum CA-125 in preoperative patients at high risk for endometriosis, *Obstet Gynecol 99*, 375-380.

[29] Soletormos, G., Duffy, M. J., Othman Abu Hassan, S., Verheijen, R. H., Tholander, B., Bast, R. C., Jr., Gaarenstroom, K. N., Sturgeon, C. M., Bonfrer, J. M., Petersen, P. H., Troonen, H., CarloTorre, G., Kanty Kulpa, J., Tuxen, M. K., and Molina, R. (2016) Clinical Use of Cancer Biomarkers in Epithelial Ovarian Cancer: Updated Guidelines From the European Group on Tumor Markers, *Int J Gynecol Cancer 26*, 43-51.

[30] Botta, G., and Zarcone, R. (1995) Trans-vaginal ultrasound examination of ovarian masses in premenopausal women, *Eur J Obstet Gynecol Reprod Biol 62*, 37-41.

[31] Fung, E. T. (2010) A recipe for proteomics diagnostic test development: the OVA1 test, from biomarker discovery to FDA clearance, *Clin Chem 56*, 327-329.

[32] Muller, C. Y. (2010) Doctor, should I get this new ovarian cancer test-OVA1?, *Obstet Gynecol 116*, 246-247.

[33] Varki, A., and Gagneux, P. (2015) Biological Functions of Glycans, In *Essentials of Glycobiology*, Cold Spring Harbor Laboratory Press, New York, 77-78.

[34] Rutishauser, U., and Landmesser, L. (1996) Polysialic acid in the vertebrate nervous system: a promoter of plasticity in cell-cell interactions, *Trends Neurosci 19*, 422-427.

[35] Weinbaum, S., Tarbell, J. M., and Damiano, E. R. (2007) The structure and function of the endothelial glycocalyx layer, *Annu Rev Biomed Eng 9*, 121-167.

[36] Parekh, R. B. (1991) Effects of glycosylation on protein function, *Curr Opin Struc Biol 1*, 750-754.

[37] Bernard, B. A., Newton, S. A., and Olden, K. (1983) Effect of size and location of the oligosaccharide chain on protease degradation of bovine pancreatic ribonuclease, *J Biol Chem 258*, 12198-12202.

[38] Arike, L., and Hansson, G. C. (2016) The Densely O-Glycosylated MUC2 Mucin Protects the Intestine and Provides Food for the Commensal Bacteria, *J Mol Biol 428*, 3221-3229.

[39] Bertozzi, C. R., and Rabuka, D. (2009) Structural Basis of Glycan Diversity, In *Essentials of Glycobiology*, Cold Spring Harbor Laboratory Press, New York, 23-36.

[40] Irie, A., Koyama, S., Kozutsumi, Y., Kawasaki, T., and Suzuki, A. (1998) The molecular basis for the absence of N-glycolylneuraminic acid in humans, *J Biol Chem 273*, 15866-15871.

[41] Samraj, A. N., Pearce, O. M., Laubli, H., Crittenden, A. N., Bergfeld, A. K., Banda, K., Gregg, C. J., Bingman, A. E., Secrest, P., Diaz, S. L., Varki, N. M., and Varki, A. (2015) A red meat-derived glycan promotes inflammation and cancer progression, *Proc Natl Acad Sci U S A 112*, 542-547.

[42] Herscovics, A., and Orlean, P. (1993) Glycoprotein-Biosynthesis in Yeast, *Faseb J 7*, 540-550.

[43] Stanley, P., Schachter, H., and Taniguchi, N. (2009) N-Glycans, In *Essentials of Glycobiology*, Cold Spring Harbor Laboratory Press, New York, 101-114.

[44] Munkley, J., and Elliott, D. J. (2016) Hallmarks of glycosylation in cancer, *Oncotarget 7*, 35478-35489.

[45] Vajaria, B. N., and Patel, P. S. (2017) Glycosylation: a hallmark of cancer?, *Glycoconj J 34*, 147-156.

[46] Abd Hamid, U. M., Royle, L., Saldova, R., Radcliffe, C. M., Harvey, D. J., Storr, S. J., Pardo, M., Antrobus, R., Chapman, C. J., Zitzmann, N., Robertson, J. F., Dwek, R. A., and Rudd, P. M. (2008) A strategy to reveal potential glycan markers from serum glycoproteins associated with breast cancer progression, *Glycobiology 18*, 1105-1118.

[47] Saldova, R., Wormald, M. R., Dwek, R. A., and Rudd, P. M. (2008) Glycosylation changes on serum glycoproteins in ovarian cancer may contribute to disease pathogenesis, *Dis Markers 25*, 219-232.

[48] Arnold, J. N., Saldova, R., Galligan, M. C., Murphy, T. B., Mimura-Kimura, Y., Telford, J. E., Godwin, A. K., and Rudd, P. M. (2011) Novel glycan biomarkers for the detection of lung cancer, *J Proteome Res 10*, 1755-1764.

[49] Takeuchi, M., Kitamura, H., Tsukamoto, T., Masumori, N., Amano, M., Hirose, K., Ohashi, T., and Nishimura, S. I. (2014) N- and O-Glycome Analysis of Serum and Urine from Bladder Cancer Patients Using a High-Throughput Glycoblotting Method, *J Urology 191*, E427.

[50] Kyselova, Z., Mechref, Y., Al Bataineh, M. M., Dobrolecki, L. E., Hickey, R. J., Vinson, J., Sweeney, C. J., and Novotny, M. V. (2007) Alterations in the serum glycome due to metastatic prostate cancer, *J Proteome Res 6*, 1822-1832.

[51] Ichikawa, D., Kitamura, K., Tani, N., Nishida, S., Tsurutome, H., Hakomori, S., Ikeda, E., Mutoh, F., Kurioka, H., and Yamagishi, H. (2000) Molecular detection of disseminated cancer cells in the peripheral blood and expression of sialylated antigens in colon cancers, *J Surg Oncol 75*, 98-102.

[52] Nakamori, S., Kameyama, M., Imaoka, S., Furukawa, H., Ishikawa, O., Sasaki, Y., Kabuto, T., Iwanaga, T., Matsushita, Y., and Irimura, T. (1993) Increased expression of sialyl Lewis x antigen correlates with poor survival in patients with colorectal carcinoma: clinicopathological and immunohistochemical study, *Cancer Res 53*, 3632-3637.

[53] Duche, J. C., Urien, S., Simon, N., Malaurie, E., Monnet, I., and Barre, J. (2000) Expression of the genetic variants of human alpha-1-acid glycoprotein in cancer, *Clin Biochem 33*, 197-202.

[54] Weiz, S., Wieczorek, M., Schwedler, C., Kaup, M., Braicu, E. I., Sehouli, J., Tauber, R., and Blanchard, V. (2016) Acute-phase glycoprotein N-glycome of ovarian cancer patients analyzed by CE-LIF, *Electrophoresis 37*, 1461-1467.

[55] Croce, M. V., Salice, V. C., Lacunza, E., and Segal-Eiras, A. (2005) Alpha 1-acid glycoprotein (AGP): a possible carrier of sialyl lewis X (slewis X) antigen in colorectal carcinoma, *Histol Histopathol 20*, 91-97.

[56] Zhang, Y., and Pastan, I. (2008) High shed antigen levels within tumors: an additional barrier to immunoconjugate therapy, *Clin Cancer Res 14*, 7981-7986.

[57] Sterling, R. K., Jeffers, L., Gordon, F., Sherman, M., Venook, A. P., Reddy, K. R., Satomura, S., and Schwartz, M. E. (2007) Clinical utility of AFP-L3% measurement in North American patients with HCV-related cirrhosis, *Am J Gastroenterol 102*, 2196-2205.

[58] Nakagawa, T., Miyoshi, E., Yakushijin, T., Hiramatsu, N., Igura, T., Hayashi, N., Taniguchi, N., and Kondo, A. (2008) Glycomic analysis of alpha-fetoprotein L3 in hepatoma cell lines and hepatocellular carcinoma patients, *J Proteome Res 7*, 2222-2233.

[59] Pihikova, D., Kasak, P., Kubanikova, P., Sokol, R., and Tkac, J. (2016) Aberrant sialylation of a prostate-specific antigen: Electrochemical label-free glycoprofiling in prostate cancer serum samples, *Anal Chim Acta 934*, 72-79.

[60] Llop, E., Ferrer-Batalle, M., Barrabes, S., Guerrero, P. E., Ramirez, M., Saldova, R., Rudd, P. M., Aleixandre, R. N., Comet, J., de Llorens, R., and Peracaula, R. (2016) Improvement of Prostate Cancer Diagnosis by Detecting PSA Glycosylation-Specific Changes, *Theranostics 6*, 1190-1204.

[61] Ruhaak, L. R., Barkauskas, D. A., Torres, J., Cooke, C. L., Wu, L. D., Stroble, C., Ozcan, S., Williams, C. C., Camorlinga, M., Rocke, D. M., Lebrilla, C. B., and Solnick, J. V. (2015) The Serum Immunoglobulin G Glycosylation Signature of Gastric Cancer, *EuPA Open Proteom 6*, 1-9.

[62] Saldova, R., Stockmann, H., O'Flaherty, R., Lefeber, D. J., Jaeken, J., and Rudd, P. M. (2015) N-Glycosylation of Serum IgG and Total Glycoproteins in MAN1B1 Deficiency, *J Proteome Res 14*, 4402-4412.

[63] Theodoratou, E., Thaci, K., Agakov, F., Timofeeva, M. N., Stambuk, J., Pucic-Bakovic, M., Vuckovic, F., Orchard, P., Agakova, A., Din, F. V., Brown, E., Rudd, P. M., Farrington, S. M., Dunlop, M. G., Campbell, H., and Lauc, G. (2016) Glycosylation of plasma IgG in colorectal cancer prognosis, *Sci Rep 6*, 28098.

[64] Kanoh, Y., Mashiko, T., Danbara, M., Takayama, Y., Ohtani, S., Imasaki, T., Abe, T., and Akahoshi, T. (2004) Analysis of the oligosaccharide chain of human serum immunoglobulin g in patients with localized or metastatic cancer, *Oncology 66*, 365-370.

[65] Kanoh, Y., Mashiko, T., Danbara, M., Takayama, Y., Ohtani, S., Egawa, S., Baba, S., and Akahoshi, T. (2004) Changes in serum IgG oligosaccharide chains with prostate cancer progression, *Anticancer Res 24*, 3135-3139.

[66] Parekh, R. B., Dwek, R. A., Sutton, B. J., Fernandes, D. L., Leung, A., Stanworth, D., Rademacher, T. W., Mizuochi, T., Taniguchi, T., Matsuta, K., and et al. (1985) Association of rheumatoid arthritis and primary osteoarthritis with changes in the glycosylation pattern of total serum IgG, *Nature 316*, 452-457.

[67] Ren, S., Zhang, Z., Xu, C., Guo, L., Lu, R., Sun, Y., Guo, J., Qin, R., Qin, W., and Gu, J. (2016) Distribution of IgG galactosylation as a promising biomarker for cancer screening in multiple cancer types, *Cell Res 26*, 963-966.

[68] Kodar, K., Stadlmann, J., Klaamas, K., Sergeyev, B., and Kurtenkov, O. (2012) Immunoglobulin G Fc N-glycan profiling in patients with gastric cancer by LC-ESI-MS: relation to tumor progression and survival, *Glycoconj J 29*, 57-66.

[69] Bones, J., Byrne, J. C., O'Donoghue, N., McManus, C., Scaife, C., Boissin, H., Nastase, A., and Rudd, P. M. (2011) Glycomic and glycoproteomic analysis of serum from patients with stomach cancer reveals potential markers arising from host defense response mechanisms, *J Proteome Res 10*, 1246-1265.

[70] Barthel, S. R., Gavino, J. D., Wiese, G. K., Jaynes, J. M., Siddiqui, J., and Dimitroff, C. J. (2008) Analysis of glycosyltransferase expression in metastatic prostate cancer cells capable of rolling activity on microvascular endothelial (E)-selectin, *Glycobiology 18*, 806-817.

[71] Li, J., Guillebon, A. D., Hsu, J. W., Barthel, S. R., Dimitroff, C. J., Lee, Y. F., and King, M. R. (2013) Human fucosyltransferase 6 enables prostate cancer metastasis to bone, *Br J Cancer 109*, 3014-3022.

[72] Wang, X., Chen, J., Li, Q. K., Peskoe, S. B., Zhang, B., Choi, C., Platz, E. A., and Zhang, H. (2014) Overexpression of alpha (1,6) fucosyltransferase associated with aggressive prostate cancer, *Glycobiology 24*, 935-944.

[73] Yin, X., Rana, K., Ponmudi, V., and King, M. R. (2010) Knockdown of fucosyltransferase III disrupts the adhesion of circulating cancer cells to E-selectin without affecting hematopoietic cell adhesion, *Carbohydr Res 345*, 2334-2342.

[74] Okeley, N. M., Alley, S. C., Anderson, M. E., Boursalian, T. E., Burke, P. J., Emmerton, K. M., Jeffrey, S. C., Klussman, K., Law, C. L., Sussman, D., Toki, B. E., Westendorf, L., Zeng, W., Zhang, X., Benjamin, D. R., and Senter, P. D. (2013) Development of orally active inhibitors of protein and cellular fucosylation, *Proc Natl Acad Sci U S A 110*, 5404-5409.

[75] Desiderio, V., Papagerakis, P., Tirino, V., Zheng, L., Matossian, M., Prince, M. E., Paino, F., Mele, L., Papaccio, F., Montella, R., Papaccio, G., and Papagerakis, S. (2015) Increased fucosylation has a pivotal role in invasive and metastatic properties of head and neck cancer stem cells, *Oncotarget 6*, 71-84.

[76] Yousefi, S., Higgins, E., Daoling, Z., Pollex-Kruger, A., Hindsgaul, O., and Dennis, J. W. (1991) Increased UDP-GlcNAc:Gal beta 1-3GaLNAc-R (GlcNAc to GaLNAc) beta-1, 6-N-acetylglucosaminyltransferase activity in metastatic murine tumor cell lines. Control of polylactosamine synthesis, *J Biol Chem 266*, 1772-1782.

[77] Partridge, E. A., Le Roy, C., Di Guglielmo, G. M., Pawling, J., Cheung, P., Granovsky, M., Nabi, I. R., Wrana, J. L., and Dennis, J. W. (2004) Regulation of cytokine receptors by Golgi N-glycan processing and endocytosis, *Science 306*, 120-124.

[78] Lau, K. S., Partridge, E. A., Grigorian, A., Silvescu, C. I., Reinhold, V. N., Demetriou, M., and Dennis, J. W. (2007) Complex N-glycan number and degree of branching cooperate to regulate cell proliferation and differentiation, *Cell 129*, 123-134.

[79] Schauer, R. (1985) Sialic acids and their role as biological masks, *Trends in Biochemical Sciences 10*, 357-360.

[80] Seidenfaden, R., Krauter, A., Schertzinger, F., Gerardy-Schahn, R., and Hildebrandt, H. (2003) Polysialic acid directs tumor cell growth by controlling heterophilic neural cell adhesion molecule interactions, *Mol Cell Biol 23*, 5908-5918.

[81] Laubli, H., and Borsig, L. (2010) Selectins promote tumor metastasis, *Semin Cancer Biol 20*, 169-177.

[82] Dall'Olio, F., Malagolini, N., Trinchera, M., and Chiricolo, M. (2012) Mechanisms of cancer-associated glycosylation changes, *Front Biosci (Landmark Ed) 17*, 670-699.

[83] Cui, H., Lin, Y., Yue, L., Zhao, X., and Liu, J. (2011) Differential expression of the alpha2,3-sialic acid residues in breast cancer is associated with metastatic potential, *Oncol Rep 25*, 1365-1371.

[84] Varki, A., Kannagi, R., Toole, B., and Stanley, P. (2015) Glycosylation Changes in Cancer, In *Essentials of Glycobiology*, Cold Spring Harbor Laboratory Press, New York.

[85] Skacel, P. O., Edwards, A. J., Harrison, C. T., and Watkins, W. M. (1991) Enzymic control of the expression of the X determinant (CD15) in human myeloid cells during maturation: the regulatory role of 6-sialytransferase, *Blood 78*, 1452-1460.

[86] Wang, P. H., Li, Y. F., Juang, C. M., Lee, Y. R., Chao, H. T., Tsai, Y. C., and Yuan, C. C. (2001) Altered mRNA expression of sialyltransferase in squamous cell carcinomas of the cervix, *Gynecol Oncol 83*, 121-127.

[87] Jun, L., Yuanshu, W., Yanying, X., Zhongfa, X., Jian, Y., Fengling, W., Xianjun, Q., Kokudo, N., Wei, T., Weixia, Z., and Shuxiang, C. (2012) Altered mRNA expressions of sialyltransferases in human gastric cancer tissues, *Med Oncol 29*, 84-90.

[88] Schultz, M. J., Swindall, A. F., Wright, J. W., Sztul, E. S., Landen, C. N., and Bellis, S. L. (2013) ST6Gal-I sialyltransferase confers cisplatin resistance in ovarian tumor cells, *J Ovarian Res 6*, 25.

[89] Sata, T., Roth, J., Zuber, C., Stamm, B., and Heitz, P. U. (1991) Expression of Alpha-2,6-Linked Sialic-Acid Residues in Neoplastic but Not in Normal Human Colonic Mucosa - a Lectin-Gold Cytochemical Study with Sambucus-Nigra and Maackia-Amurensis Lectins, *Am J Pathol 139*, 1435-1448.

[90] Kaneko, Y., Yamamoto, H., Kersey, D. S., Colley, K. J., Leestma, J. E., and Moskal, J. R. (1996) The expression of Gal beta 1,4GlcNAc alpha 2,6 sialyltransferase and alpha 2,6-linked sialoglycoconjugates in human brain tumors, *Acta Neuropathol 91*, 284-292.

[91] Recchi, M. A., Hebbar, M., Hornez, L., Harduin-Lepers, A., Peyrat, J. P., and Delannoy, P. (1998) Multiplex reverse transcription polymerase chain reaction assessment of sialyltransferase expression in human breast cancer, *Cancer Res 58*, 4066-4070.

[92] Dall'Olio, F., Chiricolo, M., D'Errico, A., Gruppioni, E., Altimari, A., Fiorentino, M., and Grigioni, W. F. (2004) Expression of beta-galactoside alpha2,6 sialyltransferase and of alpha2,6-sialylated glycoconjugates in normal human liver, hepatocarcinoma, and cirrhosis, *Glycobiology 14*, 39-49.

[93] Yang, G., Tan, Z., Lu, W., Guo, J., Yu, H., Yu, J., Sun, C., Qi, X., Li, Z., and Guan, F. (2015) Quantitative glycome analysis of N-glycan patterns in bladder cancer vs normal bladder cells using an integrated strategy, *J Proteome Res 14*, 639-653.

[94] Braig, F., Kriegs, M., Voigtlaender, M., Habel, B., Grob, T., Biskup, K., Blanchard, V., Sack, M., Thalhammer, A., Ben Batalla, I., Braren, I., Laban, S., Danielczyk, A., Goletz, S., Jakubowicz, E., Markl, B., Trepel, M., Knecht, R., Riecken, K., Fehse, B., Loges, S., Bokemeyer, C., and Binder, M. (2017) Cetuximab Resistance in Head and Neck Cancer Is Mediated by EGFR-K521 Polymorphism, *Cancer Res 77*, 1188-1199.

[95] de Leoz, M. L., Young, L. J., An, H. J., Kronewitter, S. R., Kim, J., Miyamoto, S., Borowsky, A. D., Chew, H. K., and Lebrilla, C. B. (2011) High-mannose glycans are elevated during breast cancer progression, *Mol Cell Proteomics 10*, M110 002717.

[96] Balog, C. I., Stavenhagen, K., Fung, W. L., Koeleman, C. A., McDonnell, L. A., Verhoeven, A., Mesker, W. E., Tollenaar, R. A., Deelder, A. M., and Wuhrer, M. (2012) N-glycosylation of colorectal cancer tissues: a liquid chromatography and mass spectrometry-based investigation, *Mol Cell Proteomics 11*, 571-585.

[97] Wanyama, F. M., and Blanchard, V. (2021) Glycomic-Based Biomarkers for Ovarian Cancer: Advances and Challenges, *Diagnostics (Basel) 11*.

[98] Donnelly, D. P., Rawlins, C. M., DeHart, C. J., Fornelli, L., Schachner, L. F., Lin, Z., Lippens, J. L., Aluri, K. C., Sarin, R., Chen, B., Lantz, C., Jung, W., Johnson, K. R., Koller, A., Wolff, J. J., Campuzano, I. D. G., Auclair, J. R., Ivanov, A. R., Whitelegge, J. P., Pasa-Tolic, L., Chamot-Rooke, J., Danis, P. O., Smith, L. M., Tsybin, Y. O., Loo, J. A., Ge, Y., Kelleher, N. L., and Agar, J. N. (2019) Best practices and benchmarks for intact protein analysis for top-down mass spectrometry, *Nat Methods 16*, 587-594.

[99] Struwe, W., Cosgrave, E., Byrne, J., Saldova, R., Rudd, P. (2011) Glycoproteomics in Health and Disease, In *Functional and structural proteomics of glycoproteins*, Springer, 1-38.

[100] Patel, T., Bruce, J., Merry, A., Bigge, C., Wormald, M., Jaques, A., and Parekh, R. (1993) Use of Hydrazine to Release in Intact and Unreduced Form Both N-Linked and O-Linked Oligosaccharides from Glycoproteins, *Biochemistry-Us 32*, 679-693.

[101] Maley, F., Trimble, R. B., Tarentino, A. L., and Plummer, T. H. (1989) Characterization of Glycoproteins and Their Associated Oligosaccharides through the Use of Endoglycosidases, *Anal Biochem 180*, 195-204.

[102] Harvey, D. J. (2006) Analysis of carbohydrates and glycoconjugates by matrix-assisted laser desorption/ionization mass spectrometry: An update covering the period 1999-2000, *Mass Spectrom Rev 25*, 595-662.

[103] Hosseini, S., Martinez-Chapa, S. O. (2017) Principles and Mechanism of MALDI-ToF-MS Analysis, In *Fundamentals of MALDI-ToF-MS analysis*, Springer Nature, 1-19.

[104] Selman, M. H., Hoffmann, M., Zauner, G., McDonnell, L. A., Balog, C. I., Rapp, E., Deelder, A. M., and Wuhrer, M. (2012) MALDI-TOF-MS analysis of sialylated glycans and glycopeptides using 4-chloro-alpha-cyanocinnamic acid matrix, *Proteomics 12*, 1337-1348.

[105] Boesl, U. (2017) Time-of-flight mass spectrometry: Introduction to the basics, *Mass Spectrom Rev 36*, 86-109.

[106] Powell, A. K., and Harvey, D. J. (1996) Stabilization of sialic acids in N-linked oligosaccharides and gangliosides for analysis by positive ion matrix-assisted laser desorption/ionization mass spectrometry, *Rapid Commun Mass Spectrom 10*, 1027-1032.

[107] Ciucanu, I. K., F. (1984) A simple and rapid method for the permethylation of carbohydrates, *Carbohydrate research 131,* 209-217.

[108] Liu, X., Qiu, H., Lee, R. K., Chen, W., and Li, J. (2010) Methylamidation for sialoglycomics by MALDI-MS: a facile derivatization strategy for both alpha2,3- and alpha2,6-linked sialic acids, *Anal Chem 82*, 8300-8306.

[109] Reiding, K. R., Blank, D., Kuijper, D. M., Deelder, A. M., and Wuhrer, M. (2014) High-throughput profiling of protein N-glycosylation by MALDI-TOF-MS employing linkage-specific sialic acid esterification, *Anal Chem 86*, 5784-5793.

[110] Wheeler, S. F., Domann, P., and Harvey, D. J. (2009) Derivatization of sialic acids for stabilization in matrix-assisted laser desorption/ionization mass spectrometry and concomitant differentiation of alpha(2 --> 3)- and alpha(2 --> 6)-isomers, *Rapid Commun Mass Spectrom 23*, 303-312.

[111] Sekiya, S., Wada, Y., and Tanaka, K. (2005) Derivatization for stabilizing sialic acids in MALDI-MS, *Anal Chem 77*, 4962-4968.

[112] de Haan, N., Reiding, K. R., Haberger, M., Reusch, D., Falck, D., and Wuhrer, M. (2015) Linkage-specific sialic acid derivatization for MALDI-TOF-MS profiling of IgG glycopeptides, *Anal Chem 87*, 8284-8291.

[113] Holst, S., Heijs, B., de Haan, N., van Zeijl, R. J., Briaire-de Bruijn, I. H., van Pelt, G. W., Mehta, A. S., Angel, P. M., Mesker, W. E., Tollenaar, R. A., Drake, R. R., Bovee, J. V., McDonnell, L. A., and Wuhrer, M. (2016) Linkage-Specific in Situ Sialic Acid Derivatization for N-Glycan Mass Spectrometry Imaging of Formalin-Fixed Paraffin-Embedded Tissues, *Anal Chem 88*, 5904-5913.

[114] Schur, P. H. (1988) IgG subclasses. A historical perspective, *Monogr Allergy 23*, 1-11.

[115] Vidarsson, G., Dekkers, G., and Rispens, T. (2014) IgG subclasses and allotypes: from structure to effector functions, *Front Immunol 5*, 520.

[116] Kuijpers, T. W., Weening, R. S., and Out, T. A. (1992) IgG subclass deficiencies and recurrent pyogenic infections, unresponsiveness against bacterial polysaccharide antigens, *Allergol Immunopathol (Madr) 20*, 28-34.

[117] Sundqvist, V. A., Linde, A., and Wahren, B. (1984) Virus-specific immunoglobulin G subclasses in herpes simplex and varicella-zoster virus infections, *J Clin Microbiol 20*, 94-98.

[118] Yates, N. L., Lucas, J. T., Nolen, T. L., Vandergrift, N. A., Soderberg, K. A., Seaton, K. E., Denny, T. N., Haynes, B. F., Cohen, M. S., and Tomaras, G. D. (2011) Multiple HIV-1-specific IgG3 responses decline during acute HIV-1: implications for detection of incident HIV infection, *AIDS 25*, 2089-2097.

[119] Isenman, D. E., Dorrington, K. J., and Painter, R. H. (1975) The structure and function of immunoglobulin domains. II. The importance of interchain disulfide bonds and the possible role of molecular flexibility in the interaction between immunoglobulin G and complement, *J Immunol 114*, 1726-1729.

[120] Dushek, O., Goyette, J., and van der Merwe, P. A. (2012) Non-catalytic tyrosine-phosphorylated receptors, *Immunol Rev 250*, 258-276.

[121] Ravetch, J. V., and Bolland, S. (2001) IgG Fc receptors, *Annu Rev Immunol 19*, 275-290.

[122] Bournazos, S., Wang, T. T., and Ravetch, J. V. (2016) The Role and Function of Fcgamma Receptors on Myeloid Cells, *Microbiol Spectr 4*.

[123] Li, F., Smith, P., and Ravetch, J. V. (2014) Inhibitory Fcgamma receptor is required for the maintenance of tolerance through distinct mechanisms, *J Immunol 192*, 3021-3028.

[124] Lu, J., Chu, J., Zou, Z., Hamacher, N. B., Rixon, M. W., and Sun, P. D. (2015) Structure of FcgammaRI in complex with Fc reveals the importance of glycan recognition for high-affinity IgG binding, *Proc Natl Acad Sci U S A 112*, 833-838.

[125] Bruhns, P., Iannascoli, B., England, P., Mancardi, D. A., Fernandez, N., Jorieux, S., and Daeron, M. (2009) Specificity and affinity of human Fcgamma receptors and their polymorphic variants for human IgG subclasses, *Blood 113*, 3716-3725.

[126] Smyth, M. J., Cretney, E., Kelly, J. M., Westwood, J. A., Street, S. E., Yagita, H., Takeda, K., van Dommelen, S. L., Degli-Esposti, M. A., and Hayakawa, Y. (2005) Activation of NK cell cytotoxicity, *Mol Immunol 42*, 501-510.

[127] Voskoboinik, I., Whisstock, J. C., and Trapani, J. A. (2015) Perforin and granzymes: function, dysfunction and human pathology, *Nat Rev Immunol 15*, 388-400.

[128] Dunkelberger, J. R., and Song, W. C. (2010) Complement and its role in innate and adaptive immune responses, *Cell Res 20*, 34-50.

[129] Duncan, A. R., and Winter, G. (1988) The binding site for C1q on IgG, *Nature 332*, 738-740.

[130] Kishore, U., and Reid, K. B. (2000) C1q: structure, function, and receptors, *Immunopharmacology 49*, 159-170.

[131] Bindon, C. I., Hale, G., Bruggemann, M., and Waldmann, H. (1988) Human monoclonal IgG isotypes differ in complement activating function at the level of C4 as well as C1q, *J Exp Med 168*, 127-142.

[132] Banda, N. K., Wood, A. K., Takahashi, K., Levitt, B., Rudd, P. M., Royle, L., Abrahams, J. L., Stahl, G. L., Holers, V. M., and Arend, W. P. (2008) Initiation of the alternative pathway of murine complement by immune complexes is dependent on N-glycans in IgG antibodies, *Arthritis Rheum 58*, 3081-3089.

[133] Arnold, J. N., Wormald, M. R., Sim, R. B., Rudd, P. M., and Dwek, R. A. (2007) The impact of glycosylation on the biological function and structure of human immunoglobulins, *Annu Rev Immunol 25*, 21-50.

[134] Deisenhofer, J. (1981) Crystallographic refinement and atomic models of a human Fc fragment and its complex with fragment B of protein A from Staphylococcus aureus at 2.9- and 2.8-A resolution, *Biochemistry-Us 20*, 2361-2370.

[135] Krapp, S., Mimura, Y., Jefferis, R., Huber, R., and Sondermann, P. (2003) Structural analysis of human IgG-Fc glycoforms reveals a correlation between glycosylation and structural integrity, *J Mol Biol 325*, 979-989.

[136] Tao, M. H., and Morrison, S. L. (1989) Studies of aglycosylated chimeric mouse-human IgG. Role of carbohydrate in the structure and effector functions mediated by the human IgG constant region, *J Immunol 143*, 2595-2601.

[137] Shields, R. L., Lai, J., Keck, R., O'Connell, L. Y., Hong, K., Meng, Y. G., Weikert, S. H., and Presta, L. G. (2002) Lack of fucose on human IgG1 N-linked oligosaccharide improves binding to human Fcgamma RIII and antibody-dependent cellular toxicity, *J Biol Chem 277*, 26733-26740.

[138] Satoh, M., Iida, S., and Shitara, K. (2006) Non-fucosylated therapeutic antibodies as next-generation therapeutic antibodies, *Expert Opin Biol Ther 6*, 1161-1173.

[139] Ferrara, C., Grau, S., Jager, C., Sondermann, P., Brunker, P., Waldhauer, I., Hennig, M., Ruf, A., Rufer, A. C., Stihle, M., Umana, P., and Benz, J. (2011) Unique carbohydrate-carbohydrate interactions are required for high affinity binding between FcgammaRIII and antibodies lacking core fucose, *Proc Natl Acad Sci U S A 108*, 12669-12674.

[140] Imai-Nishiya, H., Mori, K., Inoue, M., Wakitani, M., Iida, S., Shitara, K., and Satoh, M. (2007) Double knockdown of alpha1,6-fucosyltransferase (FUT8) and GDP-mannose 4,6-dehydratase (GMD) in antibody-producing cells: a new strategy for generating fully non-fucosylated therapeutic antibodies with enhanced ADCC, *BMC Biotechnol 7*, 84.

[141] Umana, P., Jean-Mairet, J., Moudry, R., Amstutz, H., and Bailey, J. E. (1999) Engineered glycoforms of an antineuroblastoma IgG1 with optimized antibody-dependent cellular cytotoxic activity, *Nat Biotechnol 17*, 176-180.

[142] Davies, J., Jiang, L., Pan, L. Z., LaBarre, M. J., Anderson, D., and Reff, M. (2001) Expression of GnTIII in a recombinant anti-CD20 CHO production cell line: Expression of antibodies with altered glycoforms leads to an increase in ADCC through higher affinity for FC gamma RIII, *Biotechnol Bioeng 74*, 288-294.

[143] Peschke, B., Keller, C. W., Weber, P., Quast, I., and Lunemann, J. D. (2017) Fc-Galactosylation of Human Immunoglobulin Gamma Isotypes Improves C1q Binding and Enhances Complement-Dependent Cytotoxicity, *Front Immunol 8*, 646.

[144] Arnold, J. N., Royle, L., Dwek, R. A., Rudd, P. M., and Sim, R. B. (2005) Human immunoglobulin glycosylation and the lectin pathway of complement activation, *Adv Exp Med Biol 564*, 27-43.

[145] Kaneko, Y., Nimmerjahn, F., and Ravetch, J. V. (2006) Anti-inflammatory activity of immunoglobulin G resulting from Fc sialylation, *Science 313*, 670-673.

[146] van de Geijn, F. E., Wuhrer, M., Selman, M. H., Willemsen, S. P., de Man, Y. A., Deelder, A. M., Hazes, J. M., and Dolhain, R. J. (2009) Immunoglobulin G galactosylation and sialylation are associated with pregnancy-induced improvement of rheumatoid arthritis and the postpartum flare: results from a large prospective cohort study, *Arthritis Res Ther 11*, R193.

[147] Scallon, B. J., Tam, S. H., McCarthy, S. G., Cai, A. N., and Raju, T. S. (2007) Higher levels of sialylated Fc glycans in immunoglobulin G molecules can adversely impact functionality, *Mol Immunol 44*, 1524-1534.

[148] Anthony, R. M., Kobayashi, T., Wermeling, F., and Ravetch, J. V. (2011) Intravenous gammaglobulin suppresses inflammation through a novel T(H)2 pathway, *Nature 475*, 110-113.

[149] Temming, A. R., Dekkers, G., van de Bovenkamp, F. S., Plomp, H. R., Bentlage, A. E. H., Szittner, Z., Derksen, N. I. L., Wuhrer, M., Rispens, T., and Vidarsson, G. (2019) Human DC-SIGN and CD23 do not interact with human IgG, *Sci Rep 9*, 9995.

[150] Quast, I., Keller, C. W., Maurer, M. A., Giddens, J. P., Tackenberg, B., Wang, L. X., Munz, C., Nimmerjahn, F., Dalakas, M. C., and Lunemann, J. D. (2015) Sialylation of IgG Fc domain impairs complement-dependent cytotoxicity, *J Clin Invest 125*, 4160-4170.

[151] Gercel-Taylor, C., Bazzett, L. B., and Taylor, D. D. (2001) Presence of aberrant tumor-reactive immunoglobulins in the circulation of patients with ovarian cancer, *Gynecol Oncol 81*, 71-76.

[152] Saldova, R., Royle, L., Radcliffe, C. M., Abd Hamid, U. M., Evans, R., Arnold, J. N., Banks, R. E., Hutson, R., Harvey, D. J., Antrobus, R., Petrescu, S. M., Dwek, R. A., and Rudd, P. M. (2007) Ovarian cancer is associated with changes in glycosylation in both acute-phase proteins and IgG, *Glycobiology 17*, 1344-1356.

[153] Alley, W. R., Jr., Vasseur, J. A., Goetz, J. A., Svoboda, M., Mann, B. F., Matei, D. E., Menning, N., Hussein, A., Mechref, Y., and Novotny, M. V. (2012) N-linked glycan structures and their expressions change in the blood sera of ovarian cancer patients, *J Proteome Res 11*, 2282-2300.

[154] Qian, Y., Wang, Y., Zhang, X., Zhou, L., Zhang, Z., Xu, J., Ruan, Y., Ren, S., Xu, C., and Gu, J. (2013) Quantitative analysis of serum IgG galactosylation assists differential diagnosis of ovarian cancer, *J Proteome Res 12*, 4046-4055.

[155] Ruhaak, L. R., Kim, K., Stroble, C., Taylor, S. L., Hong, Q., Miyamoto, S., Lebrilla, C. B., and Leiserowitz, G. (2016) Protein-Specific Differential Glycosylation of Immunoglobulins in Serum of Ovarian Cancer Patients, *J Proteome Res 15*, 1002-1010.

[156] Selman, M. H., Hemayatkar, M., Deelder, A. M., and Wuhrer, M. (2011) Cotton HILIC SPE microtips for microscale purification and enrichment of glycans and glycopeptides, *Anal Chem 83*, 2492-2499.

[157] Jansen, B. C., Reiding, K. R., Bondt, A., Hipgrave Ederveen, A. L., Palmblad, M., Falck, D., and Wuhrer, M. (2015) MassyTools: A High-Throughput Targeted Data Processing Tool for

Relative Quantitation and Quality Control Developed for Glycomic and Glycoproteomic MALDI-MS, *J Proteome Res 14*, 5088-5098.

[158] Parekh, R., Roitt, I., Isenberg, D., Dwek, R., and Rademacher, T. (1988) Age-related galactosylation of the N-linked oligosaccharides of human serum IgG, *J Exp Med 167*, 1731-1736.

[159] Kristic, J., Vuckovic, F., Menni, C., Klaric, L., Keser, T., Beceheli, I., Pucic-Bakovic, M., Novokmet, M., Mangino, M., Thaqi, K., Rudan, P., Novokmet, N., Sarac, J., Missoni, S., Kolcic, I., Polasek, O., Rudan, I., Campbell, H., Hayward, C., Aulchenko, Y., Valdes, A., Wilson, J. F., Gornik, O., Primorac, D., Zoldos, V., Spector, T., and Lauc, G. (2014) Glycans are a novel biomarker of chronological and biological ages, *J Gerontol A Biol Sci Med Sci 69*, 779-789.

[160] Balbin, M., Grubb, A., de Lange, G. G., and Grubb, R. (1994) DNA sequences specific for Caucasian G3m(b) and (g) allotypes: allotyping at the genomic level, *Immunogenetics 39*, 187-193.

[161] Wuhrer, M., Stam, J. C., van de Geijn, F. E., Koeleman, C. A., Verrips, C. T., Dolhain, R. J., Hokke, C. H., and Deelder, A. M. (2007) Glycosylation profiling of immunoglobulin G (IgG) subclasses from human serum, *Proteomics 7*, 4070-4081.

[162] Plomp, R., Ruhaak, L. R., Uh, H. W., Reiding, K. R., Selman, M., Houwing-Duistermaat, J. J., Slagboom, P. E., Beekman, M., and Wuhrer, M. (2017) Subclass-specific IgG glycosylation is associated with markers of inflammation and metabolic health, *Sci Rep 7*, 12325.

[163] Chen, G., Wang, Y., Qin, X., Li, H., Guo, Y., Wang, Y., Liu, H., Wang, X., Song, G., Li, F., Li, F., Guo, S., Qiu, L., and Li, Z. (2013) Change in IgG1 Fc N-linked glycosylation in human lung cancer: age- and sex-related diagnostic potential, *Electrophoresis 34*, 2407-2416.

[164] de Haan, N., Reiding, K. R., Driessen, G., van der Burg, M., and Wuhrer, M. (2016) Changes in Healthy Human IgG Fc-Glycosylation after Birth and during Early Childhood, *J Proteome Res 15*, 1853-1861.

[165] Berek, J. S., Crum, C., and Friedlander, M. (2015) Cancer of the ovary, fallopian tube, and peritoneum, *Int J Gynaecol Obstet 131 Suppl 2*, S111-122.

[166] Schwedler, C., Kaup, M., Weiz, S., Hoppe, M., Braicu, E. I., Sehouli, J., Hoppe, B., Tauber, R., Berger, M., and Blanchard, V. (2014) Identification of 34 N-glycan isomers in human serum by capillary electrophoresis coupled with laser-induced fluorescence allows improving glycan biomarker discovery, *Anal Bioanal Chem 406*, 7185-7193.

[167] Malhotra, R., Wormald, M. R., Rudd, P. M., Fischer, P. B., Dwek, R. A., and Sim, R. B. (1995) Glycosylation changes of IgG associated with rheumatoid arthritis can activate complement via the mannose-binding protein, *Nat Med 1*, 237-243.

[168] Axford, J. S., Alavi, A., Bond, A., and Hay, F. C. (1994) Differential B lymphocyte galactosyltransferase activity in the MRL mouse model of rheumatoid arthritis, *Autoimmunity 17*, 157-163.

[169] Maccio, A., Lai, P., Santona, M. C., Pagliara, L., Melis, G. B., and Mantovani, G. (1998) High serum levels of soluble IL-2 receptor, cytokines, and C reactive protein correlate with impairment of T cell response in patients with advanced epithelial ovarian cancer, *Gynecol Oncol 69*, 248-252.

[170] Franceschi, C., Bonafe, M., Valensin, S., Olivieri, F., De Luca, M., Ottaviani, E., and De Benedictis, G. (2000) Inflamm-aging. An evolutionary perspective on immunosenescence, *Ann N Y Acad Sci 908*, 244-254.

[171] Chung, S., Quarmby, V., Gao, X., Ying, Y., Lin, L., Reed, C., Fong, C., Lau, W., Qiu, Z. J., Shen, A., Vanderlaan, M., and Song, A. (2012) Quantitative evaluation of fucose reducing effects in a humanized antibody on Fcgamma receptor binding and antibody-dependent cell-mediated cytotoxicity activities, *MAbs 4*, 326-340.

[172] Saito, H., Miyatani, K., Kono, Y., Murakami, Y., Kuroda, H., Matsunaga, T., Fukumoto, Y., Takano, S., Osaki, T., and Fujiwara, Y. (2017) Decreased Serum Concentration of Total IgG Is Related to Tumor Progression in Gastric Cancer Patients, *Yonago Acta Med 60*, 119-125.

[173] Yuan, W., Sanda, M., Wu, J., Koomen, J., and Goldman, R. (2015) Quantitative analysis of immunoglobulin subclasses and subclass specific glycosylation by LC-MS-MRM in liver disease, *J Proteomics 116*, 24-33.

[174] Shah, I. S., Lovell, S., Mehzabeen, N., Battaile, K. P., and Tolbert, T. J. (2017) Structural characterization of the Man5 glycoform of human IgG3 Fc, *Mol Immunol 92*, 28-37.

[175] Sonneveld, M. E., Koeleman, C. A. M., Plomp, H. R., Wuhrer, M., van der Schoot, C. E., and Vidarsson, G. (2018) Fc-Glycosylation in Human IgG1 and IgG3 Is Similar for Both Total and Anti-Red-Blood Cell Anti-K Antibodies, *Front Immunol 9*, 129.

[176] Jones, M. B., Oswald, D. M., Joshi, S., Whiteheart, S. W., Orlando, R., and Cobb, B. A. (2016) B-cell-independent sialylation of IgG, *Proc Natl Acad Sci U S A 113*, 7207-7212.

[177] Qin, R., Yang, Y., Chen, H., Qin, W., Han, J., Gu, Y., Pan, Y., Cheng, X., Zhao, J., Wang, X., Ren, S., Sun, Y., and Gu, J. (2020) Prediction of neoadjuvant chemotherapeutic efficacy in patients with locally advanced gastric cancer by serum IgG glycomics profiling, *Clin Proteomics 17*, 4.

[178] Chen, G., Wang, Y., Qiu, L., Qin, X., Liu, H., Wang, X., Wang, Y., Song, G., Li, F., Guo, Y., Li, F., Guo, S., and Li, Z. (2012) Human IgG Fc-glycosylation profiling reveals associations with age, sex, female sex hormones and thyroid cancer, *J Proteomics 75*, 2824-2834.

[179] Lis, H. S., N. (1986) Lectins as Molecules and as Tools, *Annual Review of Biochemistry 55(1)*, 35-67.

[180] Varki, A., Etzler, M. E., Cummings, R. D., and Esko, J. D. (2009) Discovery and Classification of Glycan-Binding Proteins, In *Essentials of Glycobiology*, Cold Spring Harbor Laboratory Press, New York, 375-386.

[181] Rhodes, J., M.; Milton, J.,D. (1998) Lectin Histochemistry and Cytochemistry, In *Lectin Methods and Protocols*, Humana Press Inc., Totowa, New Jersey.

[182] Byrne, P., Williams, A., and Rollason, T. (1989) Studies of lectin binding to the human cervix uteri: II. Cervical intraepithelial neoplasia and invasive squamous carcinoma, *Histochem J 21*, 323-336.

[183] Hori, T., Nishiyama, F., Anno, Y., Adachi, S., Numata, H., Hokama, Y., Muraoka, K., and Hirano, H. (1985) Difference of lectin binding sites of secretory granules between normal pituitary and adenoma cells, *Acta Neuropathol 66*, 177-183.

[184] Raedler, A., Schmiegel, W. H., Raedler, E., Arndt, R., and Thiele, H. G. (1983) Lectin-defined cell surface glycoconjugates of pancreatic cancer cells and their nonmalignant counterparts, *Exp Cell Biol 51*, 19-28.

[185] Walker, R. A. (1984) The binding of peroxidase-labelled lectins to human breast epithelium. II The reactivity of breast carcinomas to wheat germ agglutinin, *J Pathol 144*, 101-108.

[186] Roth, J. (2011) Lectins for histochemical demonstration of glycans, *Histochem Cell Biol 136*, 117-130.

[187] Kiessling, L. L., and Pohl, N. L. (1996) Strength in numbers: non-natural polyvalent carbohydrate derivatives, *Chem Biol 3*, 71-77.

[188] Taatjes, D. J., Roth, J., Peumans, W., and Goldstein, I. J. (1988) Elderberry bark lectin-gold techniques for the detection of Neu5Ac (alpha 2,6) Gal/GalNAc sequences: applications and limitations, *Histochem J 20*, 478-490.

[189] Geisler, C., and Jarvis, D. L. (2011) Effective glycoanalysis with Maackia amurensis lectins requires a clear understanding of their binding specificities, *Glycobiology 21*, 988-993.

[190] Dotan, N., Altstock, R. T., Schwarz, M., and Dukler, A. (2006) Anti-glycan antibodies as biomarkers for diagnosis and prognosis, *Lupus 15*, 442-450.

[191] Padler-Karavani, V., Yu, H., Cao, H., Chokhawala, H., Karp, F., Varki, N., Chen, X., and Varki, A. (2008) Diversity in specificity, abundance, and composition of anti-Neu5Gc antibodies in normal humans: potential implications for disease, *Glycobiology 18*, 818-830.

[192] Makovitzky, J. (1986) The distribution and localization of the monoclonal antibody-defined antigen 19-9 (CA19-9) in chronic pancreatitis and pancreatic carcinoma. An immuno-histochemical study, *Virchows Arch B Cell Pathol Incl Mol Pathol 51*, 535-544.

[193] Sait, S., and Modak, S. (2017) Anti-GD2 immunotherapy for neuroblastoma, *Expert Rev Anticancer Ther 17*, 889-904.

[194] Sterner, E., Flanagan, N., and Gildersleeve, J. C. (2016) Perspectives on Anti-Glycan Antibodies Gleaned from Development of a Community Resource Database, *ACS Chem Biol 11*, 1773-1783.

[195] Cummings, R. D., and Etzler, M. E. (2009) Antibodies and Lectins in Glycan Analysis, In *Essentials of Glycobiology*, Cold Spring Harbor Laboratory Press, New York, 633-648.

[196] Cummings, R. D., Darvill, A. G., Etzler, M. E., and Hahn, M. G. (2015) Glycan-Recognizing Probes as Tools, In *Essentials of Glycobiology*, Cold Spring Harbor Laboratory Press, New York, 611-625.

[197] Manimala, J. C., Roach, T. A., Li, Z., and Gildersleeve, J. C. (2007) High-throughput carbohydrate microarray profiling of 27 antibodies demonstrates widespread specificity problems, *Glycobiology 17*, 17C-23C.

[198] Powers, T. W., Neely, B. A., Shao, Y., Tang, H., Troyer, D. A., Mehta, A. S., Haab, B. B., and Drake, R. R. (2014) MALDI imaging mass spectrometry profiling of N-glycans in formalin-fixed paraffin embedded clinical tissue blocks and tissue microarrays, *PLoS One 9*, e106255.

[199] Powers, T. W., Holst, S., Wuhrer, M., Mehta, A. S., and Drake, R. R. (2015) Two-Dimensional N-Glycan Distribution Mapping of Hepatocellular Carcinoma Tissues by MALDI-Imaging Mass Spectrometry, *Biomolecules 5*, 2554-2572.

[200] Everest-Dass, A. V., Briggs, M. T., Kaur, G., Oehler, M. K., Hoffmann, P., and Packer, N. H. (2016) N-glycan MALDI Imaging Mass Spectrometry on Formalin-Fixed Paraffin-Embedded Tissue Enables the Delineation of Ovarian Cancer Tissues, *Mol Cell Proteomics 15*, 3003-3016.

[201] Drake, R. R., Powers, T. W., Jones, E. E., Bruner, E., Mehta, A. S., and Angel, P. M. (2017) MALDI Mass Spectrometry Imaging of N-Linked Glycans in Cancer Tissues, *Adv Cancer Res 134*, 85-116.

[202] McDowell, C. T., Klamer, Z., Hall, J., West, C. A., Wisniewski, L., Powers, T. W., Angel, P. M., Mehta, A. S., Lewin, D. N., Haab, B. B., and Drake, R. R. (2020) Imaging Mass Spectrometry and Lectin Analysis of N-Linked Glycans in Carbohydrate Antigen-Defined Pancreatic Cancer Tissues, *Mol Cell Proteomics 20*, 100012.

[203] Briggs, M. T., Condina, M. R., Ho, Y. Y., Everest-Dass, A. V., Mittal, P., Kaur, G., Oehler, M. K., Packer, N. H., and Hoffmann, P. (2019) MALDI Mass Spectrometry Imaging of Early- and Late-Stage Serous Ovarian Cancer Tissue Reveals Stage-Specific N-Glycans, *Proteomics 19*, e1800482.

[204] Ceroni, A., Maass, K., Geyer, H., Geyer, R., Dell, A., and Haslam, S. M. (2008) GlycoWorkbench: a tool for the computer-assisted annotation of mass spectra of glycans, *J Proteome Res 7*, 1650-1659.

[205] Kallweit, U. B., K.O.; Kresbach, G.M.; Widmer, H.M.;. (1996) Matrix Compatible Buffers for Analysis of Proteins with Matrix-assisted Laser Desorption/Ionization Mass Spectrometry, *Rapid Comm. Mass Spec 10*, 845-849.

[206] Heijs, B., Holst, S., Briaire-de Bruijn, I. H., van Pelt, G. W., de Ru, A. H., van Veelen, P. A., Drake, R. R., Mehta, A. S., Mesker, W. E., Tollenaar, R. A., Bovee, J. V., Wuhrer, M., and McDonnell, L. A. (2016) Multimodal Mass Spectrometry Imaging of N-Glycans and Proteins from the Same Tissue Section, *Anal Chem 88*, 7745-7753.

[207] Biskup, K., Braicu, E. I., Sehouli, J., Fotopoulou, C., Tauber, R., Berger, M., and Blanchard, V. (2013) Serum glycome profiling: a biomarker for diagnosis of ovarian cancer, *J Proteome Res 12*, 4056-4063.

[208] Biskup, K., Braicu, E. I., Sehouli, J., Tauber, R., and Blanchard, V. (2017) The ascites N-glycome of epithelial ovarian cancer patients, *J Proteomics 157*, 33-39.

[209] Dedova, T., Braicu, E. I., Sehouli, J., and Blanchard, V. (2019) Sialic Acid Linkage Analysis Refines the Diagnosis of Ovarian Cancer, *Front Oncol 9*, 261.

[210] Kuzmanov, U., Jiang, N., Smith, C. R., Soosaipillai, A., and Diamandis, E. P. (2009) Differential N-glycosylation of kallikrein 6 derived from ovarian cancer cells or the central nervous system, *Mol Cell Proteomics 8*, 791-798.

[211] Tang, H., Hsueh, P., Kletter, D., Bern, M., and Haab, B. (2015) The detection and discovery of glycan motifs in biological samples using lectins and antibodies: new methods and opportunities, *Adv Cancer Res 126*, 167-202.

[212] Ballehaninna, U. K., and Chamberlain, R. S. (2012) The clinical utility of serum CA 19-9 in the diagnosis, prognosis and management of pancreatic adenocarcinoma: An evidence based appraisal, *J Gastrointest Oncol 3*, 105-119.

[213] Haji-Ghassemi, O., Blackler, R. J., Martin Young, N., and Evans, S. V. (2015) Antibody recognition of carbohydrate epitopesdagger, *Glycobiology 25*, 920-952.

[214] Fournier, I., Wisztorski, M., and Salzet, M. (2008) Tissue imaging using MALDI-MS: a new frontier of histopathology proteomics, *Expert Rev Proteomics 5*, 413-424.

[215] Goto-Inoue, N., Hayasaka, T., Zaima, N., and Setou, M. (2011) Imaging mass spectrometry for lipidomics, *Biochim Biophys Acta 1811*, 961-969.

[216] Fujimura, Y., and Miura, D. (2014) MALDI Mass Spectrometry Imaging for Visualizing In Situ Metabolism of Endogenous Metabolites and Dietary Phytochemicals, *Metabolites 4*, 319-346.

[217] Drake, R. R., Jones, E. E., Powers, T. W., and Nyalwidhe, J. O. (2015) Altered glycosylation in prostate cancer, *Adv Cancer Res 126*, 345-382.

[218] Anugraham, M., Jacob, F., Nixdorf, S., Everest-Dass, A. V., Heinzelmann-Schwarz, V., and Packer, N. H. (2014) Specific glycosylation of membrane proteins in epithelial ovarian cancer cell lines: glycan structures reflect gene expression and DNA methylation status, *Mol Cell Proteomics 13*, 2213-2232.

[219] Park, D. D., Phoomak, C., Xu, G., Olney, L. P., Tran, K. A., Park, S. S., Haigh, N. E., Luxardi, G., Lert-Itthiporn, W., Shimoda, M., Li, Q., Matoba, N., Fierro, F., Wongkham, S., Maverakis, E., and Lebrilla, C. B. (2020) Metastasis of cholangiocarcinoma is promoted by extended high-mannose glycans, *Proc Natl Acad Sci U S A 117*, 7633-7644.

[220] Hamester, F., Legler, K., Wichert, B., Kelle, N., Eylmann, K., Rossberg, M., Ding, Y., Kurti, S., Schmalfeldt, B., Milde-Langosch, K., and Oliveira-Ferrer, L. (2019) Prognostic relevance of the Golgi mannosidase MAN1A1 in ovarian cancer: impact of N-glycosylation on tumour cell aggregation, *Br J Cancer 121*, 944-953.

[221] Swindall, A. F., and Bellis, S. L. (2011) Sialylation of the Fas death receptor by ST6Gal-I provides protection against Fas-mediated apoptosis in colon carcinoma cells, *J Biol Chem 286*, 22982-22990.

[222] Zhuo, Y., Chammas, R., and Bellis, S. L. (2008) Sialylation of beta1 integrins blocks cell adhesion to galectin-3 and protects cells against galectin-3-induced apoptosis, *J Biol Chem 283*, 22177-22185.

[223] Hanahan, D., and Weinberg, R. A. (2011) Hallmarks of cancer: the next generation, *Cell 144*, 646-674.

[224] Hirabayashi, J., Hashidate, T., Arata, Y., Nishi, N., Nakamura, T., Hirashima, M., Urashima, T., Oka, T., Futai, M., Muller, W. E., Yagi, F., and Kasai, K. (2002) Oligosaccharide specificity of galectins: a search by frontal affinity chromatography, *Biochim Biophys Acta 1572*, 232-254.

[225] Christie, D. R., Shaikh, F. M., Lucas, J. A., 4th, Lucas, J. A., 3rd, and Bellis, S. L. (2008) ST6Gal-I expression in ovarian cancer cells promotes an invasive phenotype by altering integrin glycosylation and function, *J Ovarian Res 1*, 3.

[226] Lin, S., Kemmner, W., Grigull, S., and Schlag, P. M. (2002) Cell surface alpha 2,6 sialylation affects adhesion of breast carcinoma cells, *Exp Cell Res 276*, 101-110.

[227] Lise, M., Belluco, C., Perera, S. P., Patel, R., Thomas, P., and Ganguly, A. (2000) Clinical correlations of alpha2,6-sialyltransferase expression in colorectal cancer patients, *Hybridoma 19*, 281-286.

[228] Fidler, I. J. (1978) Tumor heterogeneity and the biology of cancer invasion and metastasis, *Cancer Res 38*, 2651-2660.

[229] Hallou, A., Jennings, J., and Kabla, A. J. (2017) Tumour heterogeneity promotes collective invasion and cancer metastatic dissemination, *R Soc Open Sci 4*, 161007.

[230] Klein, O., Kanter, F., Kulbe, H., Jank, P., Denkert, C., Nebrich, G., Schmitt, W. D., Wu, Z., Kunze, C. A., Sehouli, J., Darb-Esfahani, S., Braicu, I., Lellmann, J., Thiele, H., and Taube, E. T. (2019) MALDI-Imaging for Classification of Epithelial Ovarian Cancer Histotypes from a Tissue Microarray Using Machine Learning Methods, *Proteomics Clin Appl 13*, e1700181.

Appendix

1. List of publications and attended conferences

1.1. Publications

Wieczorek M, Taube E, Braicu EI, Sehouli J, Blanchard V*, Klein O*
* *equal contribution*
In situ N-glycosylation signatures of epithelial ovarian cancer tissue.
Manuscript in preparation

Wieczorek M, Braicu EI, Oliveira-Ferrer L, Sehouli J, Blanchard V (2020)
Immunoglobulin G subclass-specific glycosylation changes in primary epithelial ovarian cancer.
Front. Immunol. 11:654.
https://doi.org/10.3389/fimmu.2020.00654

Weiz S, Wieczorek M, Schwedler C, Kaup M, Braicu EI, Sehouli J, Tauber R, Blanchard V (2016)
Acute-phase glycoprotein N-glycome of ovarian cancer patients analyzed by CE-LIF.
Electrophoresis. 37(11):1461-1467.
https://doi.org/10.1002/elps.201500518

1.2. Conference poster presentations

Wieczorek M, Klein O, Taube E, Braicu EI, Sehouli J, Blanchard V
Unraveling the N-glycosylation profile of epithelial ovarian cancer tissue.
Conference: "11th International Charité Mayo Conference", Berlin, Germany, 2021.
» Best Poster Award «

Wieczorek M, Braicu EI, Oliveira-Ferrer L, Sehouli J, Blanchard V
Immunoglobulin G subclass-specific glycosylation changes in primary epithelial ovarian cancer. Conference: "2020 Society for Glycobiology Virtual Annual Meeting", 2020.

Wieczorek M, Tauber R, Blanchard V
Immunoglobulin G subclass-specific glycosylation changes in primary epithelial ovarian cancer. Conference: "30th Joint Glycobiology Meeting", Lille, France, 2019.

Hamouda H, Ullah M, Wieczorek M, Berger M, Sittinger M, Tauber R, Ringe J, Blanchard V
N-Glycosylation Profile of Undifferentiated and Differentiated Human Bone Marrow Mesenchymal Stem Cells.
Conference: "RESTORE 1st Advanced Therapies Science Meeting", Berlin, Germany, 2019.

Wieczorek M, Klein O, Taube E, Braicu EI, Tauber R, Blanchard V
MALDI-MS Imaging of N-glycans in FFPE ovarian cancer tissue.
Conference: "Annual Congress Biotechnology 2020+", Berlin, Germany, 2018.

Wieczorek M, Tauber R, Blanchard V
Unraveling the IgG glycome of epithelial ovarian cancer patients.
Conference: "SPP Meetup Berlin 2017", Berlin, Germany, 2017.

Wieczorek M, Tauber R, Blanchard V
Unraveling the IgG glycome of epithelial ovarian cancer patients.
Conference: "New and Emerging Technologies", Potsdam, Germany, 2017.
» Best Poster Award (Second Place) «

2. Curriculum Vitae

For reasons of data protection, the curriculum vitae is not included in the online version.

Acknowledgements

In this place, I would like to express my gratitude and appreciation to all people that accompanied me over the last years and helped me accomplish this big step in my professional life.

First and foremost, I want to thank Prof. Dr. Véronique Blanchard for giving me the opportunity to perform my research in the "Glyco Group" under her supervision. Dear Véro, I am grateful for your guidance, support and all scientific and non-scientific knowledge you shared. Although my doctoral projects are finalized at this point, I am looking forward to continue working with you on future projects. In this place, I also would like to thank Prof. Dr. Kevin Pagel for taking his time to act as the second supervisor of this work and Prof. Dr. Rudolf Tauber, a former Head of the Institute of Laboratory Medicine, Clinical Chemistry and Pathobiochemistry, for being a great inspiration and discussion partner.

To Dr. Oliver Klein and his research team that includes Dipl. Ing Grit Nebrich, Dr. Zhyiang Wu, Sylwia Handzik and a former colleague Angelika Krajewski, I owe a big debt of gratitude for their assistance and support in terms of MALDI-MSI experiments. Dear Oliver, thank you for your patient guidance and assistance with data analysis. You are a great scientist, colleague and discussion partner. I hope that we can continue working together in the future. With regard to mass spectrometry imaging, I also would like to acknowledge and sincerely thank the research group of Prof. Dr. Manfred Wuhrer, especially Dr. Stephanie Holst-Bernal, who in 2017 hosted me at the Center for Proteomics and Metabolomics of the Leiden University Medical Center and introduced me to this novel technique. Thank you for sharing your expertise and protocols. It was a great honor to learn from you!

Likewise, I would like to thank all other cooperators and co-authors for their scientific contribution and assistance. In particular, I want to acknowledge Prof. Dr. Elena Ioana Braicu, Prof. Dr. Jalid Sehouli, Dr. Antje Ludwig and Dr. Eliane Taube. It was a great honor and pleasure to work with such great scientists!

I also want to take this opportunity to thank Prof. Stephan Hinderlich, Dr. Grit Sandig and Dr. Julia Rosenlöcher, who warmly welcomed me into their scientific group at Beuth Hochschule Berlin in 2015. You were the first people I got to know in Berlin, and your support made this stressful time easier and undoubtedly nicer. It is you who fueled my interest in protein glycosylation, what eventually led to pursuing a doctorate in this subject. Dear Grit and Julia, I am grateful that after all these years we still manage to stay in touch!

Surely, those last years would not be the same without my friends and colleagues that crossed my path at Charité Virchow-Klinikum. A special thanks goes to my 0.0405 office colleagues that are/were Dr. Karina Biskup, Dr. Christian Schwedler, Dr. Tereza Dědová and Dominique Braumann: I have been lucky to be surrounded by all of you through the last years. I enjoyed our discussions, brain-storms, coffee breaks and, back in the day, Friday's breakfasts – by the way, we should bring this last one back! Karina, you are a great colleague and have become a great friend. Without you, our "Polish mafia" would be nonexistent. At the same time, I want to thank all other current and former members of the "Glyco Group": It was/is a pleasure to work with you all!

My "Mädels", Dr. Nicole Niesler and Dr. Alexandra Trautner, I want to thank for their friendship and all beautiful moments we spent together. Nicole and Alex, thank you for being my personal rays of sunshine, making the rainiest days great again!

These acknowledgements would not be complete without thanking Luca, my soulmate and beloved husband. Dear Luci, I am forever grateful for your love, support and delicious food you always cook for me. I am the luckiest woman on Earth to have you on my side!

W końcu, największe podziękowania należą się moim Rodzicom i Siostrze. Dziękuję Wam za Waszą bezkresną miłość i wsparcie. Wam zawdzięczam wszystko ♥